UNIVERSITY OF OKLAHOMA

GRADUATE COLLEGE

HIGH-PERFORMANCE ANTENNA ARRAYS FOR MULTIFUNCTION PHASED ARRAY RADAR (MPAR) APPLICATION

A DISSERTATION

SUBMITTED TO THE GRADUATE FACULTY

in partial fulfillment of the requirements for the

Degree of

DOCTOR OF PHILOSOPHY

By

HADI SAEIDI MANESH

Norman, Oklahoma

2019

HIGH-PERFORMANCE ANTENNA ARRAYS FOR
MULTIFUNCTION PHASED ARRAY RADAR (MPAR) APPLICATION

A DISSERTATION APPROVED FOR THE
SCHOOL OF ELECTRICAL AND COMPUTER ENGINEERING

BY

Dr. Guifu Zhang, Chair

Dr. Yang Hong

Dr. Richard Doviak

Dr. Hjalti Sigmarsson

Dr. Yan Zhang

© Copyright by HADI SAEIDI MANESH 2019
All Rights Reserved.

To my parents, and my beloved wife, Elaheh.

Acknowledgments

First, I would like to express my sincere gratitude to my research advisor Dr. Guifu Zhang for his unceasing support, motivation and immense knowledge. Dr. Zhang was always available whenever I had questions or ran into problems for my research. I could not have imagined a better advisor and mentor for my PhD study.

I would like to acknowledge my committee members Dr. Richard Doviak, Dr. Yang Hong, Dr. Hjalti Sigmarsson, and Dr. Yan Zhang for their interest and valuable expertise, time, and effort in advising my dissertation work. I am grateful for their insightful comments and input towards the completion of this work.

I am grateful to the generous financial support for my research by National Oceanic and Atmospheric Administration (NOAA). The staff members at the Advanced Radar Research Center (ARRC) and School of Electrical and Computer Engineering (ECE) deserve my sincere thanks as well. I would also like to thank all my friends. They have been a constant source of support and strength. My special thanks to my good friend, Dr. Shahrokh Saeedi for his help and support.

I would like to thank my family for their unfailing support, encouragement, and sacrifice. None of this work would have been possible without them. My gratitude to them is more than that can be expressed in words.

Finally, I would like to thank my beloved wife, Elaheh Jafarigol for her

endless love, continuous encouragement and support throughout this venture. This accomplishment would not have been possible without her.

Table of Contents

List of Tables

List of Figures

Abstract

There are interest and practical value in utilizing polarization diversity for a radar to obtain more target information or for a communication system to carry more signal information without occupying more frequency band. This is because frequency bands are getting crowded in microwave frequencies due to the recent advancements in cellular communications. For example, the Spectrum Efficient National Surveillance Radar Program (SENSR) is started to study the feasibility of replacing the four radar networks that service the U.S with a single network of Multifunction Phased Array Radar (MPAR). Candidates being considered for future MPAR include Cylindrical Polarimetric Phased Array Radar (CPPAR), and Planar Polarimetric Phased Array Radar (PPPAR). To have the desired accurate weather measurements with a PPPAR or CPPAR, a high-performance phased array antenna with dual-polarization capability is required. The array antenna is required to possess matched main beams, high input isolation, and low cross-polarization level at broadside and scan angles up to 45°. The beam mismatch should be within 5% of the beamwidth, the input isolation needs to be better than 40 dB, and to have Z_{DR} bias of less than 0.2 dB, the cross-polarization level along beam axis needs to be lower than -20 dB and -40 dB for alternate and simultaneous transmission, respectively. These are very stringent requirements for antenna design and development.

The primary objective of this dissertation is to propose high-performance

dual-polarized antenna arrays with high input isolation and low cross-polarization level for multifunction phased radar application. To do so, four different types of dual-polarized microstrip patch antenna arrays are presented. In the proposed patch antennas, different feeding techniques such as, aperture coupling method, balanced feed method and the combination of these methods which is called hybrid feeding technique are used. The proposed antenna arrays in this dissertation are configured according to image configuration for improving the cross-polarization level. The issues and challenges of implementing image arrangement is discussed, and precise procedure for design and predicting the final array radiation characteristics is proposed.

The CPPAR demonstrator antenna is redesigned to achieve matched horizontal and vertical polarization beam pointing angels. A method of beam matching between two linearly polarized radiation patterns of a dual-polarized frequency scanning antenna is proposed, implemented, and tested. A meticulous phase match process between the outputs of both individual cells and the whole corresponding horizontal and vertical feed lines is carried out. To verify the simulation results and to take the coupling effect into account, the radiation patterns of an isolated column, as well as those of three columns, are measured. In agreement with the design and simulation results, horizontal and vertical polarization beams with a pointing angle mismatch of less than $\pm 0.2^{\circ}$ within the resonant frequency bandwidth of 2.75–2.95 GHz are achieved.

Chapter 1

Introduction

1.1 Microstrip Patch Antennas

By introduction of the ground plane and advances in the printed circuit board technology, the two-wire transmission lines were reduced to planar configurations. Planar configurations provided opportunities for realizing new microwave techniques. The advantages of using planar configurations such as microstrip structures include low-cost, low-size, low-weight, and more importantly good electrical and electromagnetic characteristics. A microstrip transmission line is basically evolved from the two-wire transmission line. Fig. 1.1 shows the parallel wire transmission line concept. If an infinite width ground plane is placed between the two wires, then according to the image theory, the image of the upper conductor will exist at the location of the lower conductor. Consequently, the lower conductor line can be removed. Also, the upper conductor can be replaced with a strip placed on the ground plane while a dielectric layer is sandwiched between the ground plane and the upped conductor, forming a microstrip transmission line [1].

Microstrip patch antennas can be considered as an extension of microstrip transmission lines and were first proposed in [1] by Grieg and Englemann in

1952. Fig. 1.2 shows the geometry of a microstrip patch antenna fed by a microstrip line. Other feeding techniques are also possible, and some of them will be discussed in this dissertation. Similar to microstrip transmission lines, microstrip patch antennas have several desirable characteristics. For instance, the microstrip antennas are low profile, comformable to planar and non-planar surfaces, simple and inexpensive to fabricate using modern printed-circuit technology. Also, using flexible substrates, conformal antennas whose shapes are conformed by non-electromagnetic requirements are also feasible.

Realizing dual-polarization capability is also possible using microstrip patch antennas. In fact, the most common type of dual-polarized element, for antenna array applications, is microstrip patch antenna. Compared to a high-performance dipole antenna, it possesses a low profile geometry with less fabrication complexity, especially in the array configurations. In this chapter, an overview of various designs of dual-polarized microstrip patch antennas is presented.

1.2 Dual-Polarized Microstrip Patch Antennas

A dual-polarized patch antenna can be excited using two coaxial feeds placed at two orthogonal points. The coaxial feed ports are located at the Null location of horizontal and vertical polarizations. Therefore, the input impedance of polarization won't be affected by the other polarization feed line. Microstrip patch antennas excited using this method are known as probe-fed (pin-fed) patch antennas. In Ref. [3] a probe-fed patch antenna is designed, and an isolation level of better than 30 dB is reported.

As shown in Fig. 1.3 in the probe-fed patch antenna the inner conductor of coaxial feed is connected to radiating patch antenna. However, as shown in Fig. 1.4, the patch antenna can be excited using capacitive probes, in which there

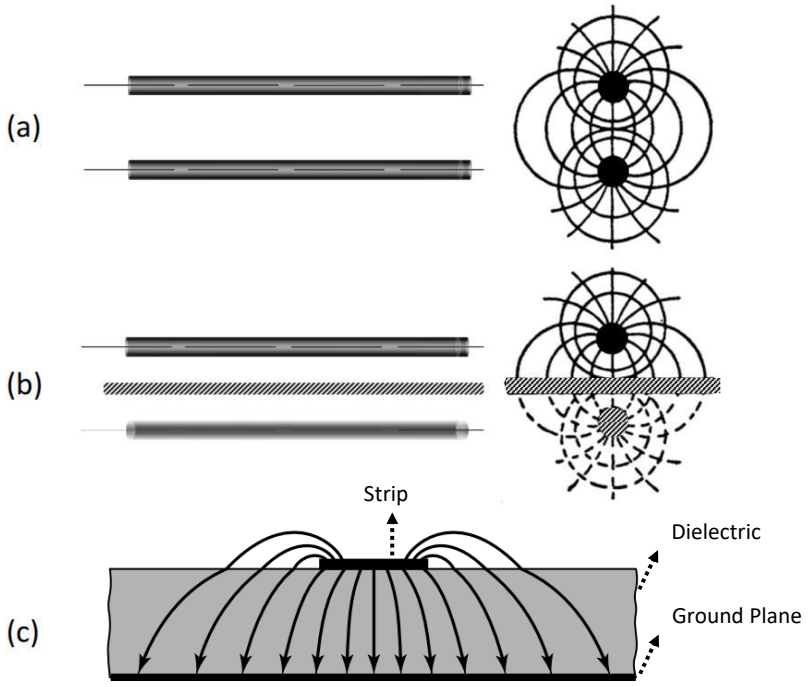

Fig. 1.1: Evolution of a line above ground plane; (a) Two-wire transmission line, (b) One conductor above ground plane,[1] (c) Microstrip transmission line [2].

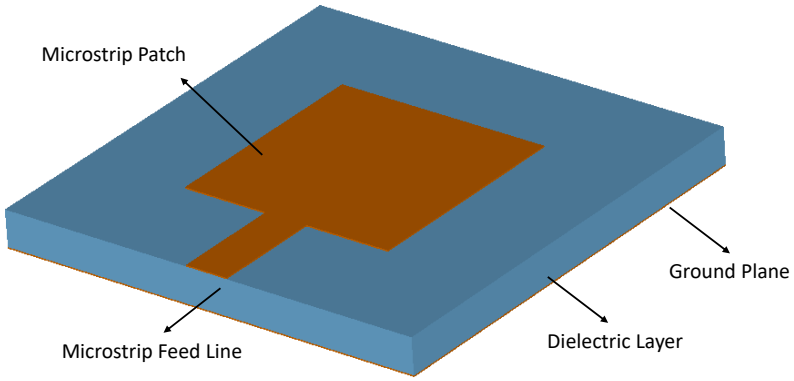

Fig. 1.2: Microstrip patch antenna configuration.

is a gap between excitation capacitive probes and radiating patch. In Ref. [4], a microstrip patch antenna is excited using two L-shaped capacitive probes. In the presented design in Ref. [4], input isolation of 20 dB is reported. Different

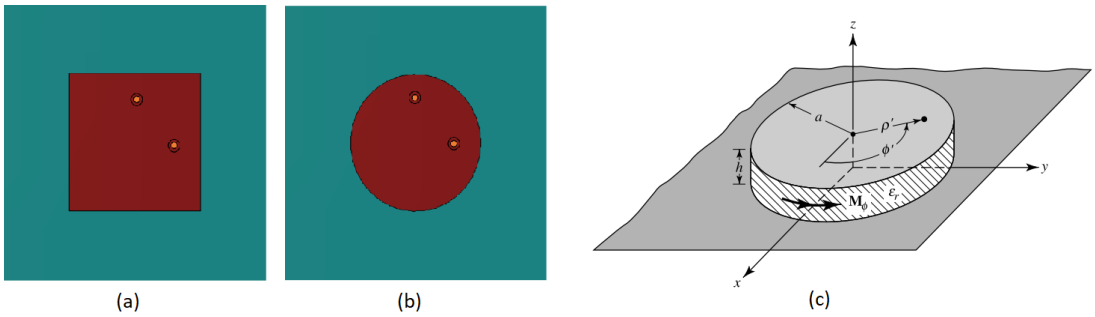

Fig. 1.3: Probe-fed microstrip patch antenna; (a) Square patch, (b) Circular patch; (d) equivalent magnetic current density for circular microstrip patch antenna.[2]

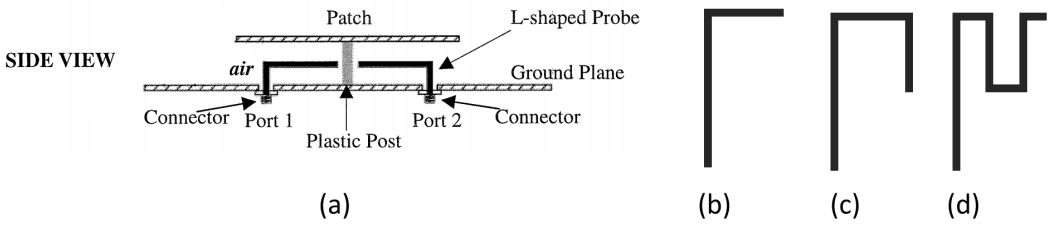

Fig. 1.4: A dual-polarized probe-fed microstrip antenna; (a) 3-d configuration, (b) L-shaped probes, (c) Hook shaped probe, (d) Meandering probe [4], [6].

configurations such as hook-shaped and T-shaped meandering probes have been proposed to improve the horizontal to vertical ports isolation. Also, it is shown that surrounding the antenna with metallic walls, will result in a better isolation. An isolation level of better than 30 dB by using metallic walls is reported in [5].

The aperture-coupled patch antenna was first introduced by Pozar [7]. This type of patch antenna has been studied and developed into different dual-polarized designs. Fig. 1.5 shows several configurations which have been implemented and discussed in the literature. A dual-polarized aperture coupled patch antenna can be realized through a centered crossed-slots or two separated orthogonal slots. In the crossed-slot design in order to avoid overlapping between two orthogonal feed lines, a double layer substrate or an air bridge is required unless the non-overlapping feed lines method is utilized.

Dual-polarized aperture-coupled patch antennas with two separate slots and

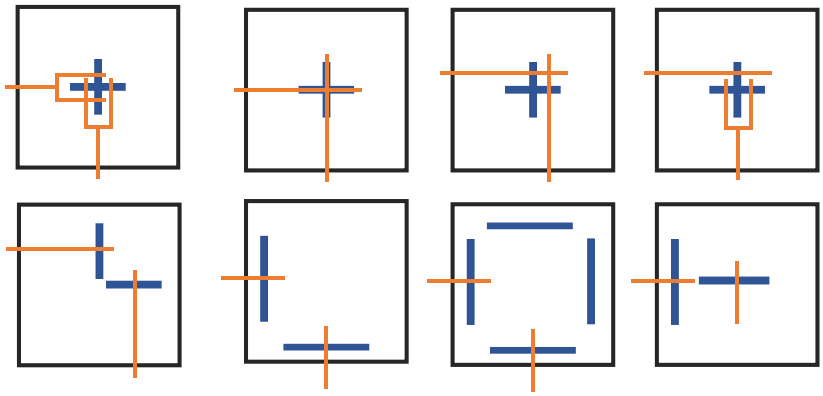

Fig. 1.5: Some configurations of dual-polarized slot-coupled patch antennas [8].

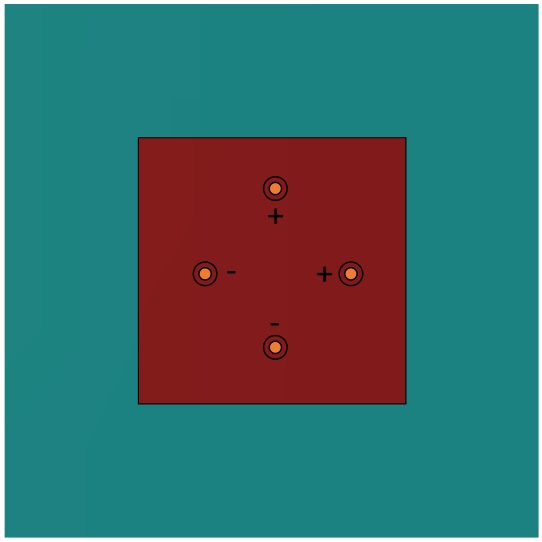

Fig. 1.6: Microstrip patch antenna excited using balanced feed method.

two non-overlapping feed lines etched on the same side of a substrate can be used when high-isolation is required. The back lobe level in the aperture-coupled patch antennas can be enhanced by using a ground plane below the feed lines.

The impedance bandwidth of microstrip patch antenna is typically %3. Different bandwidth enhancement methods have been proposed, in the open literature. Using thick dielectric material and implementing stacked patch configuration are among well-known bandwidth enhancement methods. In the multilayer configuration, a parasitic square patch with smaller or larger

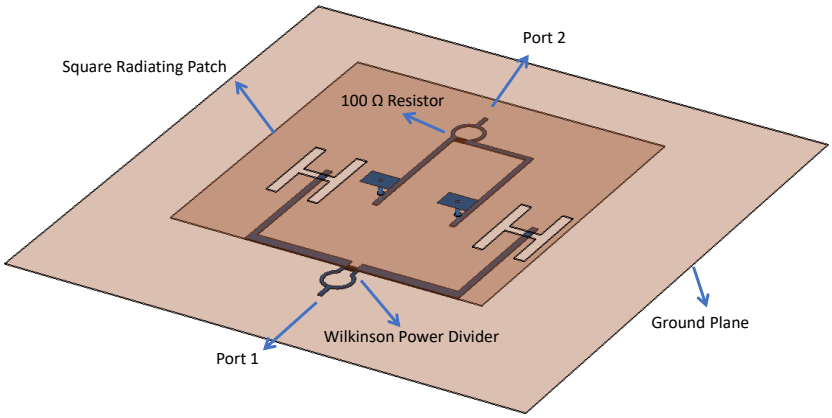

Fig. 1.7: Geometry of a broad-band dual-polarized square patch antenna fed by two in-phase aperture-coupled feeds (port 1) and two out-of-phase gap-coupled probe feeds (port 2) [10].

dimensions is placed on top of the radiating square patch. While using the thick dielectric material for increasing the bandwidth, it should be noted that this may result in a distorted radiation pattern. This is because increasing the substrate thickness will result in excitation of stronger higher order modes. To cancel higher order modes, microstrip patch antennas can be excited through two probes, placed on opposite locations and excited with 180° phase difference. Fig. 1.6 shows the balanced feed or differential feed method proposed by Chiba in 1982 [9]. Balanced feed method will significantly reduce the cross-polarization level of the antenna and in dual-polarization configuration, and a very high input isolation between horizontal and vertical polarization.

In the hybrid feed technique, different excitation methods are combined. With an appropriate design, the hybrid feed method could result in a compact design, low cross-polarization radiation pattern and high input isolation. Compared to the dual-polarized differential feed design, the hybrid feed design requires less space for feed lines, which results in a more compact design [11]. Also, the hybrid feed design provides a more symmetric feature which will

improve the isolation between the horizontal and vertical ports. The geometry of a dual-polarized hybrid-fed microstrip patch antenna is shown in Fig. 1.7. In this design, one port is excited through two in-phase aperture-coupled feeds, and the other port is excited using two out-of-phase gap-coupled probe feeds [10]. In this design the cross-polarization level of lower than -20 dB and input isolation of -40 dB were realized. In [12], a dual-polarized patch antenna is fed by an aperture coupled feed and two capacitively coupled feeds of a 180° phase shift. In this design, the input isolation of better than 32 dB and cross-polarization level of -14.4 dB were reported.

1.3 Phased Array Radar

One way to increase the antenna gain and achieve more directive radiation pattern is to increase the dimension of the single element. One way of increasing the antenna gain, without increasing the single elements size is to arrange single elements beside each other in a geometrical and electrical configuration. The new antenna which is made of multiple single elements is called an array antenna or antenna array.

IEEE standard definition of the term for antenna array (array) is as follows: "array antenna; antenna array. An antenna comprised of a number of identical radiating elements in a regular arrangement and excited to obtain a prescribed radiation pattern.

NOTES: (1) The regular arrangements possible include ones in which the elements can be made congruent by simple translation or rotation. (2) This term is sometimes applied to cases where the elements are not identical or arranged in a regular fashion. For those cases qualifiers shall be added to distinguish from the usage implied in this definition. For example, if the elements are randomly

located one may use the term random array antenna." Phased array antennas are made of several fixed elements, in which each element is being fed by variable amplitudes and phases to form the beam and scan the beam to specified angles.

A conformal array antenna is an antenna which its shape has been determined by another object. This could be a car, a building, airplane or any other object. The purpose of designing conformal antenna arrays could be the integration of the antenna with other objects to be less disrupting or less visible. In some other applications, the conformal geometry will decrease the backscatter radiation when the antenna is illuminated by another radar antenna.

The IEEE Standard Definition of Terms for Antennas (IEEE Std 145-1993) gives the following definition:

Antenna [conformal array]. An antenna [an array] that conforms to a surface whose shape is determined by considerations other than electromagnetic; for example, aerodynamic or hydrodynamic.

Conformal array. See: conformal antenna.

By this definition planar antenna is also a type of conformal antenna when the shape of the array is determined with reasons other than electromagnetic considerations. However in practice, usually the spherical, cylindrical and some other shapes are considered as conformal array geometries.

Cylindrical array antennas without shape being dictated by non-electromagnet reasons are usually considered conformal arrays. In cylindrical polarimetric phased array radar antenna, the shape is determined by electromagnetic requirements such as low cross-polarization, matched horizontal and vertical and scan invariant radiation patterns. A cylindrical array antenna has a potential of 360° coverage either with a narrow beam that can steer over 360° or an omnidirectional beam, multiple beams.

As mentioned before, in a phased array the fixed element elements can be fed by variable amplitudes and phases to form and steer the antenna array radiation pattern. Depending on the array antenna configuration the amplitude and phase of excitation of each element can be calculated. For linear and planar antennas, the array radiation pattern can be estimated based on the element pattern and the array factor. The array antenna IEEE standard definition for array factor is as follows:

"**Array Factor.** The radiation pattern of an array antenna when each array element is considered to radiate isotropically. NOTE: When the radiation patterns of individual array elements are identical, and the array elements are congruent under translation, then the product of the array factor and the element radiation pattern gives the radiation pattern of the entire array."

Circular and cylindrical arrays possess an advantage of the symmetrical radiation pattern in azimuth, which makes the circular and cylindrical array configurations very interesting for radar applications. However, calculating the antenna radiation pattern is more complicated compared to linear and planar array antennas since the element radiation pattern also depends on the element location. Therefor, in circular and cylindrical array antenna coherent addition method is being used for calculating the array radiation pattern.

Multifaceted array antenna geometry is the combination of planar and cylindrical configurations. The analysis of the multifaceted array antenna is more complicated than cylindrical array antennas. The primary advantage of multifaceted arrays compared to the cylindrical arrays is lower fabrication cost.

1.4 Multifunction Phased Array Radar

Currently, it takes about 5 min for a WSR-88D radar to complete a volumetric scan. The 5 min data update time is too slow for severe weather events such as tornados and downburst which sometimes last only a few minutes. It is desirable to have radar date with a higher temporal resolution (¡1min), so detailed evolutions of severe storm phenomena can be revealed and tracked. This level of detail is difficult to achieve operationally with a mechanically scanning dish antenna radar. The need for fast data updates leads to using advanced radar technology such as phased array radar which has an agile beam that steers electronically and quickly. [13]. The spatial diversity for the phased array radars can be achieved by using the multiple-input-multiple-output (MIMO) radars [14]–[17]. Digital Arrays, including radars and large-scale MIMO arrays have a better performance compared to the traditional phased array technology; however, their dynamic range suffers in the presence of strong interferers [18]. Currently, there are four radar networks: (1) National Weather Surveillance Radar (WSR-88D or NEXRAD); (2) Terminal Doppler Weather Radar (TDWR); (3) Airport Surveillance Radar (ASR); and (4) Air Route Surveillance Radar (ARSR) which are serving the United States on their own missions separately. There are issues such as overlap of coverage and functionality and difficulty in data sharing among these radar networks. To avoid these issues and advance air and weather surveillance capability, a single Multi-Function Phased Array Radar (MPAR) network was proposed and developed by a joint effort of the National Oceanic and Atmospheric Administration's (NOAA's) and the Federal Aviation Administration (FAA) [19]-[13], [20]. Also, since WSR-88D has been updated with the dual-polarization capability, the future MPAR should also have this capability [21], [22]. Using a single radar for long-range,

short-range, and weather applications can also result in vacating the 1300-1350 MHz spectrum for commercial use.

Polarimetric Phased Array Radars (PPAR) have been developed for military and space applications [23]. Planar Polarimetric Phased-Array Radar (PPPAR) and Cylindrical Polarimetric Phased-Array Radar (CPPAR) are being considered as the next generation of radars for MPAR [24], [25]. PPPAR, however, has fundamental shortcomings in beam characteristics and polarization coupling depend on beam direction, causing geometrically induced cross-polarization coupling and limitations in making high-quality weather measurements. [13], [26] It is crucial to design and develop a high-performance array antenna to achieve the goals of MPAR [27], [28].

MPAR is required to operate according to the Manual of Regulations and Procedures for Radio Frequency Management (47 Code of Federal Regulations (CFR) Part 300) and FAA Order 6050.19. Regarding operational bandwidth, when replacing ASR and TDWR, MPAR is required to operate in the 2.7 - 2.9 GHz band, one which is allocated for aeronautical radio navigation. However, when replacing the WSR-88D and the ARSR radars (i.e., so-called Long Range Radars; LRRs), the MPAR must operate in 2.7-3.0 GHz. For the National Weather Service (NWS) application, elevation scan angles less than 20° MPAR must provide differential reflectivity (Z_{DR}) estimates with a bias no more than 0.1 dB for the $Z_{DR} \leq 1$ dB [29]. The primary objective of this dissertation is designing antenna elements and structures that will support MPAR to meet the array radiation pattern requirements. For the MPAR applications, the cross-polarization level and horizontal and vertical ports isolation should be close to current WSR-88D measured characteristics. Based on measured and theoretically calculated copolarization and cross-polarization radiation patterns

for the WSR-88D, the cross-polarization field has a null along the co-polarization beam [30]. However, if cross-polarization radiation has a lobe coaxial with the co-polarization beam, the requirement that Z_{DR} bias should be less than 0.1 dB, requires the cross-polarization peak to be more than 45 dB below the copolarization peak [31]. This level of cross-polarization can be relaxed if phase coding is used [32]. If a cross-polarization lobe is coaxial with the copolarization beam, the largest relaxation about the peak level of a coaxial cross-polarization lobe is attained if the two polarizations are either in or out of phase with each other. In this case, the peak level of the cross-polarization radiation is relaxed to about 26 dB below the copolarization peak [33].

1.5 Outline of the Dissertation

This dissertation is devoted to design, fabrication, and characterization of phased array antennas with a low cross-polarization level along the copolarization beam and high input isolation between horizontal and vertical polarizations. The primary goal is to investigate the capability of microstrip patch antennas for MPAR applications. Therefore, all the designed and presented antennas in this dissertation are based on microstrip patch antennas.

In chapter 2, three different low cross-polarization, high-isolation dual linear polarized microstrip patch antennas are designed for MPAR application. In the first design, a dual-polarized microstrip patch antenna is excited through the aperture coupling method. Although dual-polarized aperture-coupled patch antennas with two non-overlapping feed lines laid on a single side of a laminate have been implemented for several applications, an array of very high isolation and low cross-polarization that meets MPAR requirements has not been reported. In the second design, the hybrid feed technique is implemented. In the

presented example of hybrid fed patch antenna, the horizontal polarization is excited through the differential probe feed method, and the vertical polarization is excited through an H-shaped aperture in the middle of the ground plane. In the third presented patch antenna, the horizontal polarization is excited through two 180° out of phase apertures, and vertical polarization is excited by an aperture in the middle of the ground plane.

In chapter 3, the challenges and limitations of using cross-polarization suppression methods for dual-linear polarization antenna arrays are presented. A simple probe-fed patch antenna and a high-performance, high isolation, low cross-polarization dual-polarized patch antenna are used for this study. The image feed method is used for improving the cross-polarization level and increasing the geometrical symmetry of the large array antenna. It is shown that decomposing the antenna radiation pattern to its even and odd components for calculating 2×2-element subarray radiation pattern has fundamental limitations and none of the four different 2×2-element subarray configurations will entirely suppress the sidelobe issue of configured arrays. The accuracy of using embedded element pattern for calculating the radiation pattern of the large array with identical subarrays is studied and an accurate procedure for predicting array antenna radiation pattern is proposed. The appearance of undesired sidelobes has been studied, and optimal design for the large array of 2×2-element subarrays with image configuration is presented to reduce the sidelobes.

In chapter 4, the performance of the designed single elements in chapter 2 are characterized while these designs are implemented in an array. To improve the cross-polarization level, the 2×2-element subarrays of the proposed single elements are designed, fabricated and tested. To characterize the radiation pattern of the

designed subarrays, the planar arrays of the presented subarrays, are fabricated, and the radiation pattern of the antenna arrays at broadside and various scan angles are provided and discussed.

In chapter 5, a method of beam matching between two linear polarized radiation patterns of a dual-polarized frequency scanning antenna for CPPAR is proposed, implemented, and tested. A meticulous phase match process between the outputs of both individual cells and the whole corresponding horizontal and vertical feed lines is carried out. To verify the simulation results and to take the coupling effect into account, the radiation patterns of an isolated column, as well as those of three columns, are measured. In agreement with the design and simulation results, horizontal and vertical polarization beams with a pointing angle mismatch of less than $\pm 0.2^{\circ}$ within the resonant frequency bandwidth of 2.75-2.95 GHz are achieved.

Chapter 6 concludes the dissertation by providing a summary of the work.

Chapter 2

High Performance Dual-Polarized Microstrip Patch Antennas for MPAR Application

In this section, three different excitation methods for realizing a low cross-polarization, high-isolation dual linear-polarized microstrip patch antenna for MPAR application are presented. In the first design, a dual-polarized microstrip patch antenna is excited through aperture coupling method [12], [34]. In the second design, hybrid feed technique is implemented and the vertical and horizontal polarizations are excited by a balanced-probe feed and a slot-coupled feed, respectively. In the third presented patch antenna, the horizontal and vertical polarizations are excited through two 180° out-of-phase apertures and an aperture in the middle of the ground plane, respectively.

2.1 Asymmetric Non-Overlapping Aperture Coupled Patch Antenna

The geometry of the designed dual linear-polarization stacked patch antenna is shown in Fig. 2.1. The antenna consists of two stack patches, two H-shaped slots on the ground plane and two microstrip feed lines. Two transmission lines are laid on the bottom side of the first substrate layer which is a Taconic TLX-8 with

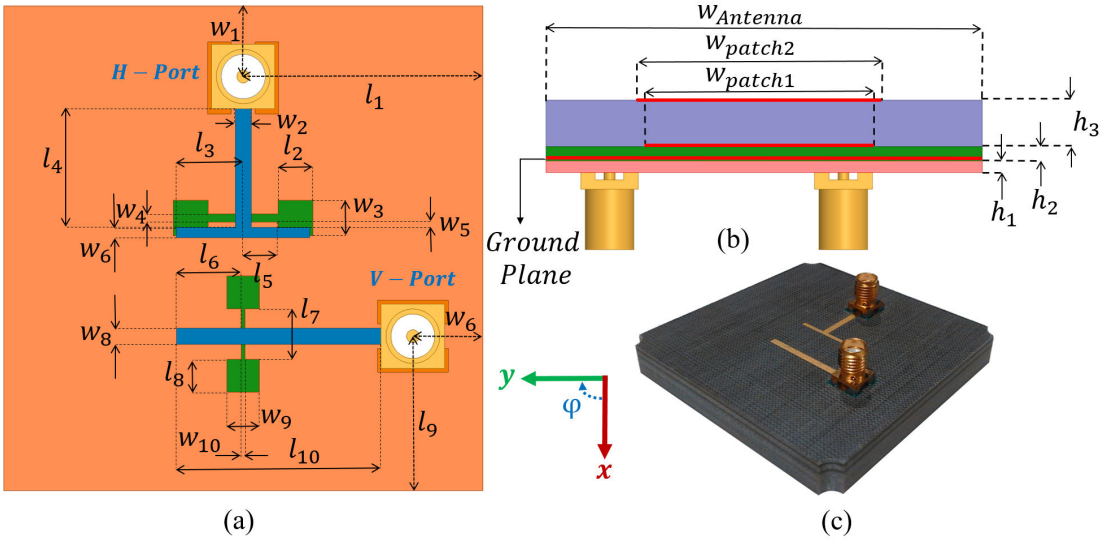

Fig. 2.1: Geometry of the designed single element. (a) bottom view, (b) side view, (c) fabricated single element.

the height of h_1. The ground plane is laid on the other side of the first substrate. A radiating square patch (width $w_{patch1} = 24.4mm$) is etched on the substrate Taconic TLX-8 with the height of h_2. To increase the bandwidth of the single element a square parasitic patch (width $w_{patch2} = 27.2mm$) is placed above the radiating patch. The sizes of the radiating and parasitic patches are optimized to provide required bandwidth and be as small as possible to reduce the size of the single element. The dielectric constant of Taconic TLX-8 is 2.55. Using a high dielectric constant substrate will reduce the size of a single element but it will limit the impedance bandwidth of the antenna [35].

For MPAR application, it is required for an array antenna to have an impedance bandwidth ($S_{11} < -10dB$) from 2.7 GHz to 3.0 GHz. Increasing the spacing between array elements will decrease the coupling between two adjacent elements in the array, however increasing the separation between elements more than $\lambda/2$ creates grating lobe and moves the scan blindness angle toward antenna broadside direction [36]. The parameter study and optimization of the

Table 2.1: Dimensions of the designed non-overlapping aperture-coupled patch antenna.

Parameter	Size	Parameter	Size
l_1	30.55 mm	w_1	13.55 mm
l_2	3.5 mm	w_2	1.6 mm
l_3	6.62 mm	w_3	0.8 mm
l_4	11.77 mm	w_4	3.5 mm
l_5	3.5 mm	w_5	0.55 mm
l_6	6.46 mm	w_6	1.025 mm
l_7	5 mm	w_7	6.35 mm
l_8	3.25 mm	w_8	1.6 mm
l_9	21.83 mm	w_9	3.25 mm
l_{10}	20.47 mm	w_{10}	0.4 mm
h_1	0.787 mm	$W_{Antenna}$	61.1 mm
h_2	1.575 mm	W_{patch1}	24.4 mm
h_3	5 mm	W_{patch2}	27.2 mm

designed single element has been carried out using ANSYS HFSS and CST Microwave Studio. The element impedance bandwidth is optimized while considering the element as a unit cell in an infinite array so the single element would have an acceptable performance in an array when all other elements are excited. The dimensions of the designed single element shown in Fig. 2.1 are listed in Table. 2.1.

The simulated and measured reflection coefficient of horizontal (S_{HH}) and vertical (S_{VV}) polarizations and isolation between horizontal and vertical ports (S_{HV}) of the designed single element are shown in Fig. 2.2. The measurements are performed in a small anechoic chamber specially designed for the S-parameter

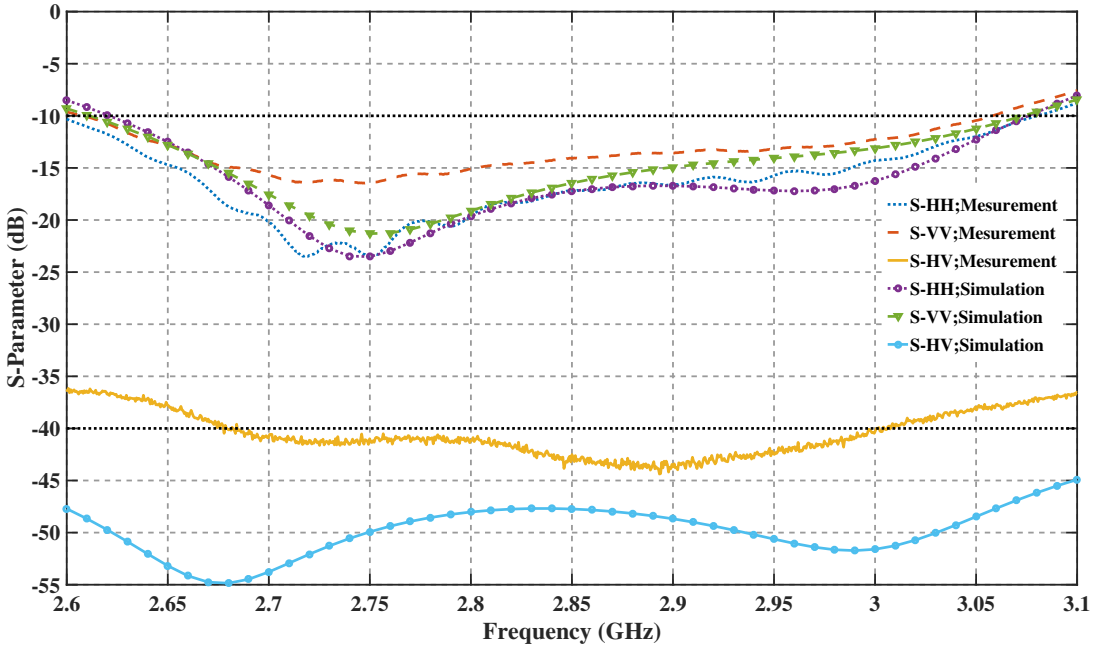

Fig. 2.2: Reflection coefficient and isolation of the designed single element.

measurements. The S_{HH} and S_{VV} are below -10 dB from 2.7 GHz to 3.0 GHz and as it is shown in Fig. 2.2 there is a good agreement between simulated and measured results. The isolation between H and V ports is better than 47 dB in simulation and 41 dB in measurement in the entire frequency band (2.7 GHz - 3.0 GHz), which is an acceptable agreement for a high-isolation antenna.

Achieving the low cross-polarization level in dual-polarized antennas is one of the most important issues. To enhance the isolation between H and V ports, the two slots are placed in a "T" arrangement. Fig. 2.3 shows the vector current distribution around H-shaped slots when H and V ports are separately excited. Fig. 2.3 (a) shows the current distribution on the ground plane when the horizontal port is excited and vertical port is terminated. As shown in Fig. 2.3 (a) when the horizontal port is excited the current level around the vertical polarization slot is around 30 dB lower than the current around the horizontal polarization slot. Also current around the horizontal polarization slot form a

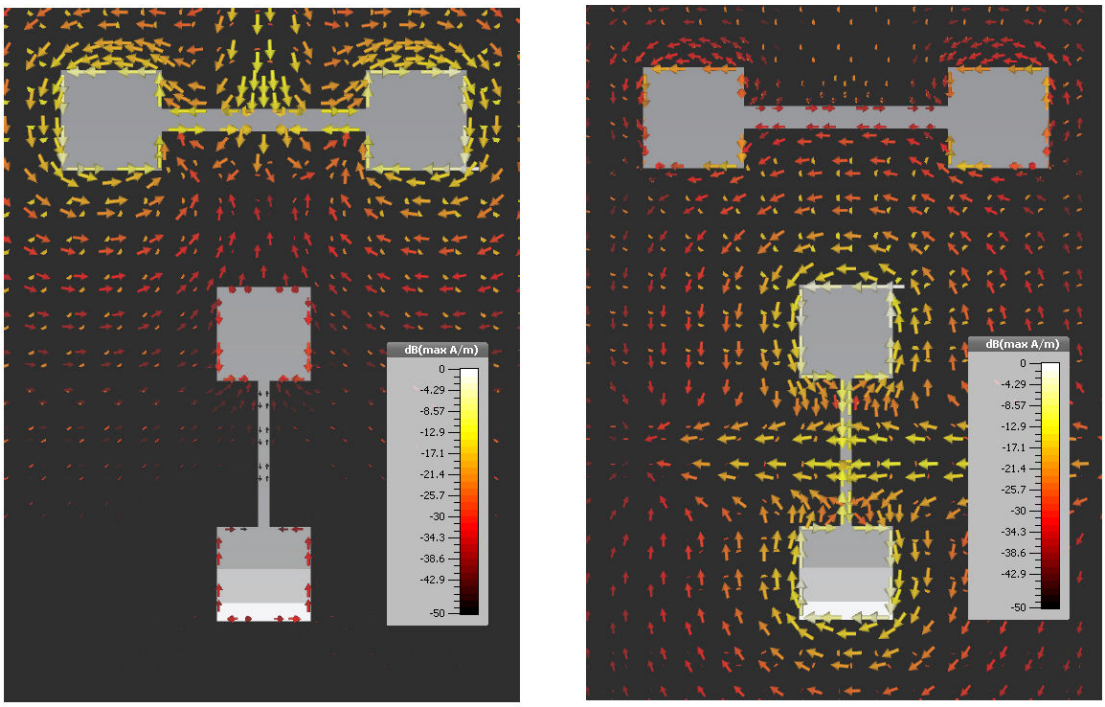

(a) (b)

Fig. 2.3: Vector current distribution on the ground plane of the designed single element; (a) Horizontal polarization is excited, (b) Vertical polarization is excited.

closed loop which can couple the power from transmission line through the slots to radiating patch. However, for the vertical polarization slot, the currents are in the same direction in parallel edges. The parallel current on the edges will cancel each other which results in a high level of isolation. A similar explanation is valid for exciting the vertical polarization.

The simulated reflection coefficient of the designed dual-polarized aperture coupled patch antenna for different scan angles in the $\varphi = 0°$ and $\varphi = 90°$ planes are shown in Fig. 2.4 and Fig. 2.5. The simulations are conducted by using periodic boundary conditions. The threshold for acceptable return loss in the scan angles is taken to be -10 dB. At the MPAR frequency of operation which is near 2.8 GHz, in the $\varphi = 0°$ plane for 47° off-broadside scan angle in horizontal

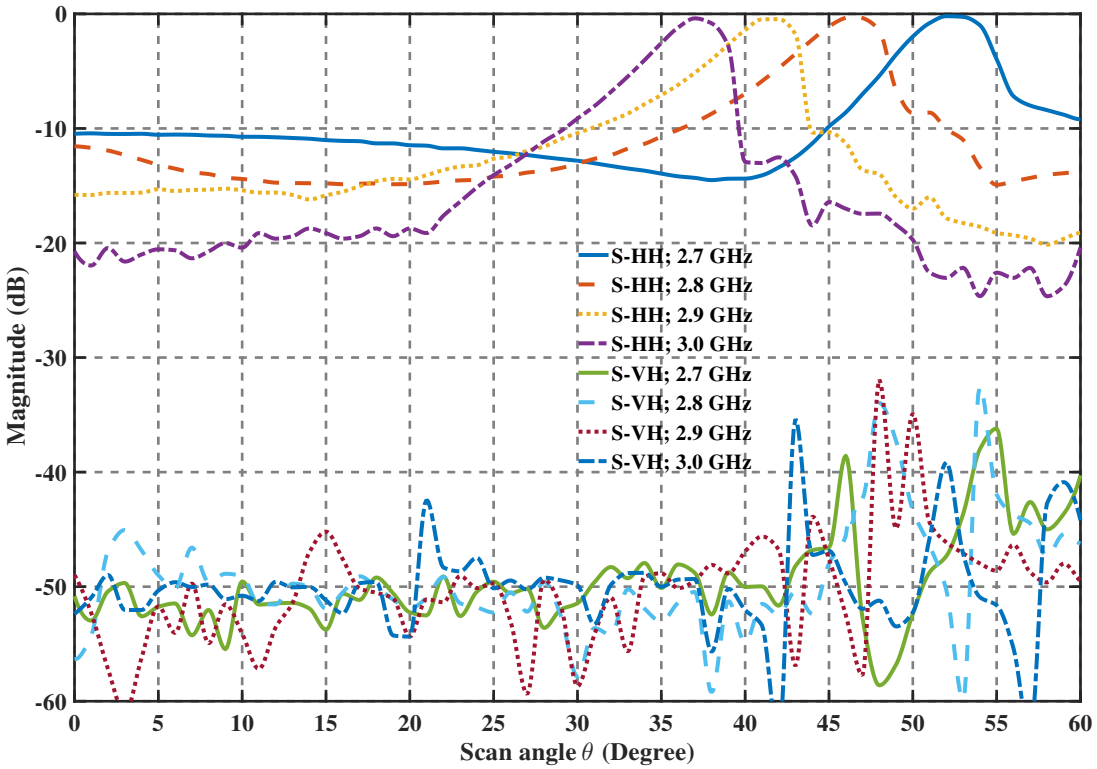

Fig. 2.4: Reflection coefficient magnitude versus scan angle in $\varphi = 0°$ plane for horizontal polarization.

polarization, the reflection coefficient approaches 0 dB and scan blindness happens. In $\varphi = 90°$ plane for 47° off-broadside scan angle in vertical polarization, the reflection coefficient approaches 0 dB. By considering the acceptable return loss in scan angle, the maximum scan angle at 2.8 GHz for both polarizations is 37°. The maximum scan angles for horizontal polarization at 2.7 GHz, 2.9 GHz, and 3.0 GHz are 45°, 31°, and 29°, respectively, and for vertical polarization are 46°, 32°, and 29°, respectively. The isolation between horizontal and vertical ports in the $\varphi = 0°$ and $\varphi = 90°$ planes for 0° to 60° scan angle are also shown in Fig. 2.4 and Fig. 2.5. Across the scan angle range from 0° to the maximum acceptable scan angle of each frequency, the isolation is always better than 40 dB.

The simulated normalized radiation pattern of the single element in $\varphi = 0°$

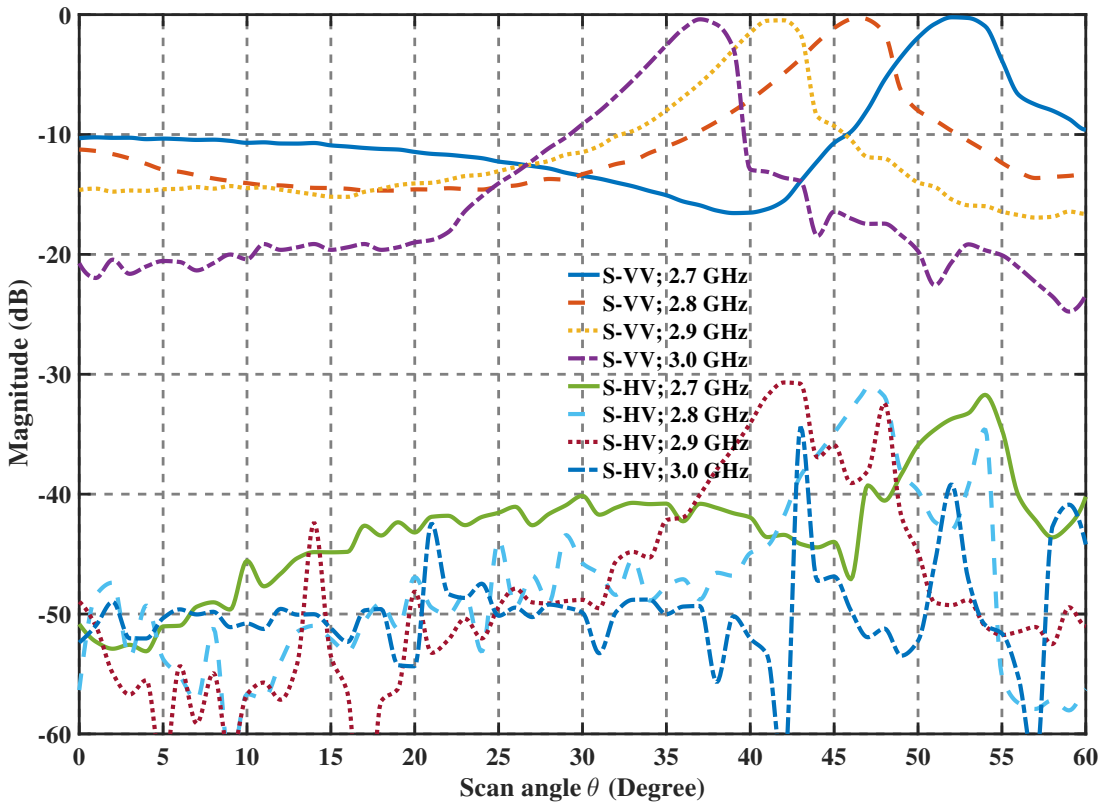

Fig. 2.5: Reflection coefficient magnitude versus scan angle in $\varphi = 90°$ plane for vertical polarization.

and $\varphi = 90°$ planes at 2.7 GHz, 2.8 GHz, 2.9 GHz, and 3.0 GHz for horizontal and vertical polarizations is shown in Fig. 2.6. In $\varphi = 0°$ plane, the cross-polarization level is lower than -38 dB for both polarizations. In $\varphi = 90°$ plane for horizontal polarization, the cross-polarization level is lower than -36 dB above the ground plane ($\theta_0 = -90°$ to $\theta = 90°$). For vertical polarization in $\varphi = 90°$ plane the cross-polarization level is -23 dB which is higher than the cross-polarization level of the same plane in horizontal polarization, however, there is -50 dB null in the cross-polarization pattern at the copolarization main beam axis.

In this section, the design and characterization of a low cross-polarization, high-isolation dual-polarized aperture-coupled microstrip patch antenna for MPAR application are presented. To improve the input isolation of the designed

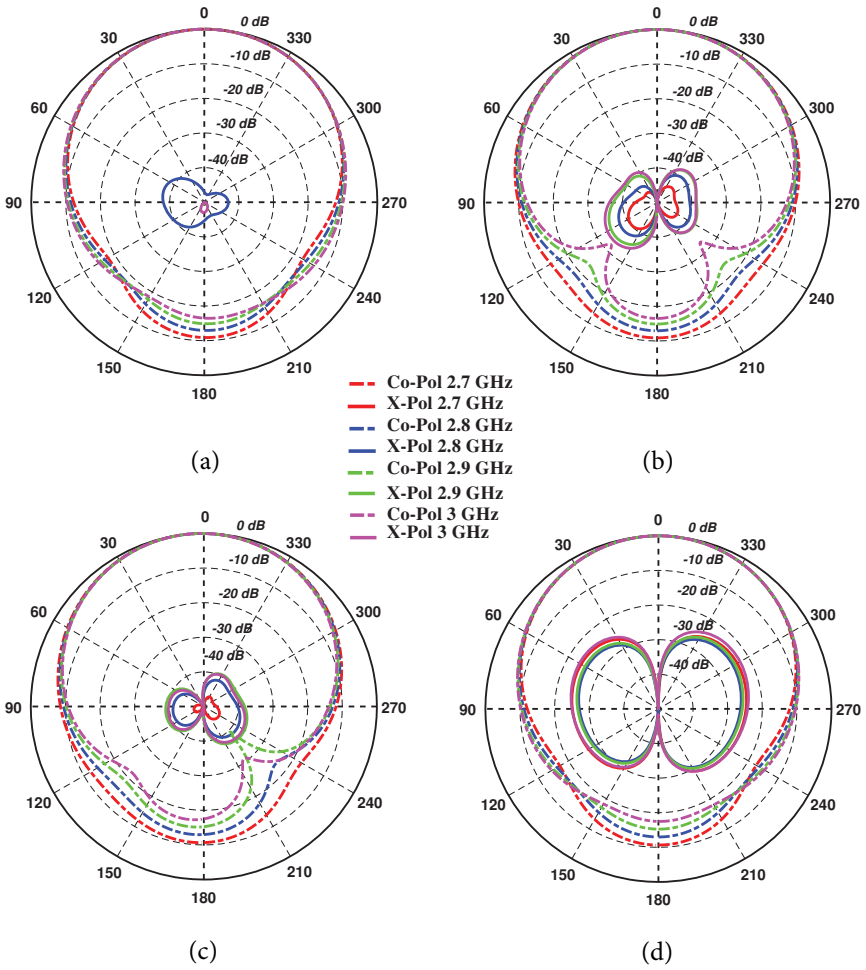

Fig. 2.6: Simulated co- and cross-polarization radiation pattern of designed single element; (a) Horizontal polarization $\varphi = 0°$ plane, (b) Horizontal polarization $\varphi = 90°$ plane, (c) Vertical polarization $\varphi = 0°$ plane, (d) Vertical polarization $\varphi = 90°$ plane.

single element, the two polarization are asymmetrically placed on the bottom layer of the antenna. As it will be explained in chapter 3, the geometrical asymmetry of the antenna will result in undesired side lobes if the array elements are configured into the identical subarrays for improving the final array cross-polarization level. Therefore, to improve the antenna performance, the electrical and geometrical symmetry of the single element need to be increased. Hybrid feed technique could be an ideal choice for increasing the antenna

geometrical symmetry. This method of excitation is implemented and discussed in section 2.2 and section 2.3.

2.2 Hybrid Feed Microstrip Patch Antenna Array; Balanced Probe-Feed and Symmetric Aperture Coupling Method

Dual-polarized microstrip patch antennas with hybrid feed design can be implemented in applications which require low cross-polarization and high isolation between horizontal and vertical polarizations. Compared to the dual-polarized differential feed design, the hybrid feed design requires less space for feed lines, which results in a more compact design. Also, the hybrid feed design provides a more symmetric feature which will improve the isolation between horizontal and vertical ports. In [10] a dual-polarized microstrip patch antenna is fed by two hybrid ports. These hybrid ports consist of two in-phase aperture-coupled feeds and two out-of-phase gap-coupled probe-feeds and the cross-polarization level of -20 dB and input isolation of -40 dB were realized. In [12] a dual-polarized patch antenna is fed by an aperture coupled feed and two capacitively coupled feeds of a 180-phase shift. In this design, the input isolation of -32 dB and cross-polarization level of -14.4 dB were reported. Considering its low cross-polarization and high input isolation, the hybrid feed design could be an ideal fit for MPAR applications. This design is being introduced for MPAR applications, and its potential deserves to be explored.

In the presented hybrid feed design in this dissertation, a dual-polarized patch antenna is excited by an aperture coupled feed and a differential probe feed. The measured input isolation of -43 is achieved. For further improvement in the cross-

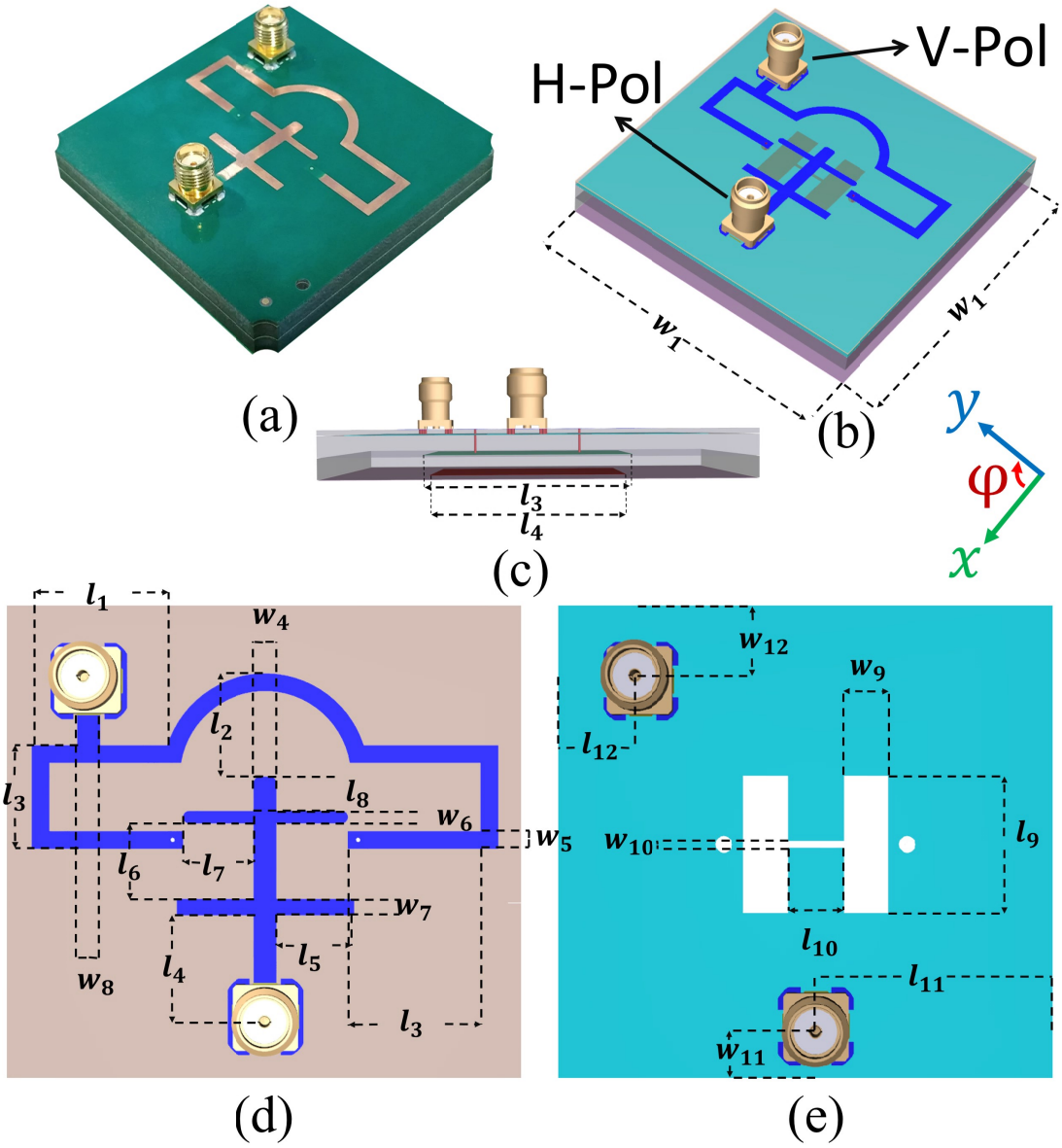

Fig. 2.7: (a) Photograph of the fabricated hybrid feed patch antenna, (b) 3-D view of the deigned single element, (c) side view of designed single element, (d) H-pol and V-pol feed lines, (e) Geometry of H-pol slot.

polarization levels, the image feed method has been implemented, resulting in measured cross-polarization levels as low as -37 dB.

The geometry of the designed and fabricated single dual-polarized patch antenna is shown in Fig. 2.7. As shown in Fig. 2.7 (b) the vertical polarization

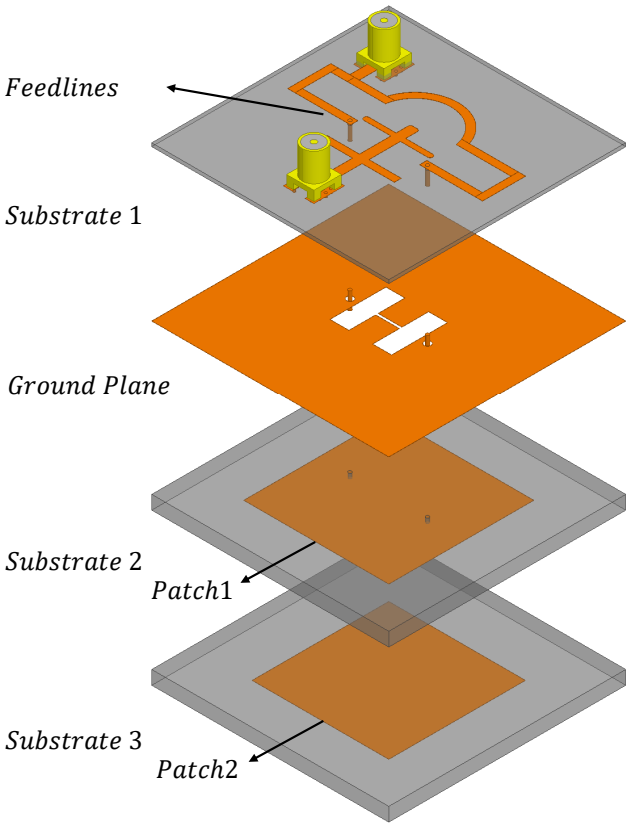

Fig. 2.8: Layer stack-up of designed single element.

is excited by a differential feed. The vertical polarization is excited by a pair of 180° out of phase currents to attain a low cross-polarization level by suppressing higher order modes[9]. In this design, the length of the transmission lines is adjusted to provide a 180° phase difference between two probes' currents. Having a 180° phase difference will suppress the vertical polarization cross-polarization and since the horizontal polarization feed line is symmetrically placed in the middle of the bottom layer, implementing differential feeding technique will increase the isolation between the horizontal and vertical polarizations. In other words, the due to having 180° phase shift between probes, the couple power form horizontal polarization to vertical polarization

probes cancel out each other. Therefore, it is expected to achieve high isolation between polarizations.

The material used for this design is Rogers RT/duroid 5880 with a dielectric constant of 2.2. As shown in Fig. 2.8, the feed lines are laid on the back side of the first substrate with the height of h_1. The ground plane and slots are laid on the front side of the first substrate. The first radiating patch is etched on the front side of the second substrate with a thickness of h_2. Since the microstrip patch antenna has a limited bandwidth, the stacked patch method is implemented and a parasitic square patch is placed on the front side of the third substrate with a height of h_3. The key parameters in this design are attained by optimization performed in CST Microwave Studio and ANSYS HFSS. The dimensions of the designed single element are listed in Table. 2.2.

The $\frown$-shaped part of the feed line increases the distance between the horizontal and vertical polarization feed lines, which will increase the isolation between the two polarizations. Also, since the 180° phase difference between two excitation probes is realized by the length difference of two arms of the vertical polarization transmission line, the $\frown$-shaped part of the feed line will increase the length of one arm, which will result in a more compact design.

The required length difference between the two arms of the vertical polarization transmission line is calculated analytically and then optimized in ANSYS HFSS. For a 1.7 mm width microstrip transmission line laid on a 1.574 mm thick Rogers RT/duroid 5880 with a dielectric constant of 2.2, the required length difference for a 180° phase shift (L) can be approximately calculated as follows [2]:

$$\varepsilon_{reff} = \frac{\varepsilon_r + 1}{2} + \frac{\varepsilon_r - 1}{2}\left[1 + 12\frac{h}{w}\right]^{-0.5} \tag{2.1}$$

$$\beta = \frac{2\pi}{\lambda} = \frac{2\pi f}{c}\sqrt{\varepsilon_{reff}} \tag{2.2}$$

$$L = \frac{\pi}{\beta} = \frac{c}{2f\sqrt{\varepsilon_{reff}}} \tag{2.3}$$

In which ε_r, ε_{reff}, and h are the dielectric constant, effective dielectric constant, thickness of the substrate, $c = 3 \times 10^8 \frac{m}{s}$, and $f = 2.8$ GHz, respectively, and w is the width of the transmission line. According to (2.3) the effective dielectric constant and required length difference at 2.8 GHz would be 1.77 and 40.2 mm, respectively. The length difference has been optimized in the final design in ANSYS HFSS and is reduced to 39.9 mm.

The horizontal polarization is excited through an H-shaped slot which is fed by a microstrip line laid below the ground plane. The H-shaped slot is placed exactly in the middle of the ground plane to increase the symmetry of radiation pattern. Although the spacing between vertical polarization probes and horizontal polarization feed line and slots is less than 1 mm, since the currents at the two probes are 180° out of phase, they cancel each other's coupling effect, which results in a high input isolation.

The simulated and measured reflection coefficient and input isolation between horizontal and vertical polarizations are shown in Fig. 2.9. As shown in Fig. 2.9 the simulated and measured S_{hh} and S_{vv} are below -10 dB from 2.7 GHz to 2.9 GHz, and there is a satisfactory agreement simulated and measured results. The isolation between horizontal and vertical ports is better than 45 dB in simulation and around 43 dB in measurement, indicating a very good agreement between

Table 2.2: Dimensions of the designed dual-polarized hybrid-fed antenna.

Parameter	Size	Parameter	Size
l_1	13.076 mm	w_1	55 mm
l_2	10 mm	w_2	55 mm
l_3	10 mm	w_3	2.2 mm
l_4	10.7 mm	w_4	1.7 mm
l_5	7.5 mm	w_5	1.2 mm
l_6	7.3 mm	w_6	1.6 mm
l_7	6.9 mm	w_7	2.2 mm
l_8	3.3 mm	w_8	4.4 mm
l_9	12.9 mm	w_9	0.6 mm
l_{10}	13 mm	w_{10}	12 mm
l_{11}	5.5 mm	w_{11}	13.35 mm
l_{12}	27.5 mm	w_{12}	12.9 mm
h_1	1.574 mm	$W_{Antenna}$	55 mm
h_2	3.175 mm	W_{patch1}	24.4 mm
h_3	3.175 mm	W_{patch2}	27.2 mm

simulated and measured results.

The simulated reflection coefficient of the proposed hybrid feed patch antenna at the scan angles in $\varphi = 0°$ and $\varphi = 90°$ planes are shown in Fig. 2.10 and Fig. 2.11, respectively. The minimum required reflection coefficient is taken to be -10 dB for the intended scan volume. For a four-faced planar array antenna or a cylindrical array antenna which has a 90° active sector, the minimum required scanning angle is 45°. As shown in Fig. 2.10 and Fig. 2.11 in the $\varphi = 0°$ and $\varphi = 90°$ planes at the entire frequency band the reflection coefficients for horizontal and vertical ports remain under -10 dB across the scan angle from 0°

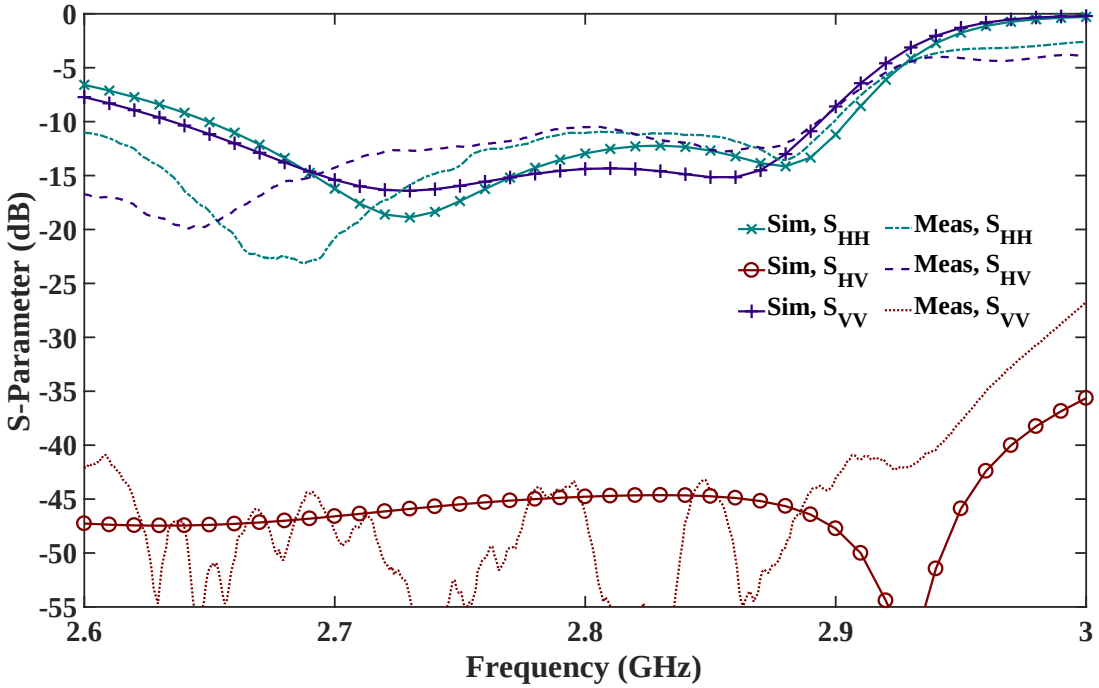

Fig. 2.9: Simulated and measured reflection coefficient and isolation of horizontal and vertical ports of a designed single element.

to 45°, except S_{VV} at 2.8 GHz in $\varphi = 90°$ plane which approaches -10 dB at 43° scan angle.

The co and cross-polarization radiation pattern of the horizontal and vertical polarizations at 2.7 GHz, 2.8 GHz and 2.9 GHz in $\varphi = 0°$ and $\varphi = 90°$ planes are shown in Fig. 2.12. In $\varphi = 0°$ plane the cross-polarization level above the ground plane is better than -48 dB for horizontal polarization and -39 dB for vertical polarization. In $\varphi = 90°$ plane the maximum cross-polarization level above the ground plane is -39 dB and -32 dB for horizontal polarization and vertical polarization, respectively.

The presented design in this section possesses the advantages of a very symmetric geometry, low cross-polarization level, and high input isolation. In the presented design the number of layers is reduced. Also, the antenna fabrication cost and complexity and can be improved by changing material to

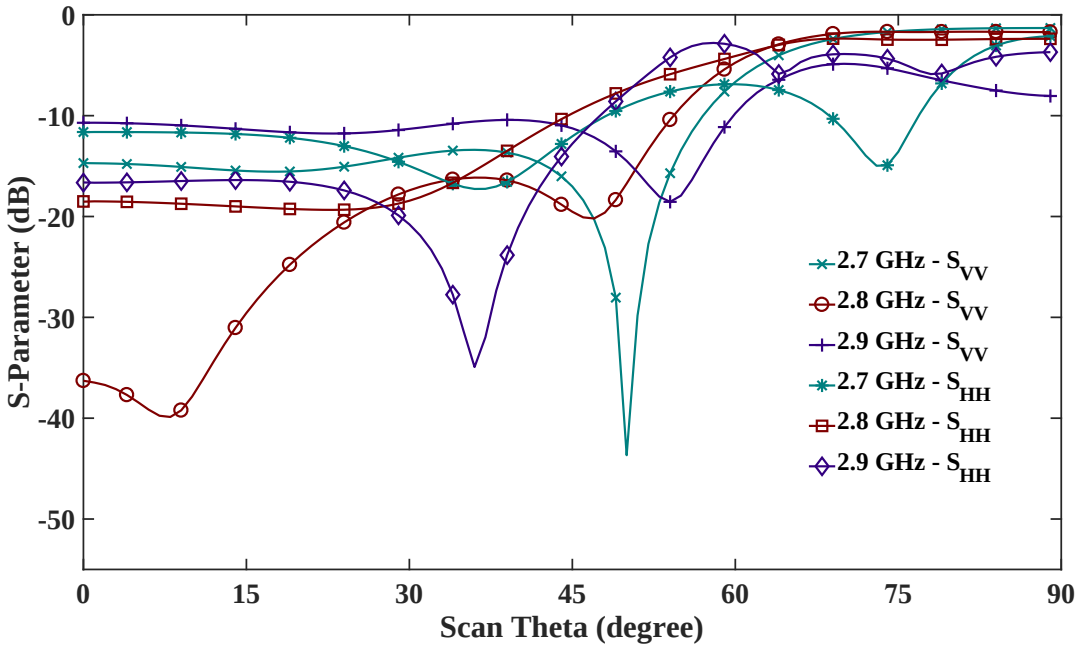

Fig. 2.10: Reflection coefficient magnitude versus scan angle in $\varphi = 0°$ plane for horizontal and vertical polarizations.

non-Teflon based material. The multilayer blind vias which excite the radiation patch antenna can be removed if the balanced probe feeding method is replaced with aperture coupling method. Considering the aforementioned changes for improving the antenna performance, the second hybrid feed patch antenna is designed and the detailed discussion is presented in the section 2.3.

2.3 Hybrid Feed Microstrip Patch Antenna; Balanced and Symmetric Aperture Coupling Method

The layer stack up and geometry of the proposed dual-polarized patch antenna is presented in Fig. 2.13. As seen in Fig. 2.13, the feed lines for both horizontal and vertical polarizations are placed on the top layer of the first substrate. To achieve the maximum bandwidth and having the minimum surface wave effect on the array

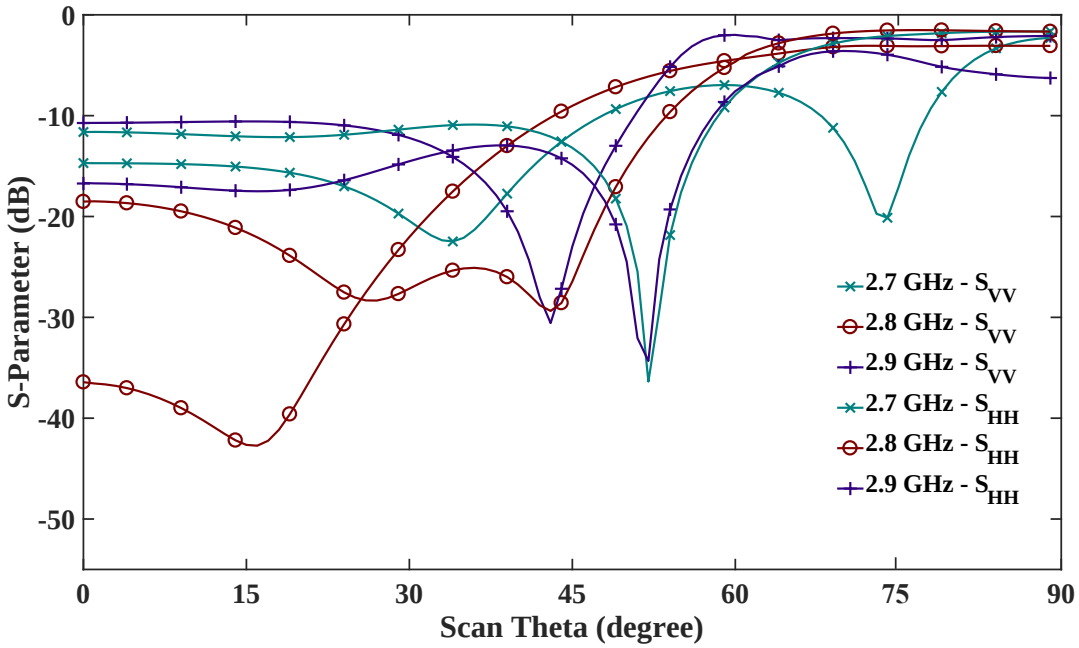

Fig. 2.11: Reflection coefficient magnitude versus scan angle in $\varphi = 90°$ plane for horizontal and vertical polarizations.

radiation pattern, it is always desired to implement a material with low dielectric constant. However, using substrates with a low dielectric constant will increase the dimension of the unit cell. Also, since low dielectric constant materials such as Rogers 5880 are based on PTFE composites, special treatment for metalized holes is required. In this design, a 0.813 mm thick Rogers 4534 laminate with a dielectric constant of 3.4 is chosen for the first substrate which contains feed lines and metalized holes for connectors. The ground plane which includes three slots is placed on the bottom layer of the Rogers 4534 laminate. The radiating square patch and the parasitic square patch are placed on the bottom layer of the second and third laminates which are 3.175 mm thick Rogers 5880. In the proposed design, a low dielectric material is used to achieve the required bandwidth for multifunction applications and Rogers 4534 with the higher dielectric material is used for reducing the size of the transmission lines and ease of fabrication [37],

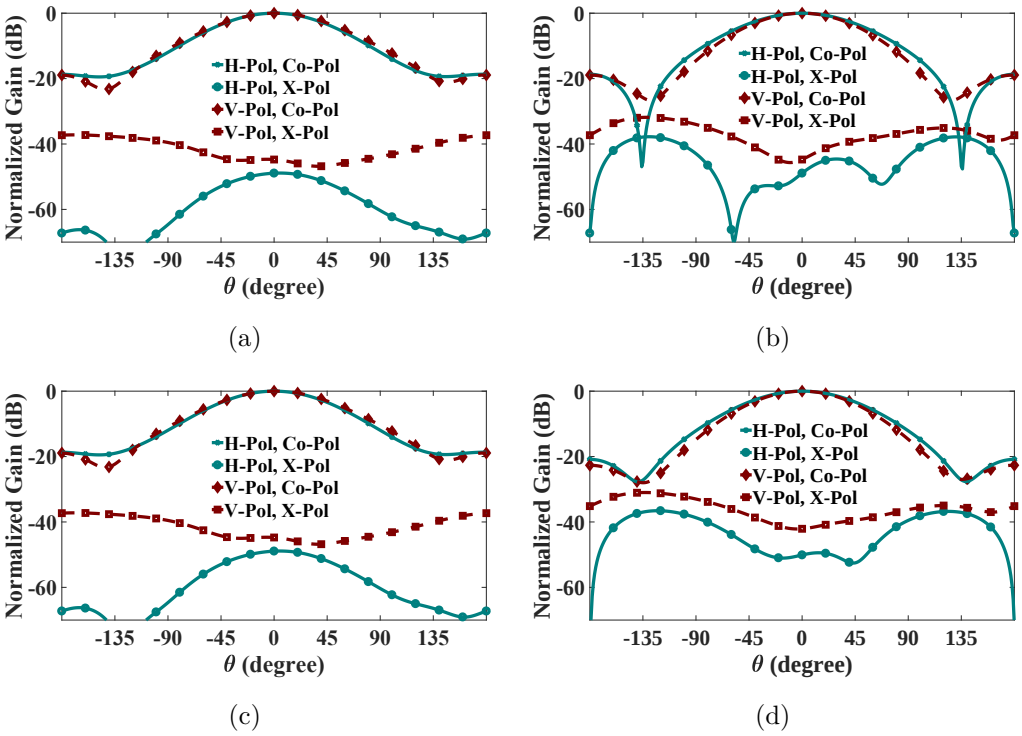

Fig. 2.12: Simulated normalized radiation pattern of designed single element; (a) 2.7 GHz, $\varphi = 0°$, (b) 2.7 GHz, $\varphi = 90°$, (c) 2.8 GHz, $\varphi = 0°$, (d) 2.8 GHz, $\varphi = 90°$,(e) 2.9 GHz, $\varphi = 0°$, (f) 2.9 GHz, $\varphi = 90°$.

[38].

Fig. 2.15 shows the current distribution of the excitation feed lines and slots while the horizontal polarization port is excited and vertical polarization port is terminated. The presented current distribution in Fig. 2.14 is based on the simulations that have been carried out using CST Microwave studio. As seen in Fig. 2.14, the horizontal polarization feed line and corresponding H-shaped slot are placed in the middle of the antenna [7], [39]–[41]. The horizontal polarization slot is symmetric with respect to horizontal and vertical planes and it is placed exactly in the middle of the ground plane. In the proposed patch antenna, when the horizontal peroration is excited, the current distribution around the edges of the corresponding slot will form a closed loop which can couple the power

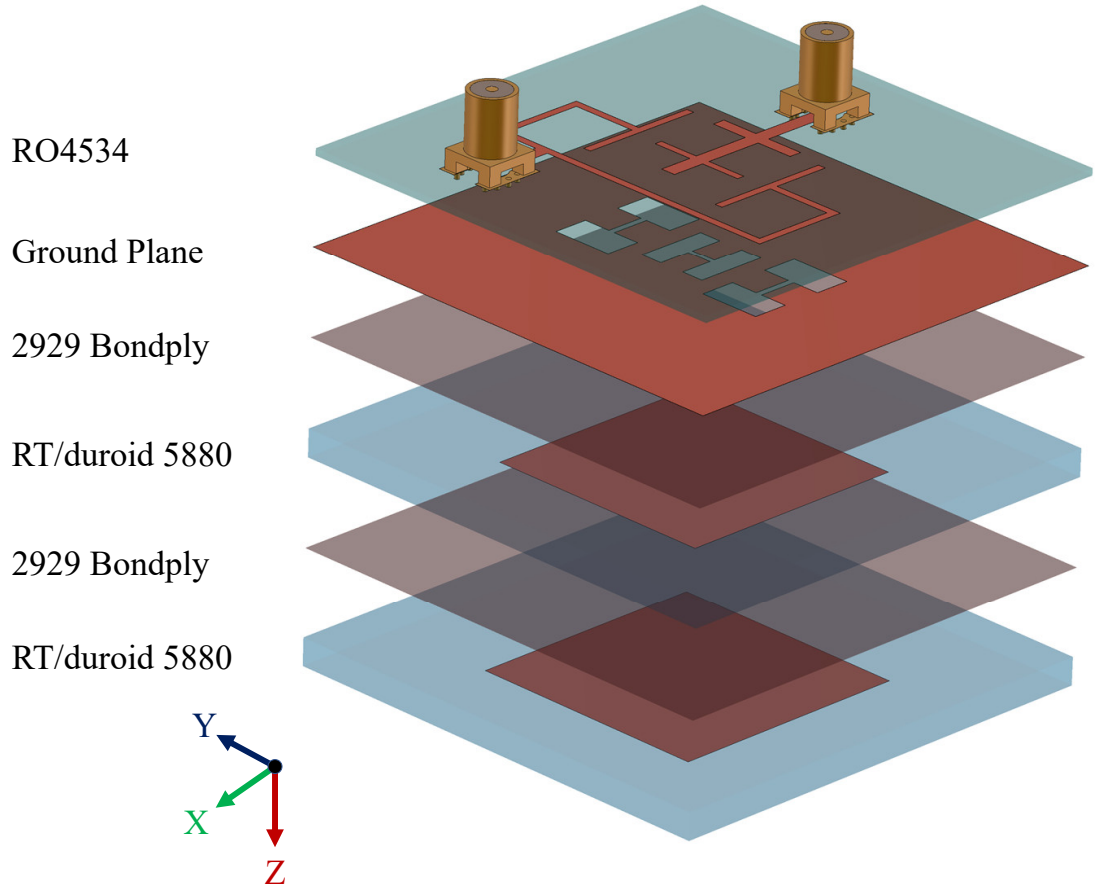

Fig. 2.13: Layer stack up of the proposed dual-polarized microstrip patch antenna.

to radiating patch antenna through the slot. On the other hand, the current distribution around the parallel edges of vertical polarization slots is oriented in the same direction. Having the parallel current distribution on the edges of the slot avoids the radiation of the orthogonal polarization which results in a high input isolation and low cross-polarization level.

Fig. 2.16 shows the current distribution of the excitation feed lines and slots while the vertical polarization port is excited and horizontal polarization port is terminated. One of the key points in design and development of the low cross-polarization and high-isolation patch antennas is to increase the symmetry of design. As mentioned above, the horizontal polarization slot is designed to be

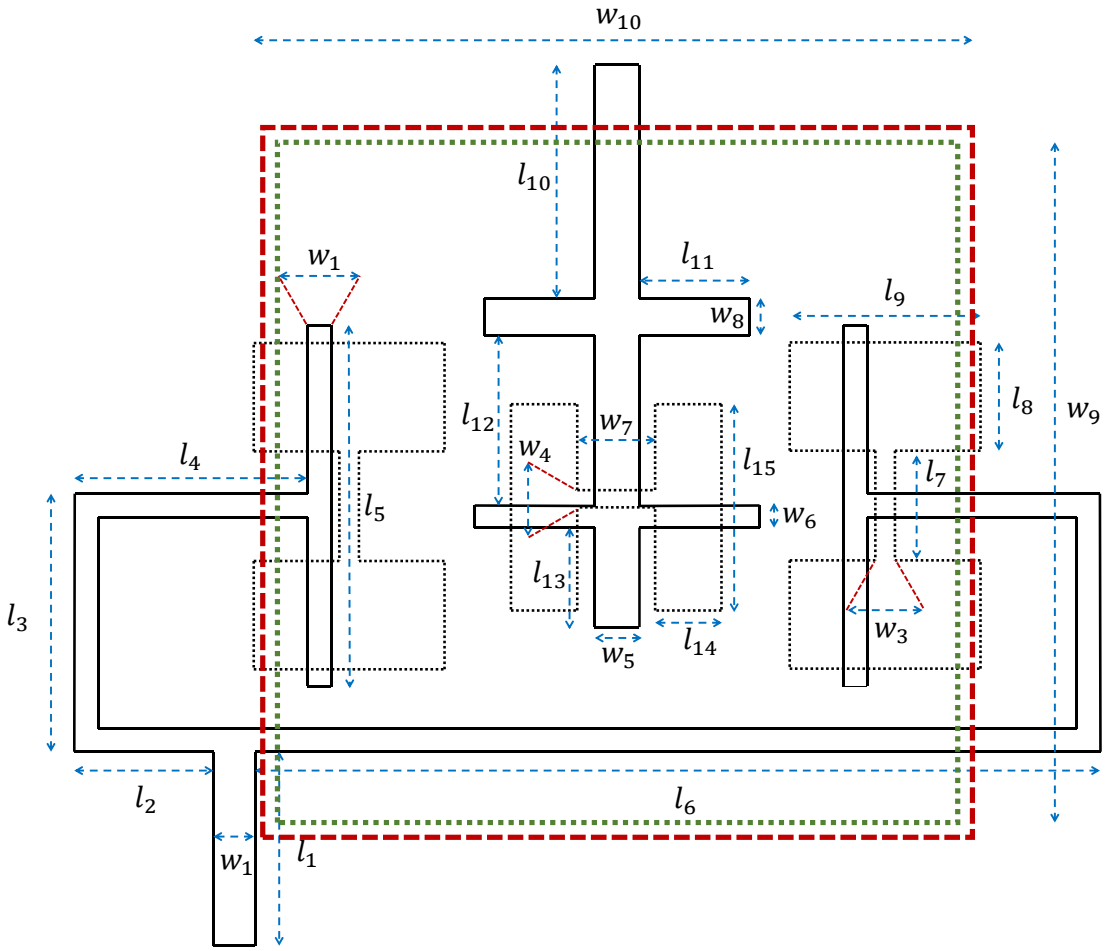

Fig. 2.14: Design parameters of proposed dual-polarized patch antenna listed in Table. 2.3.

in the middle of the ground plane, therefore the only way to maintain the symmetry of the design without having a complicated multilayer design is to excite the vertical polarization through differential feed method. To implement the differential feeding method, two similar H-shaped slots are placed beside the horizontal polarization slot. In the presented differential feed method, in order to suppress the higher order modes and reduce the cross-polarization level, the two slots are excited with 180° phase shift [9], [42]. As seen in Fig. 2.16, the required 180° phase shift for differential feed method is produced through the

Table 2.3: Dimensions of the proposed hybrid aperture-coupled antenna.

Parameter	Size	Parameter	Size
l_1	13.076 mm	w_1	55 mm
l_2	10 mm	w_2	55 mm
l_3	10 mm	w_3	2.2 mm
l_4	10.7 mm	w_4	1.7 mm
l_5	7.5 mm	w_5	1.2 mm
l_6	7.3 mm	w_6	1.6 mm
l_7	6.9 mm	w_7	2.2 mm
l_8	3.3 mm	w_8	4.4 mm
l_9	12.9 mm	w_9	0.6 mm
l_{10}	13 mm	w_{10}	12 mm
l_{11}	5.5 mm	h_1	13.35 mm
l_{12}	27.5 mm	h_2	12.9 mm
l_{13}	1.574 mm	h_3	55 mm
l_{14}	3.175 mm	h_4	24.4 mm
l_{15}	3.175 mm	h_5	27.2 mm

length difference of the two branches of vertical polarization excitation feed line. Similar to the H-pol excitation, the currents along the parallel edges of two excited slots are in opposite direction and form a closed loop current, however, the currents along the parallel edges of horizontal polarization are in opposite direction

Multifunction phased array radar is intended to integrate united states four networks of radar systems. The allocated bandwidth for MPAR operation when replacing ASR and TDWR is 2.7-2.9 GHz [43]. The impedance bandwidth of microstrip patch antenna is typically 3% percent. Different bandwidth

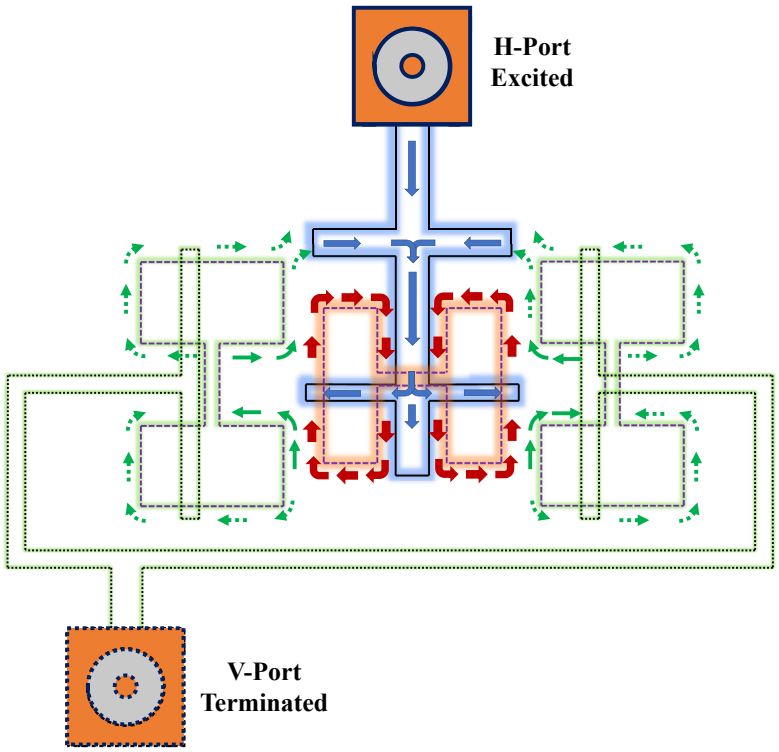

Fig. 2.15: Current distribution on the excitation feedline and ground plane with the H-pol excitation.

enhancement methods have been proposed and multilayer configuration approach is implemented in this design [44]. In the proposed design, a parasitic square patch with the smaller dimensions is placed on top of the radiating square patch. For bonding three different laminates, Rogers 2929 Bondply with a dielectric constant of 2.9 and thickness of 0.076 mm is used. The simulated and measured return loss and coupling between horizontal and vertical ports are provided in Fig. 2.17. As seen in Fig. 2.17, there is an almost perfect agreement between simulated and measured return loss results. The return loss for both polarizations is below -12 dB in the entire frequency band (2.7-2.9 GHz). Also, it is worth noting that the horizontal and vertical polarization return loss results are pretty similar which decrease the gain mismatch between two polarizations. As shown in Fig. 2.17, the isolation between horizontal and vertical

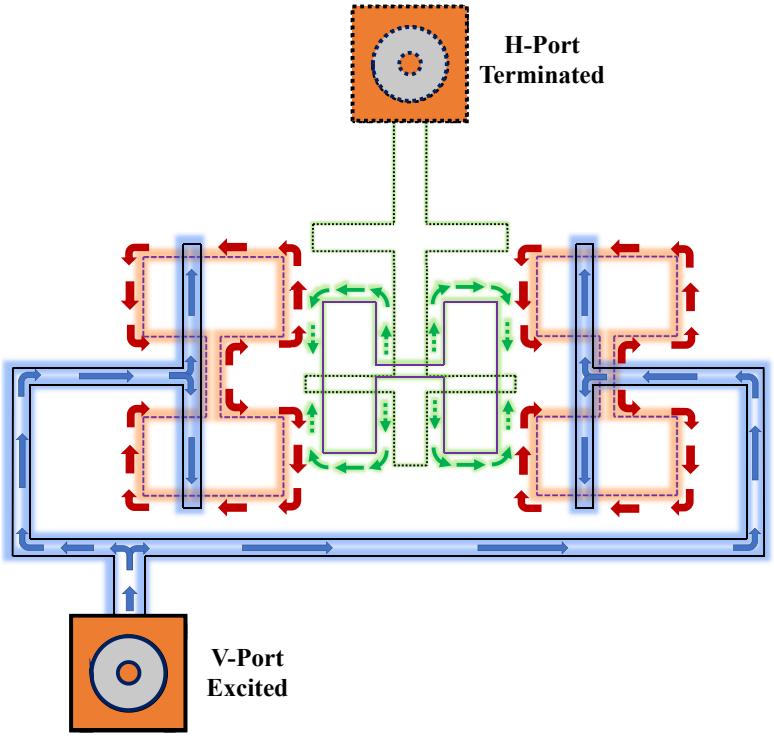

Fig. 2.16: Current distribution on the excitation feedline and ground plane with the V-pol excitation.

polarizations is better than 52 dB in simulations. To measure such low coupling between ports, the s-parameter measurements are conducted in shielded anechoic chambers designed for S-parameter measurements. As seen in Fig. 2.17, we managed to measure an isolation level of better than 50 dB in the entire frequency band.

One of the most important and interesting aspects of using phased array antenna instead of conventional reflector antennas is the electronic beam steering of the phased array antennas. However, not only the radiation characteristic of the array but also the return loss and coupling between two polarizations depend on the scan angle. To minimize the effect of beam steering on array radiation pattern, conformal geometries such as cylindrical array antenna could be an ideal choice [45]. Due to symmetric properties of the

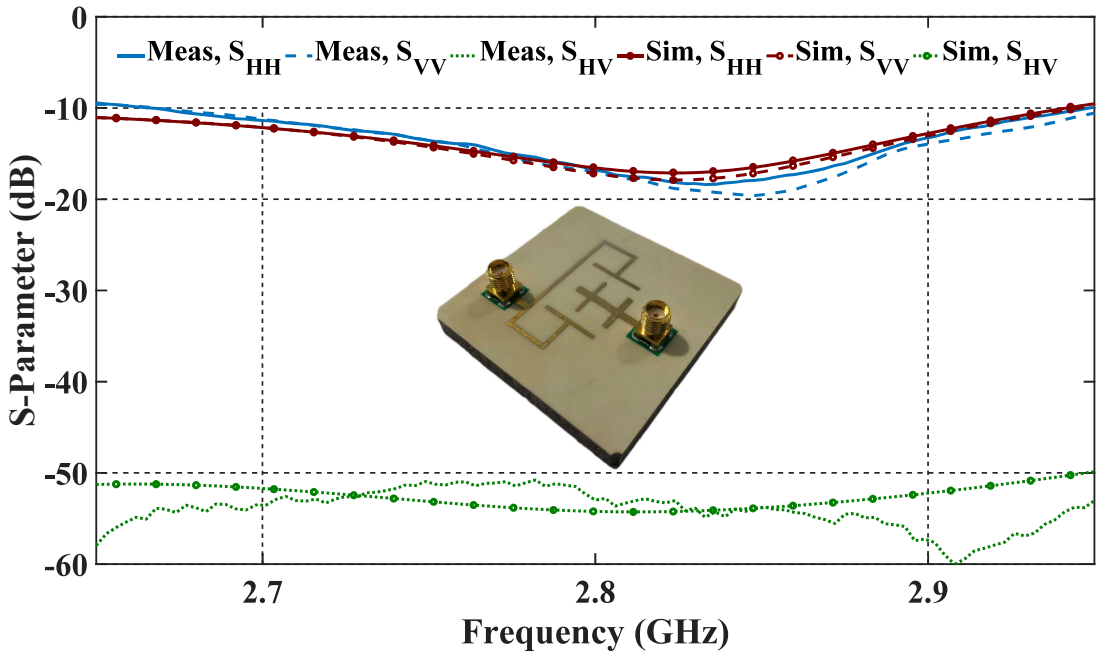

Fig. 2.17: Simulated and measured reflection coefficient and isolation of horizontal and vertical ports of the designed single element.

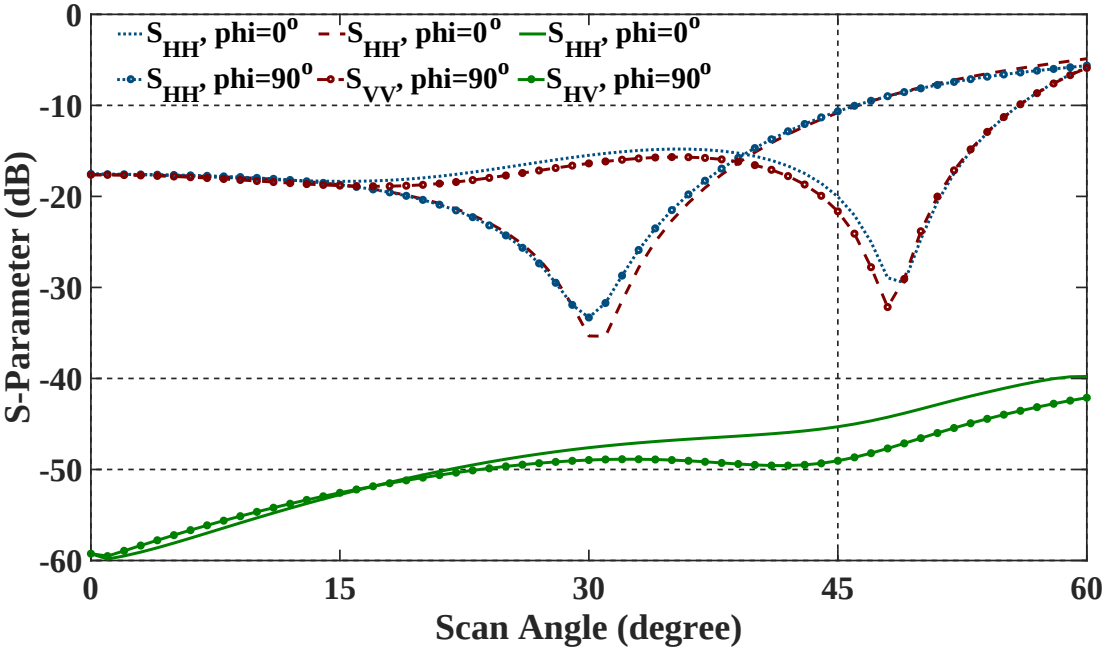

Fig. 2.18: Simulated reflection coefficient and isolation between horizontal and vertical ports versus scan angle in $\varphi = 0°$ and $\varphi = 90°$ planes.

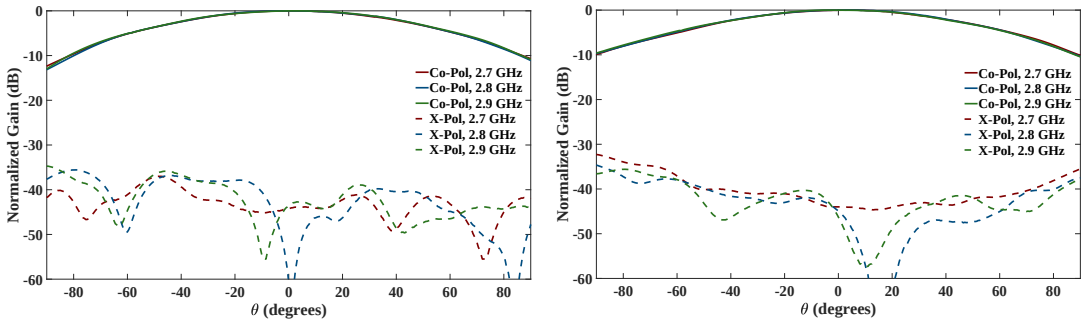

(a) (b)

Fig. 2.19: Measured radiation pattern of the designed single element at 2.7 GHz, 2.8 GHz, and 2.9 GHz; (a) H-pol, $\varphi = 0°$; (b) H-pol, $\varphi = 90°$.

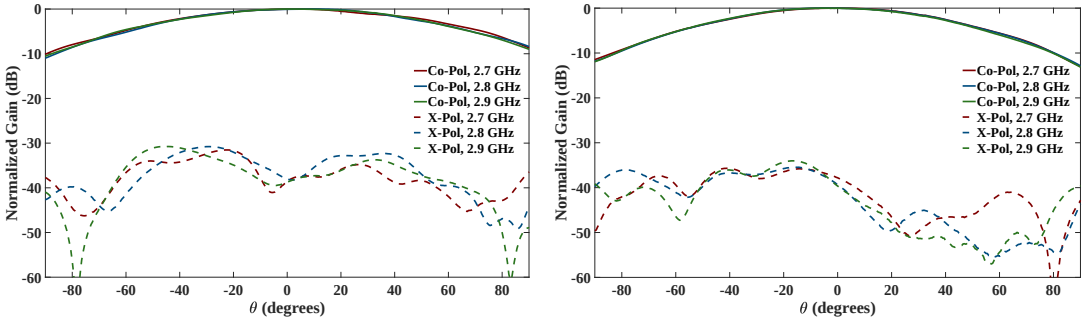

(a) (b)

Fig. 2.20: Measured radiation pattern of the designed single element at 2.7 GHz, 2.8 GHz, and 2.9 GHz; (a) V-pol, $\varphi = 0°$; (b) V-pol, $\varphi = 90°$.

cylindrical array antenna around the corresponding cylinder axis, it can offer azimuthally scan invariant radiation pattern. Therefore, beam steering in phased array antennas is only required in the elevation direction. Subsequently, since the off-principle plane beam steering is eliminated with cylindrical geometry, the alteration of co and cross-polarization radiation pattern could be tolerated.

In phased array antennas, scan blindness could result in limited scanning angle range. One explanation for the scan blindness is the presence of dielectric or metallic material in the antenna plan which can support surface waves. The exact location of the occurrence of the scan blindness depends on the spacing between

elements, array configurations, and element design. Using high dielectric constant material, increasing the spacing between elements or using subarrays could move the blind angle towered the broadside [36], [46]. The blind angel is the scan angle in which the reflection coefficient approaches to zero, however, since the antenna is required to efficiently radiate the input power, therefore the minimum acceptable return loss is taken to be -10 dB. The designed single element is simulated with a periodic boundary condition at different scan angles and the resulted s-parameters are presented in Fig. 2.18.

Fig. 2.18 shows the return loss and isolation of horizontal and vertical polarization versus scan angles in $\varphi = 0^\circ$ and $\varphi = 90^\circ$ planes. As seen in Fig. 2.18, at the MPAR frequency of operation, which is close to 2.8 GHz, the return loss for both polarizations stays below -10 dB while scanning up to 45° in both $\varphi = 0^\circ$ and $\varphi = 90^\circ$ planes. The isolation between horizontal and vertical polarization in the required scanning range is better than 45 dB.

The simulated and measured radiation patterns of the proposed dual-polarized hybrid feed aperture-coupled microstrip patch antenna are presented in Fig. 2.19 and Fig. 2.20. The antenna radiation pattern is measured in the far-field anechoic chamber of ARRC. The measured cross-polarization level of horizontal polarization in $\varphi = 0^\circ$ and $\varphi = 90^\circ$ planes are shown in Fig. 2.19 (a) and Fig. 2.19 (b), respectively. For the horizontal polarization, the maximum cross-polarization level of the designed single element at 2.8 GHz is below -36 dB and -35 dB in $\varphi = 0^\circ$ and $\varphi = 90^\circ$ planes, respectively. As shown Fig. 2.20 (a) and Fig. 2.20 (b), the measured cross-polarization level with the V-Pol excitation at 2.8 GHz is better than -30 dB and -36 dB in $\varphi = 0^\circ$ and $\varphi = 90^\circ$ planes, respectively.

Based on the presented single elements measured results, in the final array

design, the cross-polarization level should be reduced. Implementing image configuration in the array design is a well-accepted approach for decreasing the cross-polarization level. The challenges and limitations of utilizing image configuration in the large phased array antennas is discussed in the chapter 3.

Chapter 3

Challenges and Limitations of the Cross-Polarization Suppression in Dual-Polarization Antenna Arrays using Identical Subarrays

Cross-polarization suppression in dual linear-polarization antenna arrays using identical 2×2-element subarrays is a well-known method and discussed in Ref. [47]. In the reference paper, the array radiation pattern is calculated by decomposing a single element radiation pattern to its even and odd components. According to the mentioned paper, the side lobe issue associated with this method can be resolved by using configuration D. However, in this chapter, it is shown that the decomposition method has fundamental limitations and cannot be used for calculating the radiation pattern of identical subarrays. Also, it is shown that configuration D is not solving the side lobe problem. However, the sidelobe level can be improved by using other methods.

Cross-polarization suppression by using image arrangement has been implemented in many designs [43], [48]–[52]. According to Woelder et al. in Ref. [53], the radiation pattern of an array antenna made of 2×2-element subarrays can be calculated by separating the single element radiation pattern to its even and odd components. The main concern about the results provided in [53] is that all the calculations are based on the isolated element pattern obtained from

measuring the radiation pattern of a single probe-fed patch antenna on a 0.75 m $\times$ 0.75 m ground plane. First, the radiation pattern of an element in an array is different from the isolated element pattern. To better predict the array radiation pattern, the embedded element pattern that contains the coupling effects of the adjacent element should be utilized. The embedded element pattern is defined as the radiation pattern of the center element in an array of unique elements. However, in the 2×2-element subarray, the array elements are mirrored, and the relative location of H and V ports are changed, leading the change of the radiation pattern. Consequently, calculation of the radiation pattern of an array of similar 2×2-element subarrays becomes a complicated problem.

The full-wave method can be used for simulation of small array antennas. However, for large antenna arrays, which cannot be simulated with full-wave methods, this problem is more severe. The decomposition approach and the results presented in [53] will be discussed in this chapter. It is shown that the calculated radiation patterns of the 2×2-element subarray based on the measured or simulated radiation pattern of a single element are not accurate enough. It is shown that the presented results regarding the sidelobe suppression by using configuration D are not generally true, and this error is caused by the deficiency of the pattern decomposition method, and undesired sidelobes still exist.

This chapter is organized as follows: In section 3.1, the issues and limitations of calculating the radiation pattern of dual-polarization array antennas by using even and odd decomposition method are discussed. In section 3.2, the interelement coupling and subarray arrangements effects on subarray and array radiation patterns are discussed. In this section, a precise method for calculating the radiation pattern of the arrays of identical subarrays with image

arrangement is introduced, and the radiation pattern of different 2×2-element subarrays with image configuration are compared. In section 3.3, the limitations of using image configuration are illustrated and discussed in detail. The solution and optimum design for a large phased array antenna are presented in section 3.4. Finally, the summary is provided at the end of this chapter.

3.1 Issues With Even and Odd Component Decomposition Method

A well-known method for cross-polarization suppression in dual-polarized array antennas is image arrangement in which elements are arranged into the group of 2×2-element subarrays [52], [53]. Fig. 3.1 shows four different forms of 2×2-element subarrays in which either horizontal ports or vertical ports or both are mirrored regarding horizontal and vertical planes. The mirrored ports will be excited with 180° phase shift, so the mirrored elements copolarization radiation patterns will be in-phase, and cross-polarization radiation patterns will be 180° out of phase compared to the reference element in the subarray. This will result in cross-polarization suppression especially in principle planes. Based on simulation and measurement results in [53], using image configuration will result in improving the cross-polarization level, however, it could cause undesired side lobes if configuration B or C is used. Based on calculated results in [53] the cross-polarization and side lobe level suppression is possible by using configuration D. The cross-polarization suppression by using image configuration has been studied in different articles, and the presented results show that configuration D has the best performance compared to other 2×2 configurations. However, configuration C provides more geometrical symmetry which makes this configuration an exciting choice if the side lobe issue can be

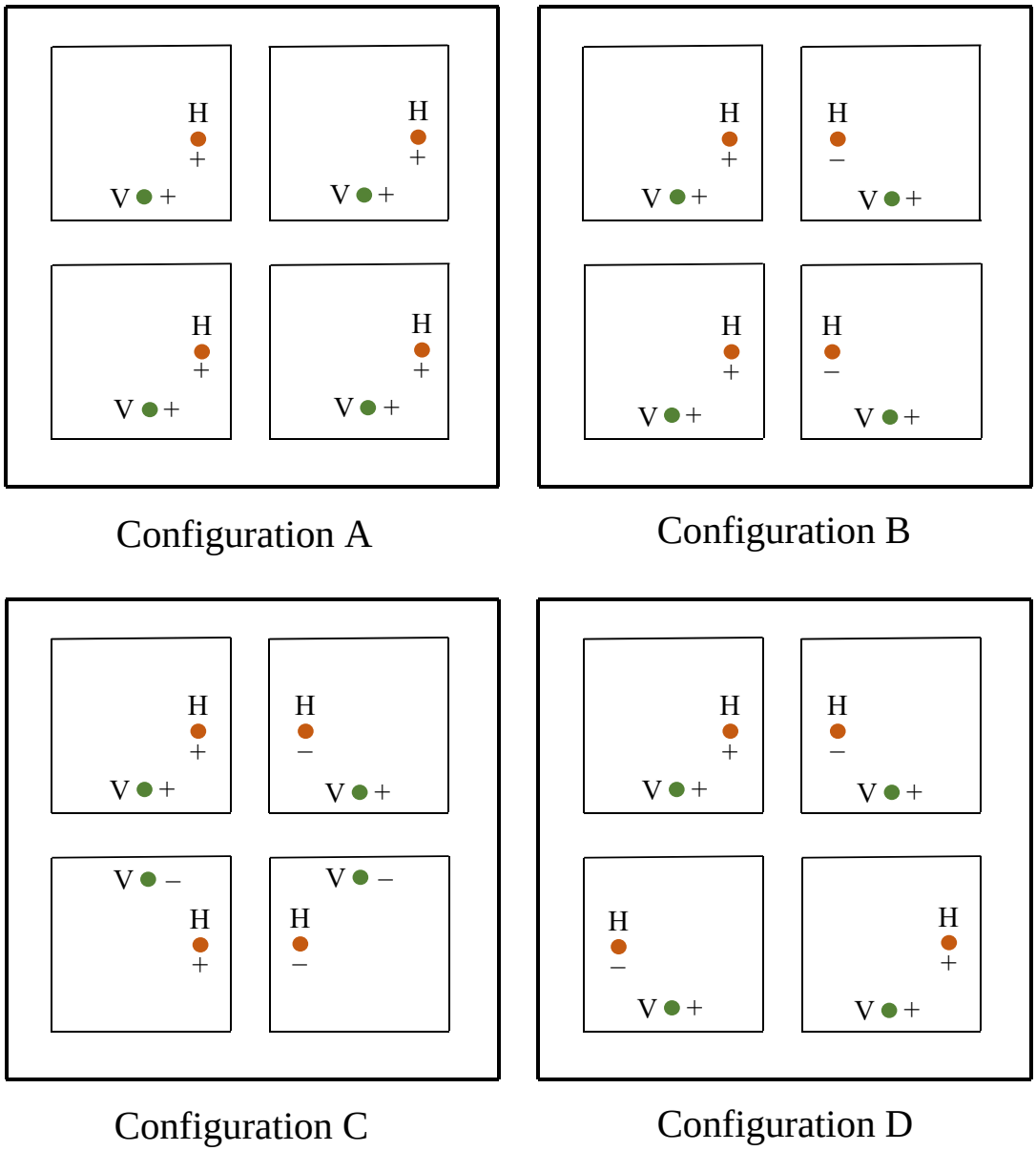

Fig. 3.1: 2×2-element subarray configuration for cross-polarization suppression. The ports marked with "-" are excited with a 180° phase shift with respect to the ports marked with "+" [54].

avoided.

The calculated radiation patterns of configuration B, C, and D in [53] are based on the measured radiation pattern of a single isolated probe-fed patch antenna. To calculate the radiation pattern of the 2×2-element subarray, the

single element horizontal and vertical polarizations co and cross-polarization patterns are decomposed to their even and odd components. Then the radiation patterns of other mirrored elements in the subarray are calculated based on the separated even and odd components, the excitation phase, and relative location of H and V ports. There are two main concerns about the results calculated with this approach. First, in this method, the isolated element radiation pattern is used which does not contain the coupling effect of other elements. The second issue with calculated radiation patterns using this method is that since the elements in the 2 × 2-element subarray are not identical, and the adjacent elements of each element of the 2 × 2-element subarray have different orientation, one element pattern regardless of being isolated element pattern or embedded element pattern, cannot be used for calculating the radiation pattern of the embedded 2 × 2-element subarray. This means that the calculated results in [53] are not generally true. To prove this claim, the radiation pattern of a 2 × 34-element array of a probe-fed patch antenna configured according to configuration D is calculated using two methods. The first method is based on separating the single element pattern to its even and odd component and then calculating the 2 × 2-element array radiation pattern. The second method is based on a full-wave simulation result which is a perfectly acceptable approach.

Assuming the antenna is placed in the x-y plane and antenna boresight is in the z-direction, the even and odd components of the antenna radiation pattern can be written as follows:

$$\begin{aligned} E_{H,V}^{even}(\theta,\varphi) &= \frac{E_{H,V}(\theta,\varphi)+E_{H,V}(\theta,\pi-\varphi)}{2} \\ E_{H,V}^{odd}(\theta,\varphi) &= \frac{E_{H,V}(\theta,\varphi)-E_{H,V}(\theta,\pi-\varphi)}{2} \end{aligned} \tag{3.1}$$

And following the same procedure in [53], the radiation pattern of the upper left $E_L(\theta,\varphi)$ and right $E_R(\theta,\varphi)$ elements in the 2×2-element subarray can be written as follows:

$$E_L(\theta,\varphi) = \begin{Bmatrix} E_E^h(\theta,\varphi) = E_E^{he}(\theta,\varphi) + E_E^{ho}(\theta,\varphi) \\ E_E^v(\theta,\varphi) = E_E^{ve}(\theta,\varphi) + E_E^{vo}(\theta,\varphi) \end{Bmatrix} \tag{3.2}$$

$$E_R(\theta,\varphi) = \begin{Bmatrix} E_E^h(\theta,\varphi) = -E_E^{he}(\theta,\varphi) + E_E^{ho}(\theta,\varphi) \\ E_E^v(\theta,\varphi) = \quad E_E^{ve}(\theta,\varphi) - E_E^{vo}(\theta,\varphi) \end{Bmatrix} \tag{3.3}$$

In which $E_E^{he}(\theta,\varphi)$ and $E_E^{ho}(\theta,\varphi)$ are the even and odd components of horizontal polarization radiation pattern and $E_E^{ve}(\theta,\varphi)$ and $E_E^{vo}(\theta,\varphi)$ are the even and odd components of the vertical polarization radiation pattern.

The radiation pattern of upper two elements of the subarray with configuration D can be written as follows:

$$\begin{aligned} E_{2\times1,U}^H(\theta,\varphi) &= \frac{1}{\sqrt{2}}\left(e^{-j\beta}E_L^H(\theta,\varphi) - e^{j\beta}E_R^H(\theta,\varphi)\right) \\ &= \sqrt{2}\begin{Bmatrix} \cos BE_E^{Hhe}(\theta,\varphi) - j\sin BE_E^{Hho}(\theta,\varphi) \\ -j\sin BE_E^{Hve}(\theta,\varphi) + \cos BE_E^{Hvo}(\theta,\varphi) \end{Bmatrix} \end{aligned} \tag{3.4}$$

$$\begin{aligned} E_{2\times1,U}^V(\theta,\varphi) &= \frac{1}{\sqrt{2}}\left(e^{-j\beta}E_L^V(\theta,\varphi) + e^{j\beta}E_R^V(\theta,\varphi)\right) \\ &= \sqrt{2}\begin{Bmatrix} -j\sin BE_E^{Vhe}(\theta,\varphi) + \cos BE_E^{Vho}(\theta,\varphi) \\ \cos BE_E^{Vve}(\theta,\varphi) - j\sin BE_E^{Vvo}(\theta,\varphi) \end{Bmatrix} \end{aligned} \tag{3.5}$$

In which $B = \frac{k_0 d_x}{2}\cos(\varphi)\sin(\theta)$ and d_x is the spacing between elements along x-axis and k_0 is the wavenumber. The radiation pattern of lower two elements can be calculated by reversing the B sign in equation (3.4) and (3.5) as follows:

$$E^{H}_{2\times1,L}(\theta,\varphi) = \sqrt{2}\begin{Bmatrix}\cos BE^{Hhe}_{E}(\theta,\varphi) + j\sin BE^{Hho}_{E}(\theta,\varphi)\\ j\sin BE^{Hve}_{E}(\theta,\varphi) + \cos BE^{Hvo}_{E}(\theta,\varphi)\end{Bmatrix} \tag{3.6}$$

$$E^{V}_{2\times1,L}(\theta,\varphi) = \sqrt{2}\begin{Bmatrix}j\sin BE^{Vhe}_{E}(\theta,\varphi) + \cos BE^{Vho}_{E}(\theta,\varphi)\\ \cos BE^{Vve}_{E}(\theta,\varphi) + j\sin BE^{Vvo}_{E}(\theta,\varphi)\end{Bmatrix} \tag{3.7}$$

The radiation pattern of the 2×2-element subarray can be calculated based on the radiation pattern of the two upper and lower elements:

$$E_{2\times2}(\theta,\varphi) = \frac{1}{\sqrt{2}}\left(e^{-jC}E_{2\times1,L}(\theta,\varphi) + e^{jC}E_{2\times1,U}(\theta,\varphi)\right) \tag{3.8}$$

In which $C = \frac{k_0 d_y}{2}\sin(\varphi)\sin(\theta)$ and d_y is the spacing between elements along y-axis. After substituting (3.6) and (3.7) in (3.8) and simplifying the results, the radiation pattern of the 2×2-element array antenna with configuration D in $\varphi = 0^\circ$ and $\varphi = 90^\circ$ planes can be written as:

$$E^{H}_{2\times2,D}(\theta,0) = 2\begin{Bmatrix}\cos BE^{Hhe}_{E}(\theta,0)\\ \cos BE^{Hvo}_{E}(\theta,0)\end{Bmatrix} \tag{3.9}$$

$$E^{V}_{2\times2,D}(\theta,0) = 2\begin{Bmatrix}\cos BE^{Vho}_{E}(\theta,0)\\ \cos BE^{Vve}_{E}(\theta,0)\end{Bmatrix} \tag{3.10}$$

$$E^{H}_{2\times2,D}(\theta,\pi/2) = 2\begin{Bmatrix}\cos CE^{Hhe}_{E}(\theta,\pi/2)\\ \cos CE^{Hvo}_{E}(\theta,\pi/2)\end{Bmatrix} \tag{3.11}$$

$$E^{V}_{2\times2,D}(\theta,\pi/2) = 2\begin{Bmatrix}\cos CE^{Vho}_{E}(\theta,\pi/2)\\ \cos CE^{Vve}_{E}(\theta,\pi/2)\end{Bmatrix} \tag{3.12}$$

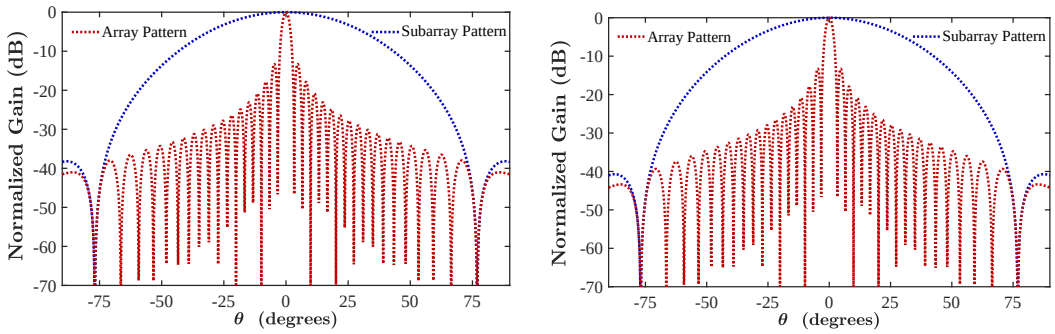

Fig. 3.2: 2×2-element subarray and 2×34-element array radiation pattern calculated using decomposition method in $\varphi = 90°$ plane; (a) H-pol; (b) V-pol.

For a fair comparison, the radiation pattern of a similar probe-fed patch antenna at 2.8 GHz is used for calculating the radiation pattern of 2×2-element subarray array with configuration D.

The radiation pattern of the $N \times M$-element array of subarray can be calculated as follows:

$$E_{2N\times 2M}(\theta,\varphi) = AF_{N\times M}(\theta,\varphi) \times AF_{2\times 2}(\theta,\varphi) \times E(\theta,\varphi) \tag{3.13}$$

In which the $AF_{N\times M}(\theta,\varphi)$ is the array factor of the array of subarrays, $AF_{2\times 2}(\theta,\varphi)$ is the array factor of the 2×2-element array, and $E_{2N\times 2M}(\theta,\varphi)$ is the radiation pattern of the $N \times M$-element array of subarrays.

The radiation patterns of the 2×2-element subarray and the 1×17-element array of the subarray are presented in Fig. 3.2. All the inter-element spacings in this chapter are 55 mm (0.513 λ) unless stated otherwise. As seen in Fig. 3.2, similar to the results presented in [53] there is no sidelobe in the array radiation pattern for both horizontal and vertical polarization in $\varphi = 90°$ plane.

As mentioned before, this method of analysis along with using a single isolated element pattern does not consider the coupling between elements. To verify the accuracy of the radiation patterns calculated using decomposition method, a $1 \times$

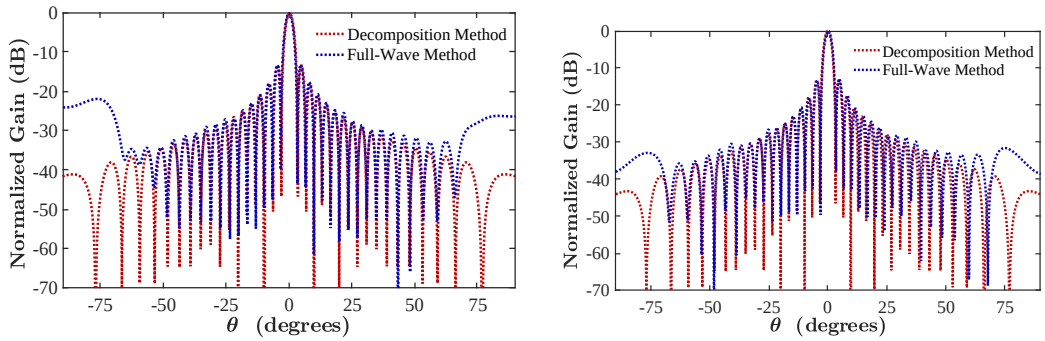

(a) (b)

Fig. 3.3: 2×34-element array radiation pattern calculated using decomposition method and full-wave simulations in $\varphi = 90°$ plane; (a) H-pol; (b) V-pol.

17-element array of a 2×2-element subarray of the probe-fed patch antenna is simulated using HFSS. As shown in Fig. 3.3, a pair of the sidelobes appeared for both polarizations in $\varphi = 90°$ plane. The sidelobe level for horizontal and vertical polarizations is -21 dB and -32 dB, respectively. Clearly, appearance of the undesired sidelobe cannot be predicted by decomposition method. Therefore, the calculated results in [53] and decomposition method, depending on the single element design, may not be generally true. Also, from the measured radiation pattern of the 8×2-element antenna with configuration "D' in [53], it is seen that undesired sidelobes will appear. The sidelobe level in the measured radiation pattern has been related to the small ground plane; however, as it is shown here, the sidelobes exist even if configuration D is implemented in a large 2×32-element array. It should be mentioned that simulation results show that the undesired sidelobes level depends on the single element design. The reason for the appearance of sidelobes will be discussed in the next section.

3.2 Coupling Effect and Method of Calculation

It is seen from the previous section that the calculated radiation pattern of the array of subarray using decomposition method, while the adjacent element coupling effect is neglected, leads to inaccurate results. The coupling associated with elements in the array of identical subarrays is emanating from two facts. The first fact is existence of adjacent elements and the second one is the orientation of the surrounding elements. To investigate the effect of the orientation of the elements on the coupling between elements and final array radiation pattern, first, the embedded element radiation pattern of the array of identical elements is calculated by full-wave simulation. To calculate the embedded element pattern, the radiation pattern of the center element in a 7×7-element array is simulated while all other elements are terminated. In this case, the orientation of the elements is neglected. The radiation pattern of the 2×2-element pattern with configuration D is then calculated by decomposition method. Using (3.12), the radiation pattern of the 2×34-element array is calculated. As seen in Fig. 3.4 including the coupling between elements, changes the 2×34-element pattern but cannot predict the side lobes.

To characterize the effects of element orientation on the subarray radiation pattern, the 2×2-element subarrays with different configurations are simulated using HFSS. Fig. 3.5 (a) and Fig. 3.5 (b), show H-pol and V-pol copolarization (Co-Pol), and Cross-polarization (X-Pol) radiation pattern of the isolated 2×2-element array of a probe-fed patch antenna with configuration (CFG) A , C, and D, respectively. The element spacing (d) in these simulations is 55 mm (0.513 λ). In $\varphi = 0^\circ$ and $\varphi = 90^\circ$ planes, using image configuration, especially configuration C, will significantly improve the cross-polarization level of the 2×2-element array. Also, not shown here, in the $\varphi = 45^\circ$ plane, image configuration has improved

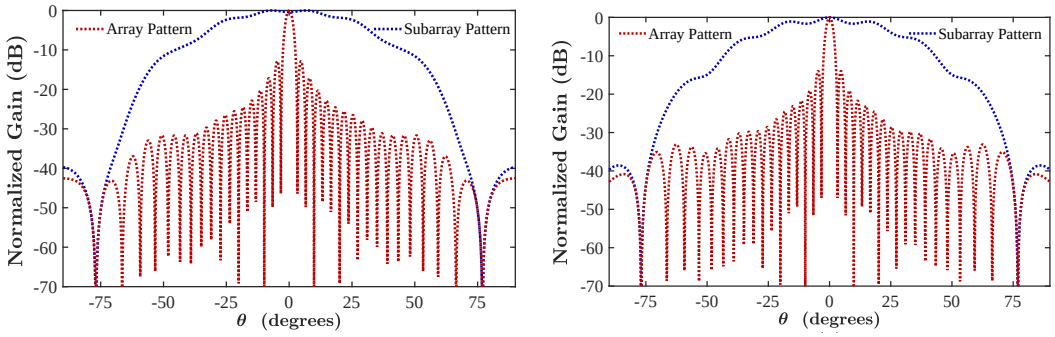

(a) (b)

Fig. 3.4: 2×2-element subarray and 2×34-element array radiation pattern calculated using decomposition method and identical array embedded element pattern; (a) H-pol; (b) V-pol.

the cross-polarization level in the main beam area. As shown in Fig. 3.5 the copolarization radiation patterns in all three arrays are almost laid on each other, and there is no degradation in a copolarization radiation pattern of 2×2-element array compared to the radiation pattern of the array with configuration A.

Clearly, applying the array factor of an array of the subarrays will result in similar copolarization patterns for all three configurations. In other words, any calculated radiation pattern of larger arrays based on the isolated 2×2-element subarray pattern is not accurate enough for the precise prediction of the undesired sidelobes level.

For further explanation, the array factor of a large array (2×34-element array) of the probe-fed patch antenna is calculated by different methods. The array factor of the $2N \times 2M$-element array is the combination of the array factor of the 2×2-element array and $N \times M$-element array antenna which is shown in Fig. 3.6. As is shown in Fig. 3.6, the grating lobe of $N \times M$-element array antenna (with an inter-element spacing of 110 mm; 1.026 λ) appears in $\theta = 77°$. On the other hand, the first null of the array factor 2×2-element array (with an inter-element spacing of 55 mm; 0.513 λ) is precisely at the location of the grating lobe of

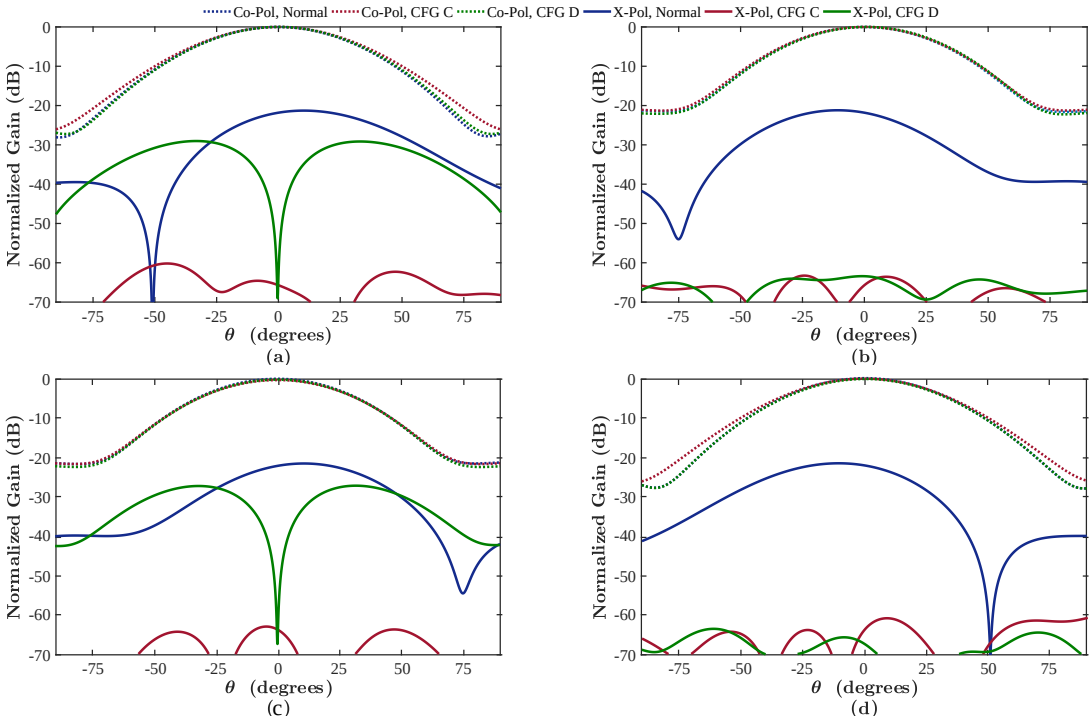

Fig. 3.5: Simulated radiation pattern of the 2×2-element array of probe-fed patch antenna configured according to the configuration A, C, and D; (a) H-pol, $\varphi = 0°$ plane; (b) H-pol, $\varphi = 90°$ plane; (c) V-pol, $\varphi = 0°$ plane; (d) V-pol, $\varphi = 90°$ plane.

$N \times M$-element array. Consequently, based on equation (3.13), the effect of the peak of the array factor of $N \times M$-element array in total array radiation pattern will be eliminated with the null of the array factor 2×2-element array. As shown in Fig. 3.6, there is no grating lobe or undesired side lobe in the array factor of the $2N \times 2M$-element array.

The radiation pattern of a 2×34-element array of the probe-fed patch antenna with configuration A is calculated using two different methods. In the first method, the array factor of the 2×2-element array is applied on the isolated element pattern to calculate the radiation pattern of the 2×2-element array antenna. The array factor of the 1×17-element array antenna is then applied on the calculated 2×2-element array radiation pattern to calculate the

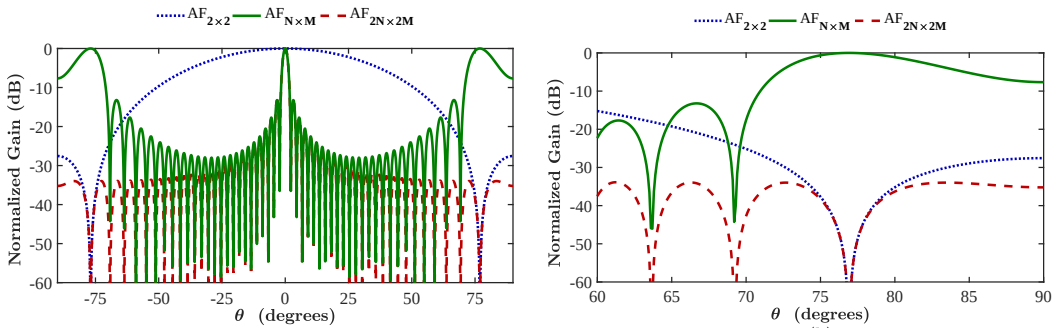

Fig. 3.6: (a) Array factor of the $2N \times 2M$-element array. (b) Local grating lobe location of $N \times M$-element array.

2×34-element array radiation pattern. In the second method, the 2×2-element array radiation pattern is calculated using the full-wave simulations, and then the array factor of the 1×17-element array antenna is applied. As shown in Fig. 3.7 and Fig. 3.8 (a), the radiation pattern of the 2×2-element array antenna calculated with the two methods are similar in the main beam area. It can be seen that the sharp null of the array factor of the 2×2-element array exists in the radiation patterns calculated based on the first method, however, in the full wave results, there is no null. The importance of the null in 2×2-element array radiation pattern is described in Fig. 3.6 as it eliminates the grating lobe peak of the array factor of $N \times M$-element array (spacing = 2d). When the null is removed from 2×2-element array radiation pattern the effect of the grating lobe of the $N \times M$-element array will show up in the $2N \times 2M$-element array radiation pattern.

Fig. 3.7 (b) and Fig. 3.8 (b) show the radiation pattern of the 2×34-element array. As shown in Fig. 3.7 (b), the effect of the grating lobe of the array factor of the 1×17-element array antenna appears in the results calculated with method 2. The 2×2-element array radiation pattern and the final array radiation pattern

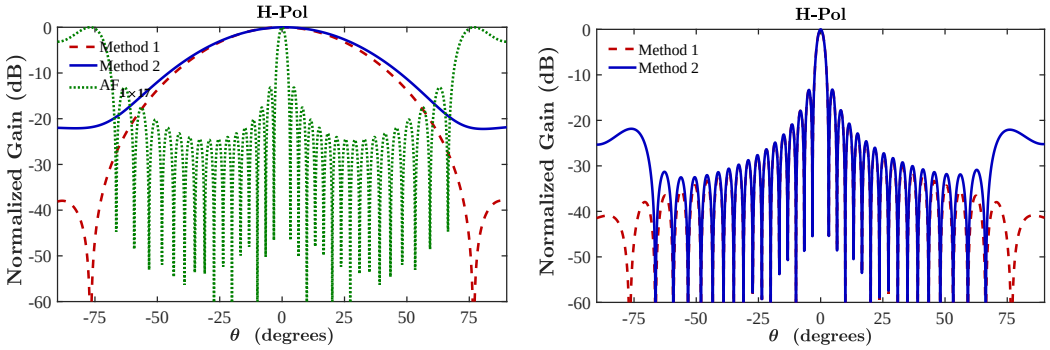

Fig. 3.7: Comparison of the horizontal polarization radiation pattern of a 2×34-element array with normal configuration calculated with two methods. (a) 2×2-element array pattern; (b) 2×34-element array radiation pattern.

for the vertical polarization are shown in Fig. 3.8. As shown in Fig. 3.8 (a), for the vertical polarization, compared to the horizontal polarization, the full wave results of the 2×2-element array radiation pattern is closer to the results calculated with applying the array factor 2×2-element array. Consequently, the side lobes with the lower peak are expected. Fig. 3.8 (b) shows the vertical polarization radiation pattern of the 2×34-element array. As shown in Fig. 3.8 (b), the local grating lobe still exists but with reduced peak power compared to horizontal polarization results. Comparing the two calculated radiation patterns shows that using isolated 2×2-element array pattern leads to inaccurate results. This means that the coupling caused by existence of the adjacent elements and the effect of elements orientation cannot be separated.

3.3 Embedded Subarray Pattern and Limitations of Image Configuration

Full-wave simulations can be used for predicting the radiation pattern of small array antennas. However, for large array antennas, alternative solutions should

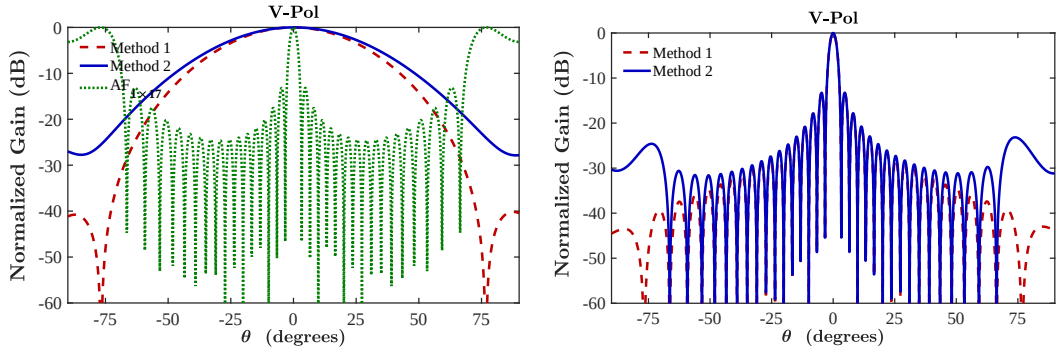

Fig. 3.8: Comparison of the vertical polarization radiation pattern of a 2×34-element array with normal configuration calculated with two methods. (a) 2×2-element array pattern; (b) 2×34-element array radiation pattern.

be utilized. The embedded element pattern is the radiation pattern of the central element in an array while all other elements are terminated. The embedded subarray pattern could be defined as the radiation pattern of the central subarray in the array of the subarrays, while all the other subarrays are terminated. The radiation pattern of the embedded 2×2-element subarrays is studied in this section. To calculate the embedded subarray pattern, a 3×3-element array of the 2×2-element subarrays is simulated. As shown in Fig. 3.9 (a), the embedded subarray pattern compared to the ideal 2×2-element pattern, which is calculated by applying the array factor of the 2×2-element array to the single element pattern, is missing two symmetric nulls. The effect of these symmetric Nulls on the array radiation pattern was discussed in the Fig. 3.6. Consequently, as seen in Fig. 3.9 (b), the undesired sidelobes appear in the calculated radiation pattern of the 2×34-element array. Compared to full-wave simulation result which does not have the sidelobes issue, it can be concluded that the calculated embedded subarray pattern of the 6×6-element array is not accurate enough for predicting the large array radiation pattern.

The reason for discrepancy between the two radiation patterns is illustrated

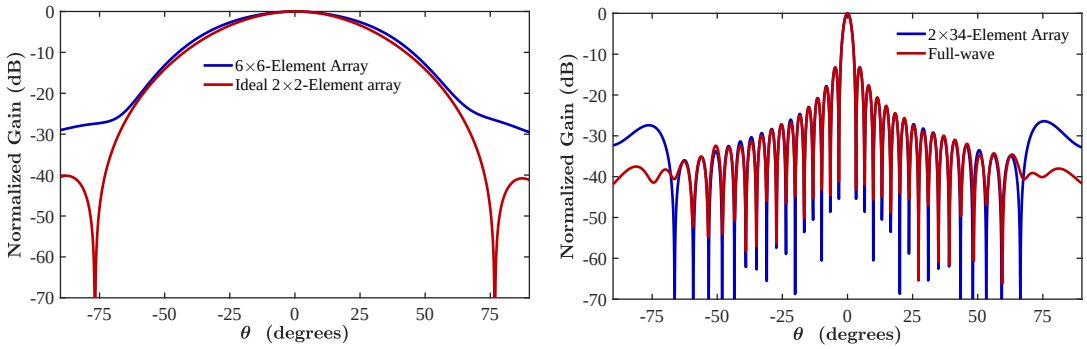

(a) (b)

Fig. 3.9: Simulated radiation pattern of the 2×2-element subarray of a probe-fed patch antenna with configuration A; (a) embedded 2×2-element pattern, (b) 2×34-element array pattern.

in Fig. 3.10. As shown in Fig. 3.10 (a), the embedded subarray radiation pattern is highly sensitive to the size of the array antenna that is used for calculating the subarray radiation pattern. Based on the simulation results in Fig. 3.10 (a), as the size of the array increases, the sharper nulls appear in the 2×2-element subarray array radiation pattern. The null in the embedded subarray radiation pattern appears if the two adjacent elements radiation patterns have the same amplitude and be 180° out of phase at a certain location. If the number of the element on the right side and left side of each element in the 2×2-element subarray is different, the conditions for having a perfect null are not met. As the number of elements increases the ratio of the number of the element on the right side to left side becomes closer to one and subsequently, the depth of the null gets closer to the ideal 2×2-element array pattern. Fig. 3.10 (b), shows the radiation pattern of the 2×34-element array, calculated based on different embedded subarray patterns. As it was expected from embedded subarray patterns, the calculated 2×34-element array sidelobe level gets closer to the full wave results. The number of array elements for less than 2 dB difference between full-wave and simulation

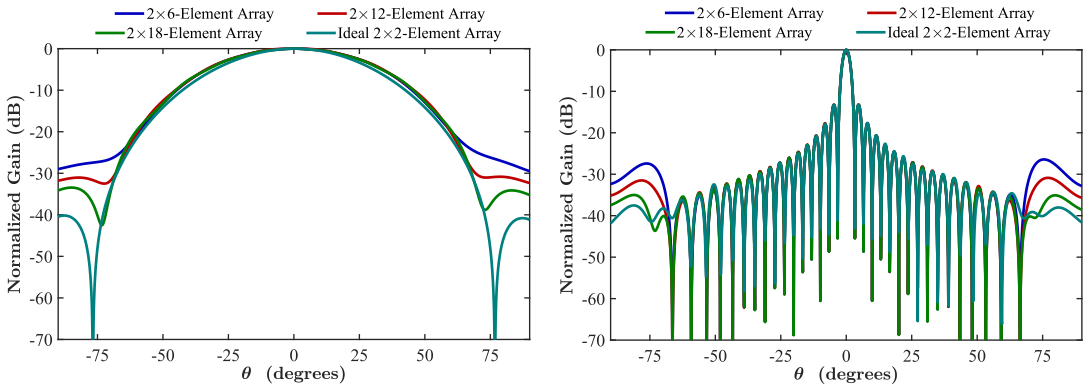

Fig. 3.10: Simulated radiation pattern of the 2×2-element subarray of a probe-fed patch antenna with configuration A; (a) embedded 2×2-element patterns of arrays with different number of subarrays, (b) 2×34-element array patterns.

results, using this probe-fed patch antenna, is 18.

3.4 Approaches to Design High-Performance Array Antennas

The radiation pattern of the 2×34-element array of a probe-fed patch antenna with configuration C and D is calculated by using the embedded subarray patterns and full wave method. As shown in Fig. 3.11 and Fig. 3.12, the embedded subarray pattern of the 18-element array perfectly predicts the side lobe level issue in configuration "D." This means that on the contrary to the claim in [53], the side lobe issue cannot be solved using configuration "D."

configuration C and D will significantly improve the cross-polarization level of the array of the probe-fed patch antenna. However, for a dual-polarized phased array antenna, it is always desired to use a high-performance single element which provides high input-isolation between horizontal and vertical polarizations. High-performance dual-polarized hybrid feed antennas [11], [12],

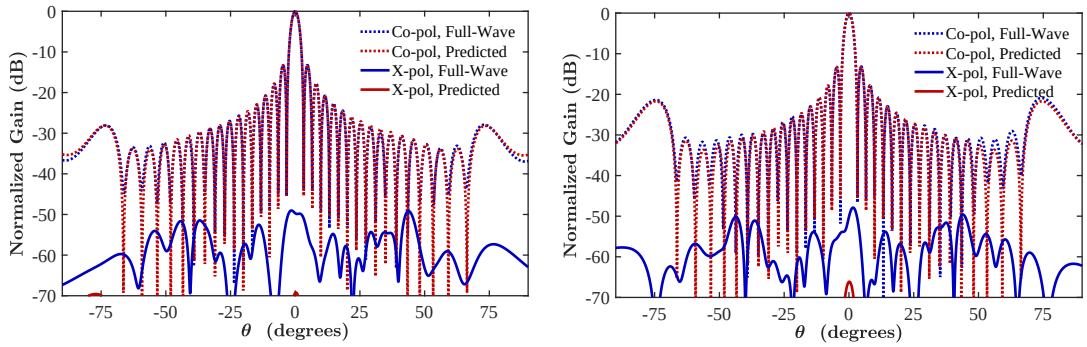

Fig. 3.11: Predicted and full-wave simulated radiation pattern of 2×34-element array of a probe-fed patch antenna with configuration C; (a) H-pol, (b) V-pol.

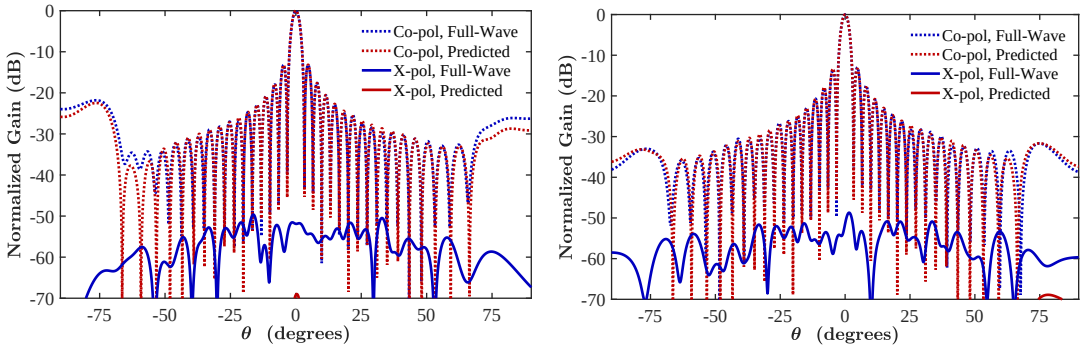

Fig. 3.12: Predicted and full-wave simulated radation pattern of 2×34-element array of a probe-fed patch antenna with configuration D; (a) H-pol, (b) V-pol.

[55] could be an ideal choice for multifunction applications [56]. Therefore, in this section, a high-performance hybrid feed patch antenna is used as the unit cell for designing a large array antenna.

It is worth noting that the side lobe level associated with each configuration also depends on the geometry of the unit cell. As the element becomes more geometrically symmetric, it will have a more symmetrical radiation pattern. In other words, as the radiation pattern of the element becomes more symmetric the effect of mirroring the elements on its radiation pattern becomes less visible.

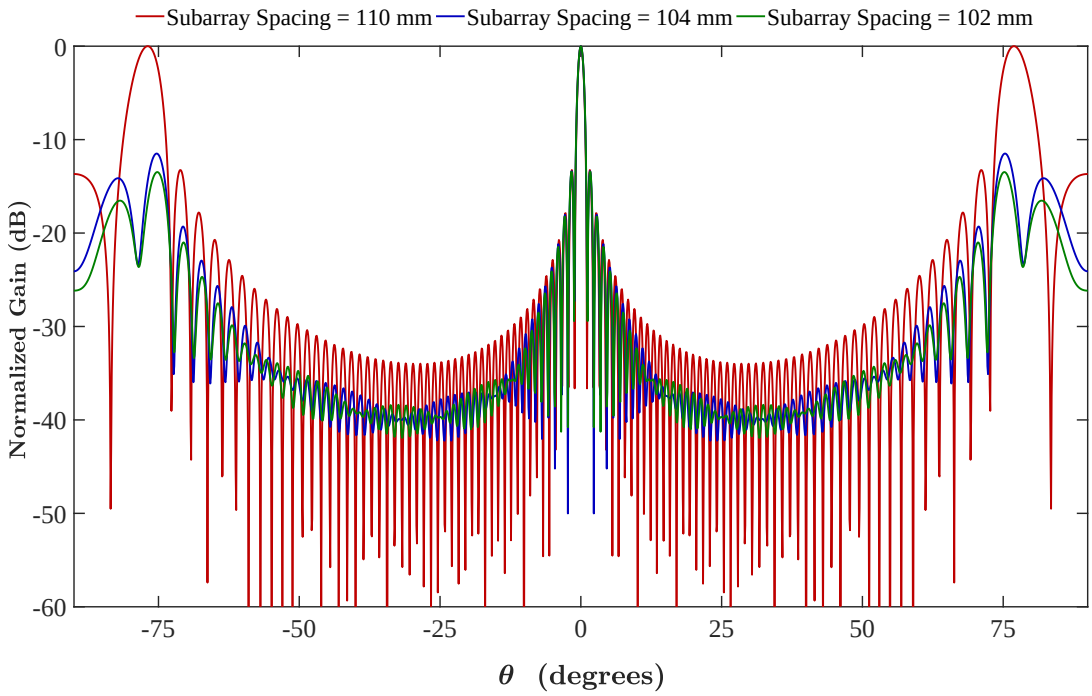

Fig. 3.13: Array factor of an array of identical subarrays with different element spacings.

An alternative solution for reducing the sidelobe level of the array is decreasing the peak power of the grating lobe of the array of subarrays. The array factors of the array of identical subarrays with different element spacings are shown in Fig. 3.13. As shown in Fig. 3.13, decreasing the spacing between elements will reduce the peak level of the grating lobe of the identical subarrays. Reducing the subarray spacing from 110 mm (1.026 λ) to 104 mm (0.97 λ) and 102 mm (0.952 λ) will reduce the level of the undesired grating lobes of the array factor of the subarrays to -11 dB and -14 dB, respectively.

For Multifunction Phased Array Radar (MPAR) application, the size of the array antenna could be as large as WSR-88D radar. WSR-88D is utilizing an 8.85 m reflector antenna [24]. Considering the Cylindrical Polarimetric Phased Array Radar (CPPAR) and 55 mm (0.513 λ) spacing between elements, this will

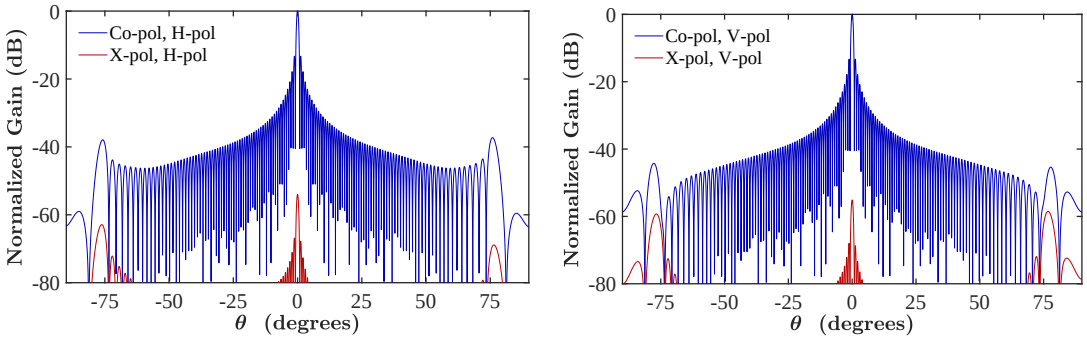

(a) (b)

Fig. 3.14: Co and cross-polarization radiation pattern of the 2×130-element array of the designed single element with configuration C at broadside (subarray spacing = 110 mm). (a) Horizontal polarization; (b) Vertical polarization.

lead to a large cylindrical array antenna with approximately more than 130 elements along its axis. For weather application, it is essential for an array antenna to have a symmetrical copolarization and low cross-polarization level radiation pattern. Also achieving the low sidelobe levels in the final array radiation pattern is critical. To achieve a symmetrical radiation pattern with low cross-polarization level, configuration C is an interesting choice because of its symmetrical subarray geometry. According to the aforementioned information and results, the following procedure is being proposed for designing a large phased array antenna and an accurate prediction of the sidelobe level or reducing it to the minimum possible level:

1. Designing a single element with maximum possible geometrical and electrical symmetry.

2. Choosing the subarray configuration; configuration C provides more geometrical symmetry, however, configuration D has lower sidelobe level.

3. Extracting the embedded subarray radiation pattern by simulation a large (15 elements or more) linear array of the selected subarray.

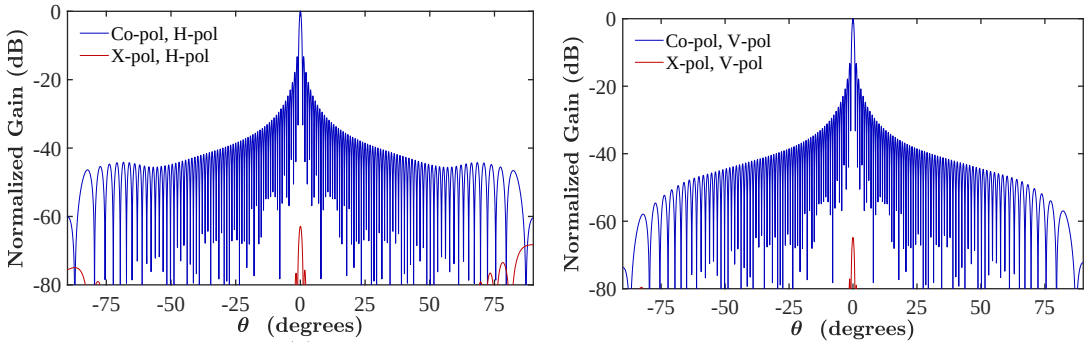

(a) (b)

Fig. 3.15: Co and cross-polarization radiation pattern of the 2×136-element array of the designed single element with configuration C at broadside (subarray spacing = 104 mm). (a) Horizontal polarization; (b) Vertical polarization.

4. Calculating the large array radiation pattern using the simulated embedded subarray pattern.

5. Evaluating the sidelobe level of the large array.

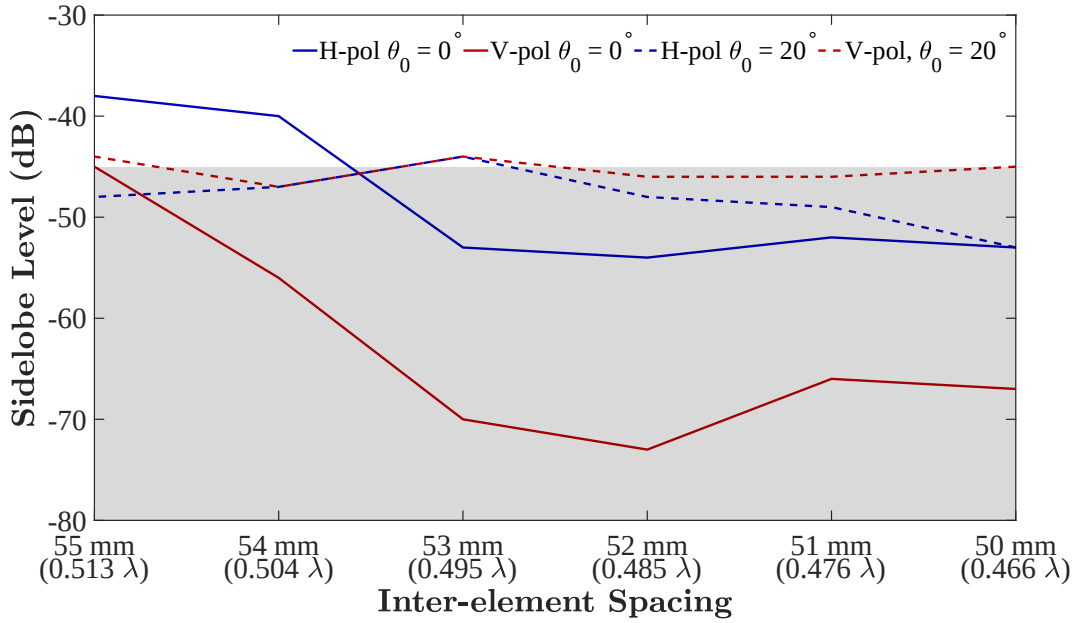

Fig. 3.16: Sidelobe level versus subarray spacing for an array of hybrid-fed patch antenna configured according to the configuration "C."

6. If the sidelobe level is not as low as the desired level the symmetry of the single element needs to be increased or, the spacing between elements should be decreased.

Following the above procedure, the embedded subarray radiation pattern is calculated from simulation of the 2×34-element array with configuration C and 55 mm (0.513 λ) inter-element spacing. The radiation pattern of the 2×130-antenna is then calculated based on the simulated embedded subarray pattern. As shown in Fig. 3.14, in a 2×130-element array antenna with 55 mm (0.513 λ) spacing between elements, and uniform excitation, the level of the undesired local grating lobe is -37 dB. Assuming that the preferred level is -45 dB, the undesired grating lobe level needs to be reduced.

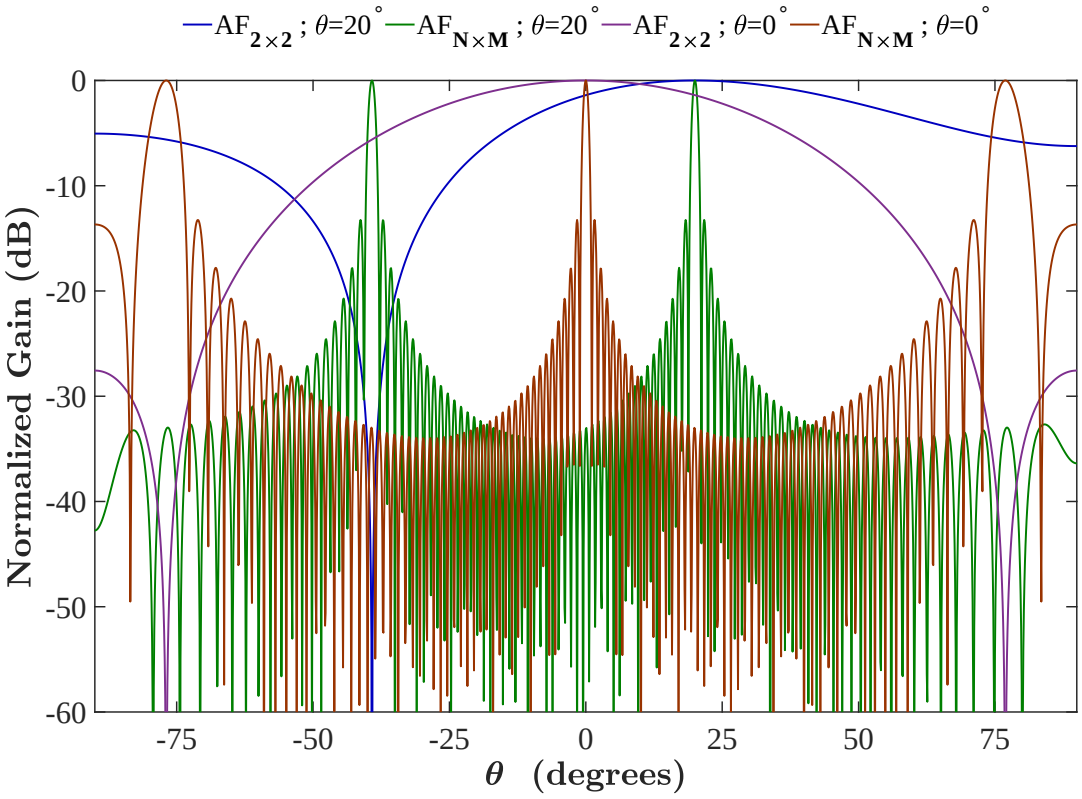

Fig. 3.17: Array factor of an array of identical subarrays at different scan angles.

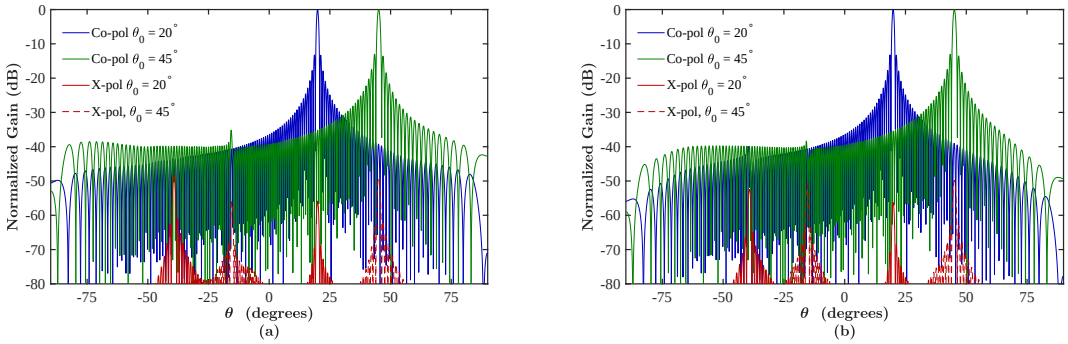

Fig. 3.18: Co and cross-polarization radiation pattern of the 2×130-element array of the designed single element with configuration C at broadside (subarray spacing = 110 mm). (a) Horizontal polarization; (b) Vertical polarization.

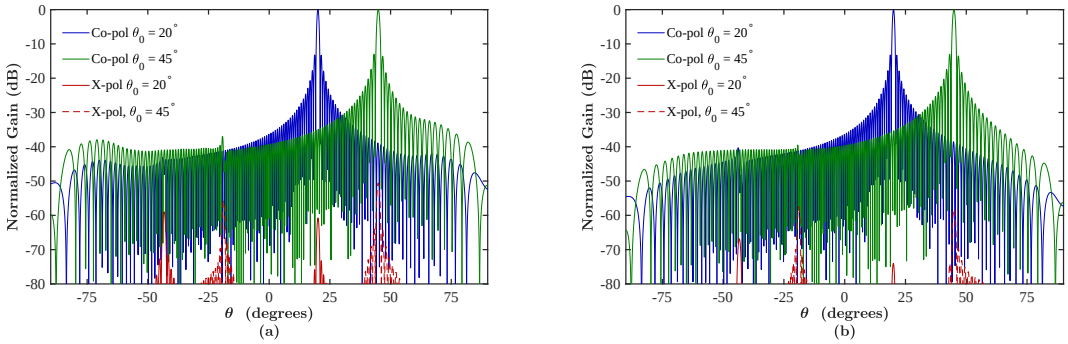

Fig. 3.19: Co and cross-polarization radiation pattern of the 2×136-element array of the designed single element with configuration C at broadside (subarray spacing = 104 mm). (a) Horizontal polarization; (b) Vertical polarization.

The radiation pattern of the 2×130-element and 2×136-element array of hybrid feed patch antenna with configuration "C," for different element spacing, are shown in Fig. 3.14 and Fig. 3.15. As shown in Fig. 3.15 (a), for horizontal polarization with 104 mm (0.97 λ) subarray spacing, the undesired sidelobe peak is reduced to -47 dB. For vertical polarization as shown in Fig. 3.15 (b), with 104 mm (0.97 λ) spacing between subarrays, there is almost no sign of undesired sidelobes. As shown in Fig. 3.15, the advantage of decreasing the spacing between the elements is in reducing the peak level of the undesired local grating lobes. However, reducing the spacing between elements will increase the

coupling between elements which may result in distortion of the radiation pattern of the phased array antenna especially when the beam is steered to off-broadside directions. The other disadvantage of decreasing the spacing between the elements is increasing the number of required elements which will result in higher cost of fabrication.

Fig. 3.16 shows the minimum sidelobe level of the array of the 2×2-element subarray of hybrid-fed patch antenna versus element spacing. The minimum side lobe level is calculated by applying the array factor of a very large array antenna to the simulated embedded subarray radiation pattern. Increasing the array antenna dimensions will increase the gain at the beam pointing angle. However, it decreases the normalized gain (concerning maximum array gain) at the location of the grating lobes. At some point, by increasing the antenna dimensions, the undesired side lobes level will not decrease any more. The pattern synthesis and optimization methods can be used to improve the side lobe level at other angles and predicting the undesired sidelobes level using smaller arrays. However, these methods are not able to solve the undesired sidelobe problem since the unwanted sidelobes are in fact the grating lobes of the array factor of subarrays. As shown in Fig. 3.16, the lowest sidelobe level for both polarizations, while the array antenna is radiating at broadside, is achieved at 52 mm (0.485 λ) interelement spacing.

At the 20° scan angle, the sidelobe level of the antenna pattern, especially for vertical polarizations, is not significantly changed, as the spacing between elements is decreased. Also for horizontal polarization, with 55 mm (0.513 λ) spacing between elements, at $\theta_0 = 20°$ the side lobe level is 10 dB lower compared to the broadside radiation pattern. The reason for having lower sidelobe level at the $\theta_0 = 20°$ scan angle, is that the grating lobe of the array of subarrays,

is exactly collocated with the null of the steered embedded subarray radiation pattern. Also, as shown in Fig. 3.17, the beam width of the grating lobe of the $N \times M$-element array factor, when the beam pointing angle is steered to $\theta_0 = 20°$, is narrower compared to the grating lobe of the $N \times M$-element array factor at broadside. Although this still limits the performance of the antenna, the effect of the grating lobes of the subarrays become less visible as the scan angle increases.

To study the effect of reducing the array element spacing, the radiation pattern of the array at the maximum required steering angle for MPAR application which is 20° ($\theta_0 = 20°$) in the elevation direction and in an arbitrary scan angle ($\theta_0 = 45°$) are shown in Fig. 3.19. The horizontal polarization and vertical polarization radiation pattern of the array antenna are shown in Fig. 3.19(a) and Fig. 3.19 (b), respectively.

In the non-configured antenna arrays, with the beam steering, the side lobe level increases. In the presented configured antenna arrays, the antenna radiation pattern is compared with the case that the spacing between elements is 55 mm (0.513 λ). Fig. 3.18 (a-b) shows the array radiation pattern at two scanning angles, while the subarray spacing is 110 mm (1.026 λ), and Fig. 3.19 shows the array radiation pattern when the subarray spacing is reduced to 102 mm (0.97 λ). Comparing two sets of radiation patterns reveals no degradation in antenna radiation pattern and the side lobe level is lower than -40 dB while the array element spacing is reduced to 52 mm (0.485 λ).

Therefore, in this design, the optimal spacing between array elements with configuration C for CPPAR in MPAR application would be 52 mm (0.485 λ).

The performance of the configuration D can be improved by extending the 2×2-element subarray to 4×4-element subarray. Fig. 3.20 shows the configuration E which is evolved from applying the configuration D to 2×2-element group level

and considering the azimuth plane as the plane of symmetry.

To evaluate the performance of this configuration, we are using the method presented in this dissertation. To do so, a 1×4-element array of the 4×4-element subarray configured based on the configuration E is simulated using ASYSY HFSS. To compare the results, with the previously calculated radiation patterns of configured arrays according to the configurations C and D, the embedded radiation pattern of the 4×4-element subarray is used for

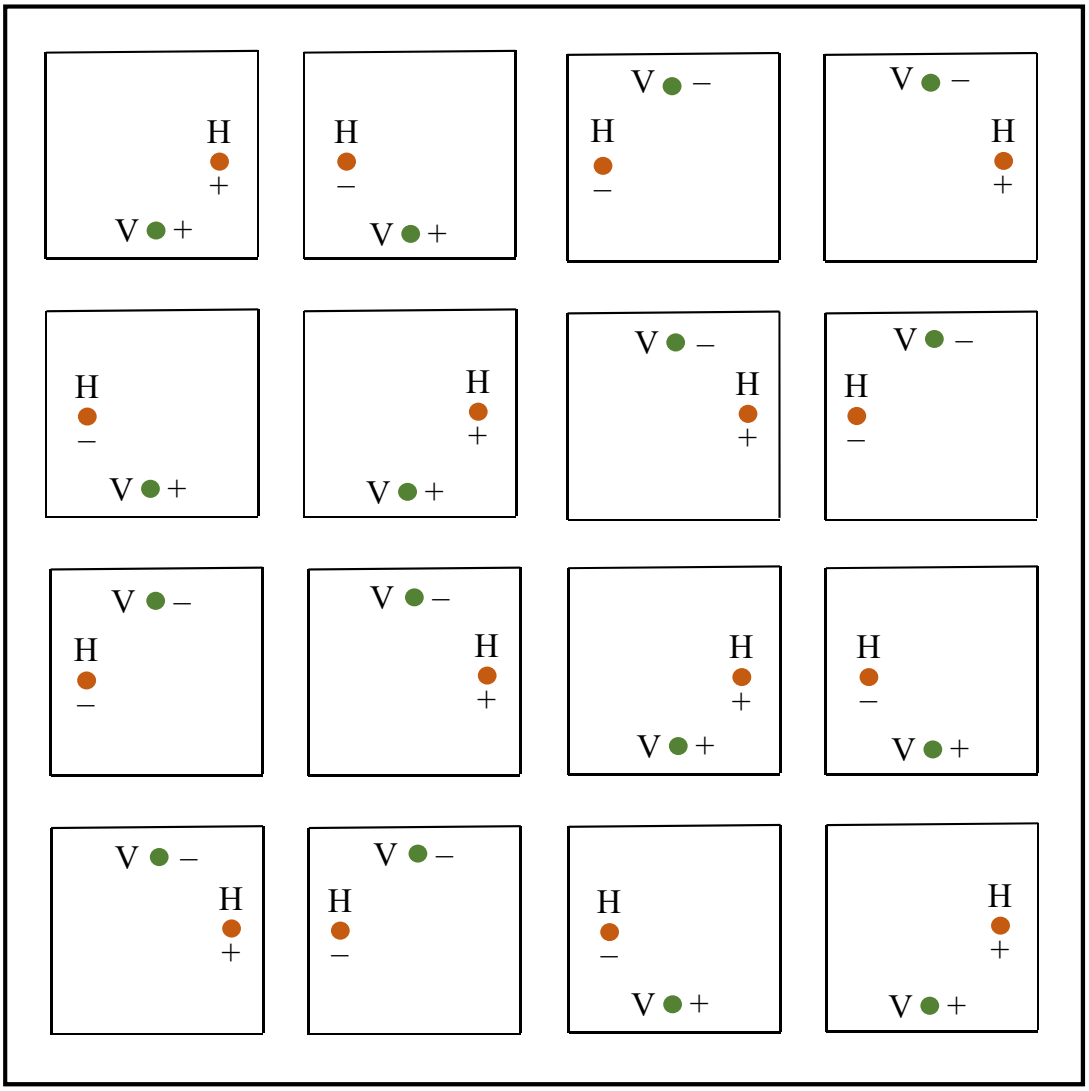

Fig. 3.20: 4×4-element subarray configured according to the configuration E [53].

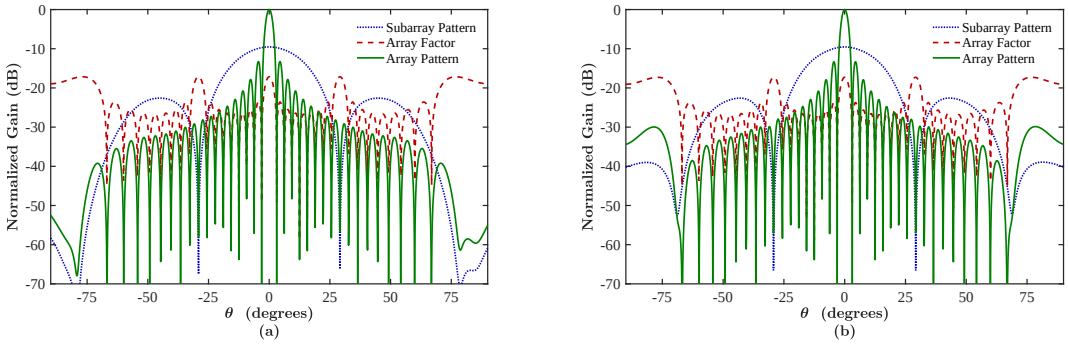

Fig. 3.21: Co and cross-polarization radiation pattern of the 4×32-element array of probe-fed patch antenna with configuration E at broadside (subarray spacing = 220 mm; 2.052 λ). (a) Horizontal polarization; (b) Vertical polarization.

calculating the radiation pattern of a 4×32-element array antenna.

Fig. 3.21 shows the embedded subarray radiation pattern, the array factor of the 1×8-element array of the 4×4-element subarray, and the calculated 4×32-element array antenna radiation pattern. It can be seen that by using configuration E the radiation performance of the horizontal polarization has been significantly improved, however, the undesired sidelobes with the intensity of -30 dB appear in the vertical polarization radiation pattern.

As shown in Fig .3.21, extending the subarray spacing to 220 mm (2.052 λ), creates four grating lobes. The first set of grating lobes with current subarray spacing appears at $\theta = 29°$. It can be seen that the first set of grating lobes have a narrower beamwidth compared to the second grating lobe set. Also since the first grating lobes are precisely co-located with first sets of null in the embedded 4×4-element subarray pattern, with this particular element design, no grating lobes will appear in the array radiation pattern. Although using configuration E improves the sidelobe levels, however, in many applications, a linear array antenna is required or extending the dimension of the subarray is not applicable. For instance, in polarimetric multifaceted phased array antennas, having four

columns in one facet results in an off-principal plane beam steering. Off-principle plane beam steering increases the cross-polarization level and decreases the radiation pattern symmetry, which could increase the polarimetric biases. Therefore, extending the subarrays dimensions should be avoided.

In this chapter, the radiation characteristics of a dual-linear polarization array of 2 × 2-element and 4 × 4-element subarrays are studied. Cross-polarization suppression can be realized through the image feed method; however, this method will result in undesired sidelobes in the array radiation pattern. To characterize the radiation pattern of large arrays, it is shown that the calculated radiation pattern of the 2 × 2-element subarray, based on even and odd components of isolated or embedded element pattern, will result in the inaccurate radiation pattern. Configuration "C" presents the best suppression of the cross-polarization level. However, the undesired local grating lobe level in large array antennas with configuration "C" is higher compared to arrays configured according to configuration "D." On the other hand; configuration "C" provides a more geometrical symmetry which will result in the more symmetric radiation pattern. On the contrary to previously published papers, it is shown that using configuration "D" will not totally suppress the undesired sidelobes. Also, it is demonstrated that under certain conditions the embedded subarray pattern can be used to characterize the radiation pattern of the large array of identical subarrays. To calculate the embedded subarray pattern, the ratio of the number of subarrays on the left and right side of the excited subarrays should be close to one.

Using full-wave simulation result, it is shown that the undesired lobes in an array of the identical 2 × 2-element subarrays copolarization pattern, which was previously considered as side lobes, can be identified as the local grating lobes

of the subarrays. This claim is proved by decreasing the spacing between array elements that reduced the peak level of the undesired lobes in the array factor of the identical subarrays. Finally, a procedure for characterizing the radiation pattern of a large array antenna with identical subarrays is proposed. Based on the procedure, increasing the geometrical and electrical symmetry of the designed unit cell and decreasing the array inter-element element spacing are suggested for mitigating the sidelobe level

Chapter 4

Planar Array of Hybrid-Fed Microstrip Patch Antenna

The performance of the designed single elements in chapter 2 are characterized while these designs are implemented in an array. To improve the cross-polarization isolation, a 2 × 2-element subarray of the proposed single elements are designed, fabricated and tested. To characterize the radiation pattern of the designed subarrays, the planar arrays of the presented subarrays, are fabricated, and the radiation pattern of the antenna arrays at broadside and various scan angles are provided and discussed.

4.1 Asymmetric Non-Overlapping Aperture Coupled Patch Antenna Array

In this section, a low cross-polarization, high-isolation dual-polarized aperture coupled microstrip patch antenna array is designed for MPAR application. In this design, 2 × 2-element subarrays with image configuration are implemented. In image configuration method the array elements are arranged in an array of 2×2-element subarrays and the final 12 × 12-element array consists of a 6 × 6-element array of 2 × 2-element subarrays.

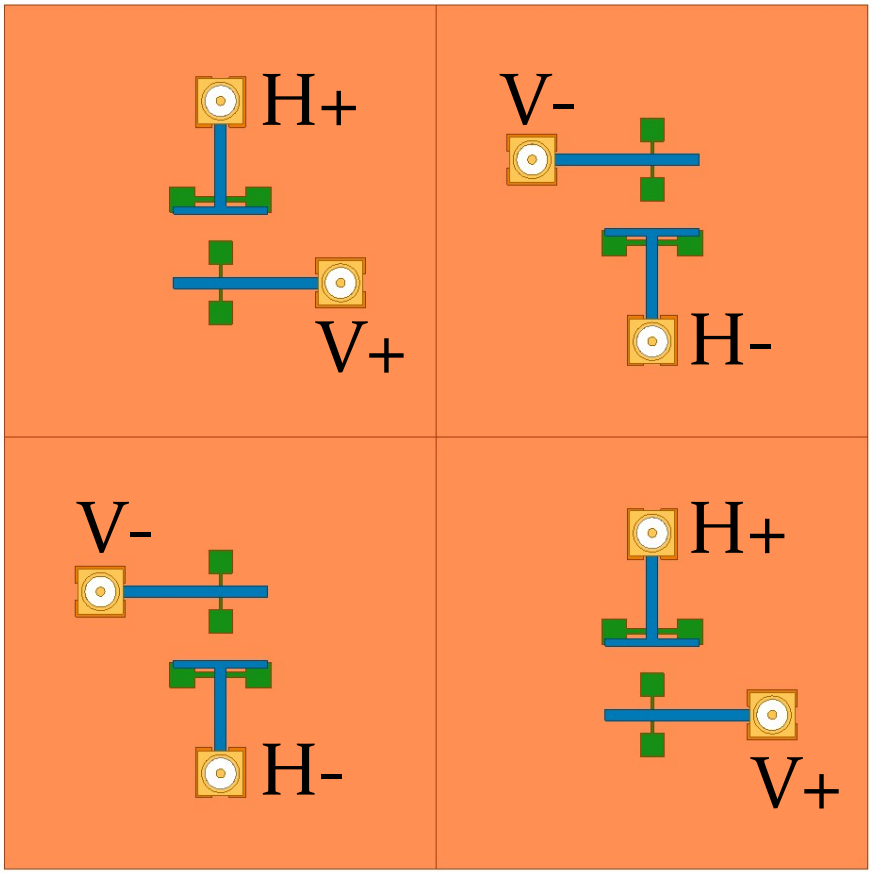

Fig. 4.1: 2 × 2-element subarray configuration.

4.1.1 Subarray Antenna Design

In order to achieve a low level of cross-polarization, the elements in the array can be arranged to the groups of 2 × 2-element subarrays with image configuration [53]-[54] to cancel cross-polarization. The feeding network distributes power to single elements in the array and the radiation pattern of each element is determined by its location, orientation and the phase of excitation. In this design, the array is considered as a number of identical 2 × 2-element subarrays as is shown in Fig. 4.1. In this configuration, the ports marked ”-” are 180°out of phase with respect to the ports marked ”+”. This configuration will not affect the copolarization radiation pattern, however, it will suppress the

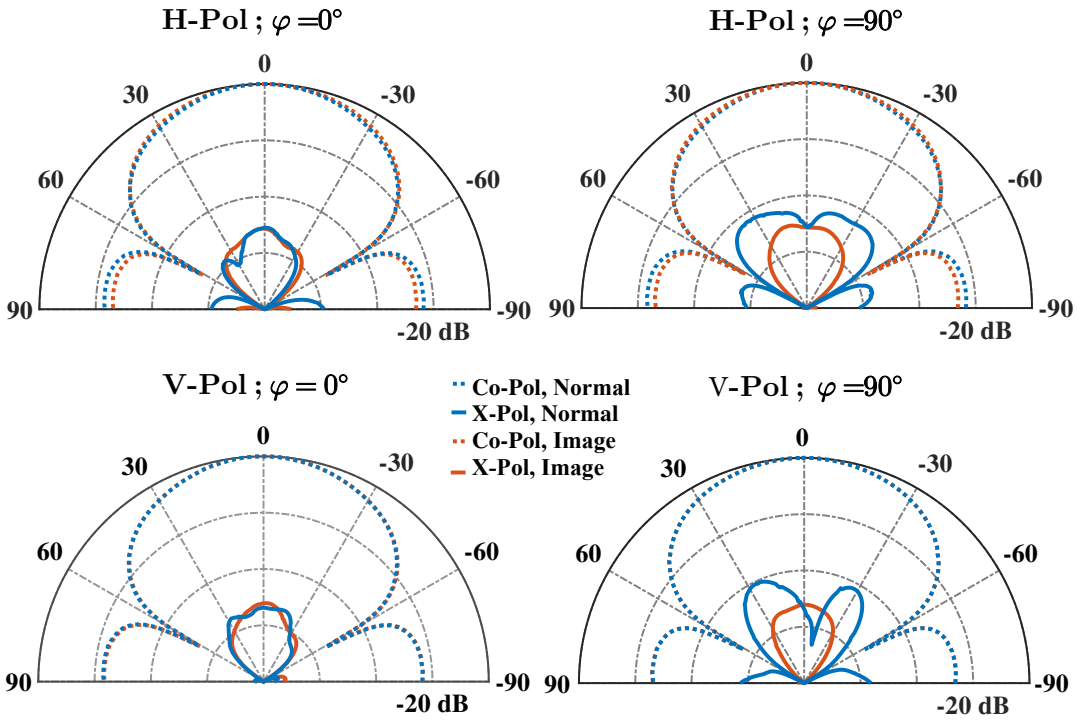

Fig. 4.2: Simulated 2 × 2-element subarray radiation pattern with and without image configuration.

cross-polarization radiation pattern especially in probe-fed patch antenna.

In order to characterize the performance of this configuration, the radiation pattern of the 2×2-element subarray with normal configuration when the elements are placed beside each other without any rotation and 2 × 2-element subarray with the image configuration, as shown in Fig. 4.1, are compared. In these simulations, a 3 × 3-element array of 2 × 2-element subarrays is simulated and the radiation patterns of the center 2 × 2 -element subarrays in two configurations are compared in Fig. 4.2.

Comparing the radiation pattern of 2 × 2-element subarray confirms that in the $\varphi = 90°$ plane for both polarizations the cross-polarization level has been significantly improved. The cross-polarization level at 35° scan angle for horizontal polarization is improved from -46 dB to -57 dB and for vertical polarization is

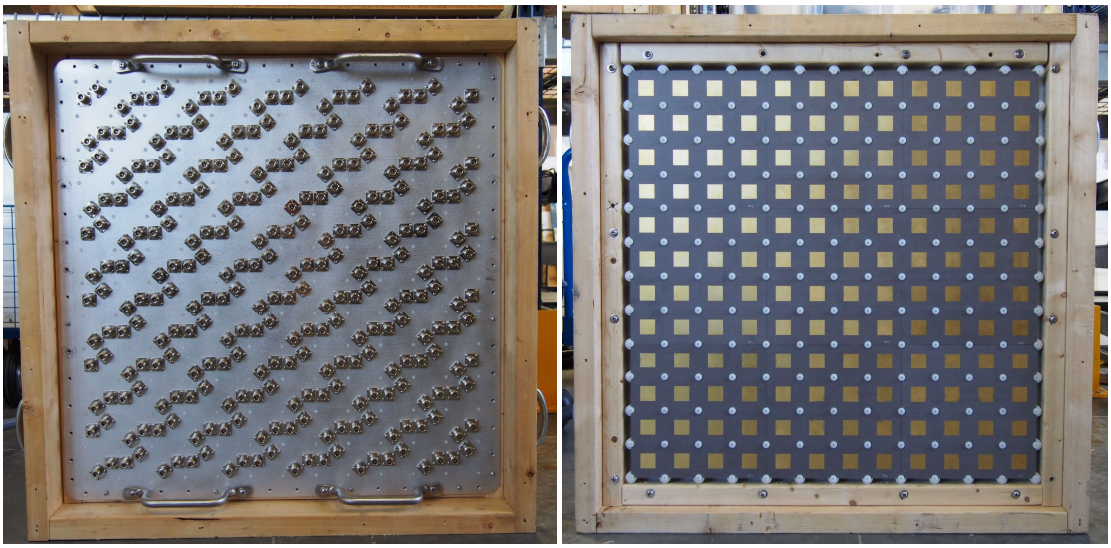

Fig. 4.3: Fabricated 12 × 12-element array antenna. (a) Back view; (b) Front view.

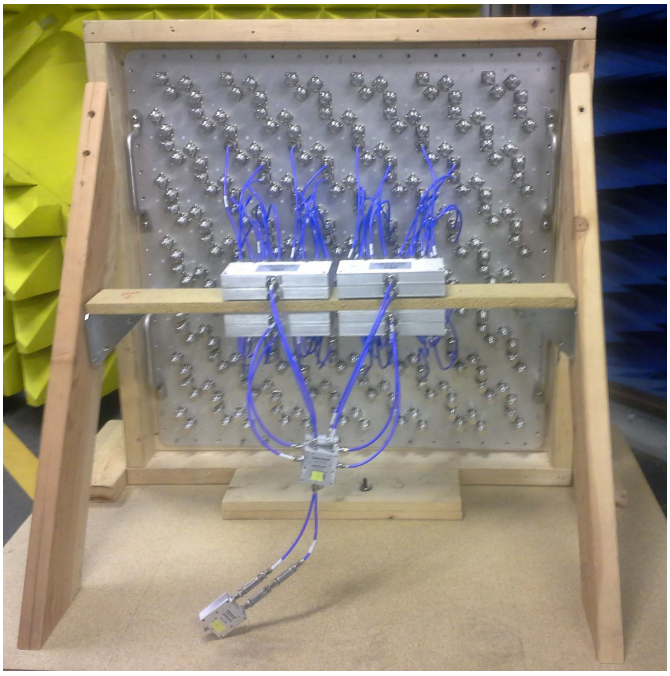

Fig. 4.4: Fabricated 12 × 12-element array antenna. The center 8 × 8-element array is excited and other elements are terminated.

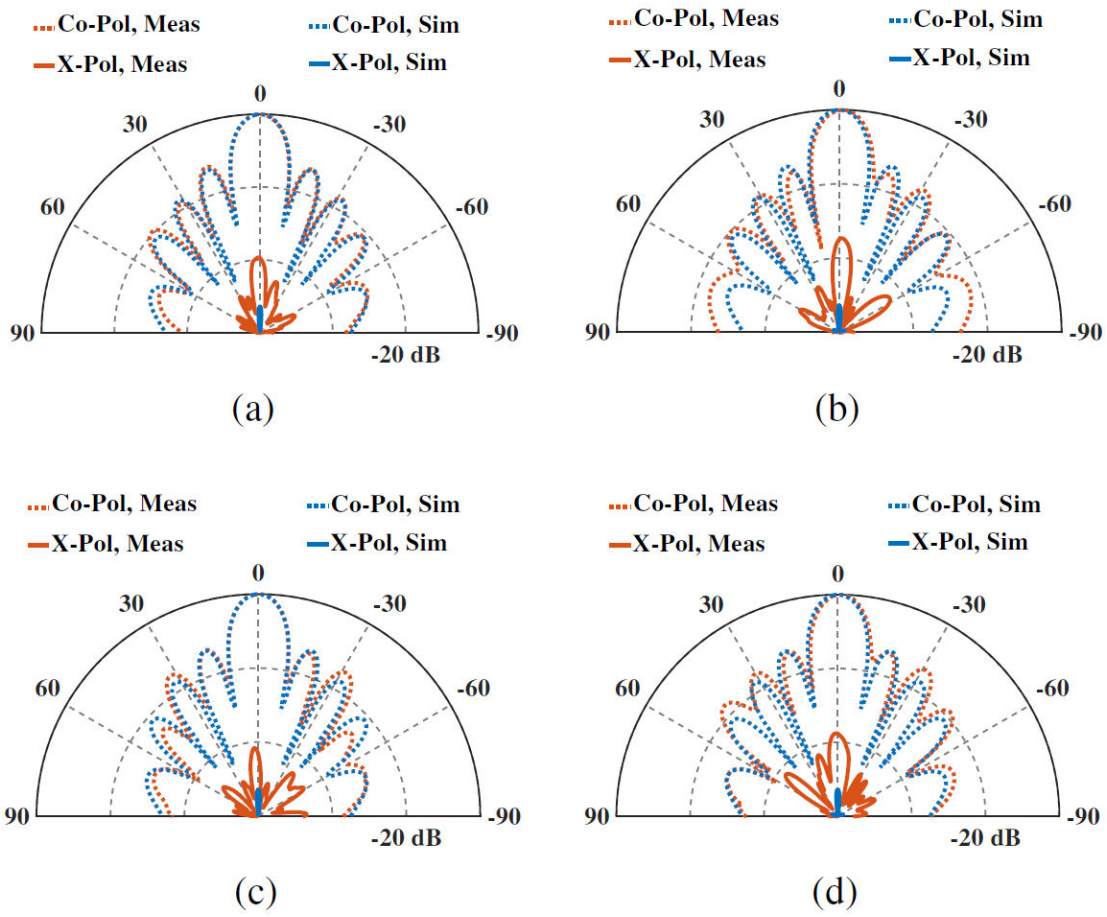

Fig. 4.5: Simulated and measured far-field pattern of central 8×8-element array at 2.7 GHz. (a) Horizontal polarization $\varphi = 0°$ plane, (b) Horizontal polarization $\varphi = 90°$ plane, (c) Vertical polarization $\varphi = 0°$ plane, (d) Vertical polarization $\varphi = 90°$ plane.

improved from -44 dB to -61 dB. In $\varphi = 0°$ plane the cross-polarization level for both polarizations even without image configuration is very low and it can be seen that the presented image configuration has a very limited effect on the cross-polarization pattern in the $\varphi = 0°$ plane.

4.1.2 The 12×12-element Array Antenna

The final 12×12-element array antenna is designed based on the designed 2×2-element subarray. The final 12×12-array consists of 36 of 2×2-element subarrays

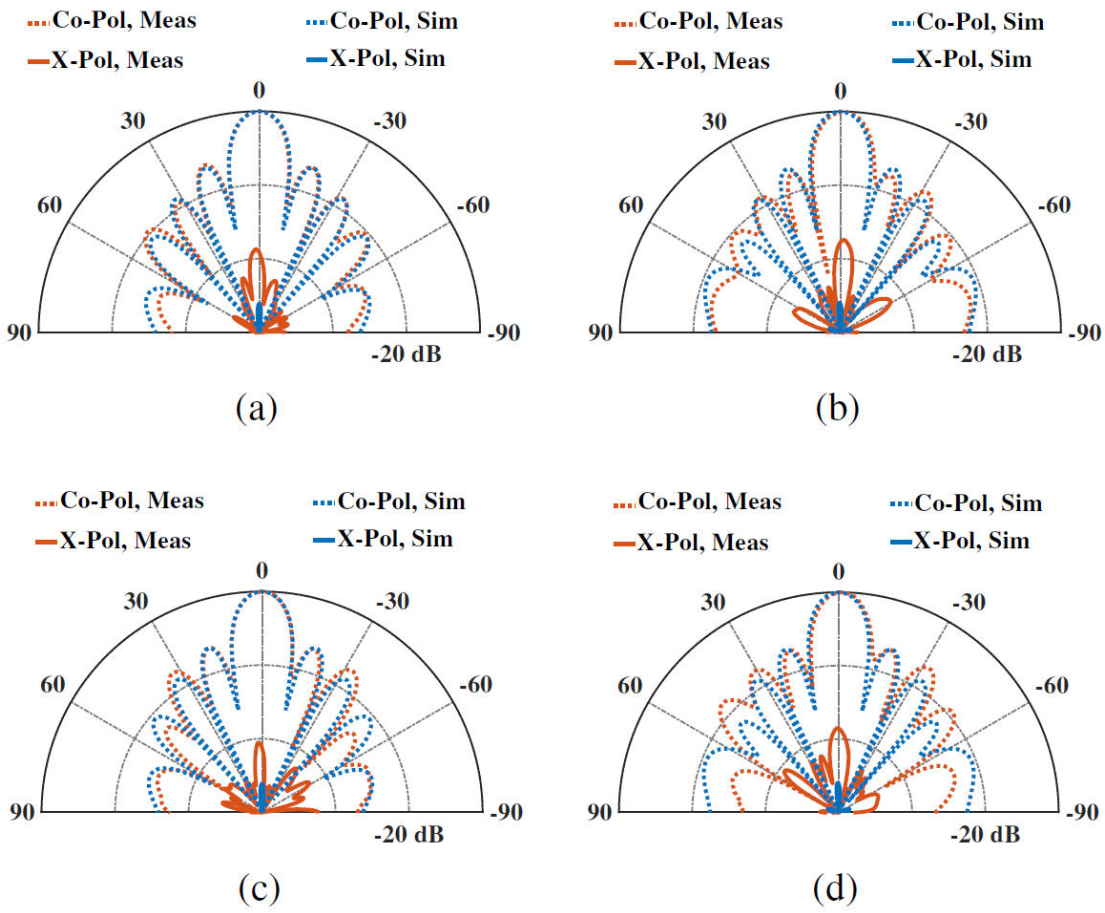

Fig. 4.6: Simulated and measured far-field pattern of central 8 × 8-element array at 2.8 GHz. (a) Horizontal polarization $\varphi = 0°$ plane, (b) Horizontal polarization $\varphi = 90°$ plane, (c) Vertical polarization $\varphi = 0°$ plane, (d) Vertical polarization $\varphi = 90°$ plane.

as is shown in Fig. 4.3. For the far-field measurement, one line of subarray from each side are terminated to reduce the edge effects on the radiation pattern of the 8 × 8-element array antenna. The central 8 × 8-element array is excited by the feed network that is shown in the Fig. 4.4. The antenna is tested in far-field anechoic chamber of ARRC. The measured radiation pattern of central 8 × 8-element array antenna is shown in Fig. 4.5, Fig. 4.6, Fig. 4.7, and Fig. 4.8, respectively. It is seen that there is good agreement between simulated and measured copolarization radiation patterns. The cross-polarization level in the

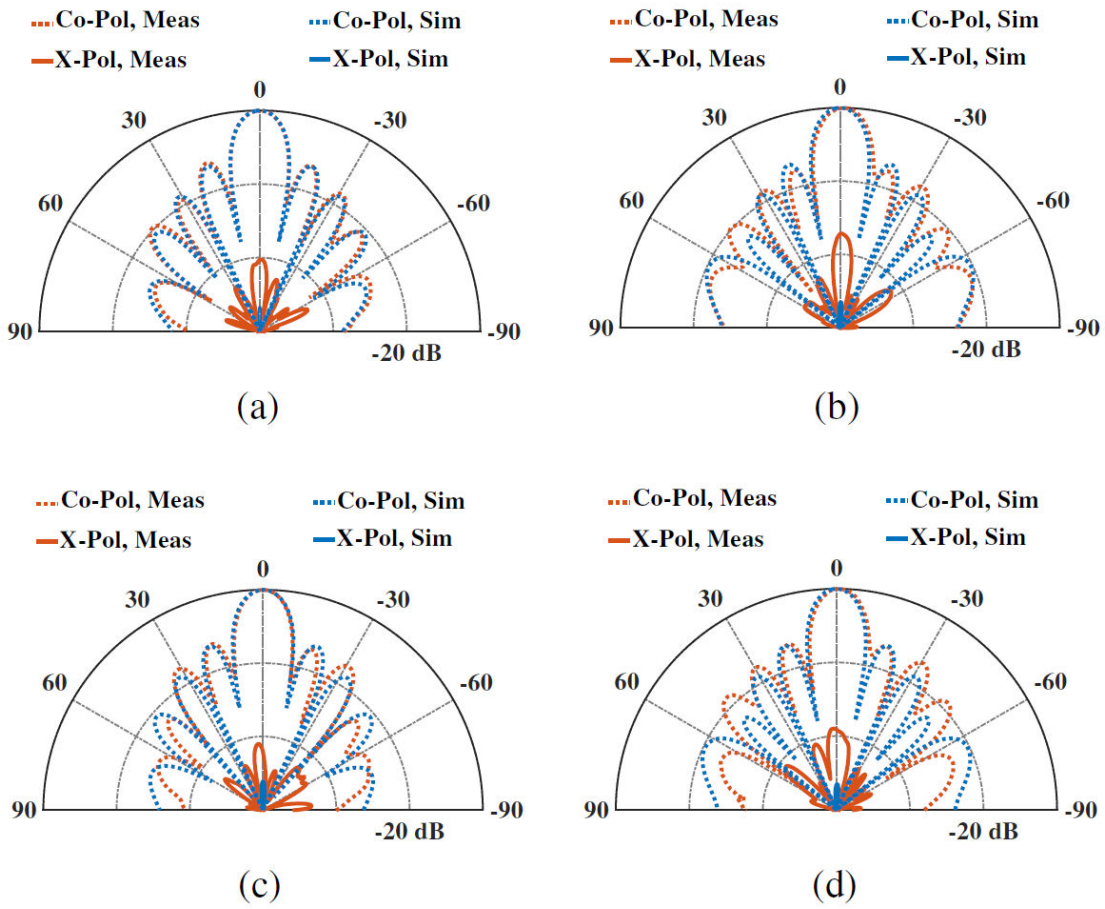

Fig. 4.7: Simulated and measured far-field pattern of central 8 × 8-element array at 2.9 GHz. (a) Horizontal polarization $\varphi = 0°$ plane, (b) Horizontal polarization $\varphi = 90°$ plane, (c) Vertical polarization $\varphi = 0°$ plane, (d) Vertical polarization $\varphi = 90°$ plane.

entire frequency band in the $\varphi = 0°$ and $\varphi = 90°$ planes for both polarizations in the simulation is lower than -50 dB. The measured cross-polarization level is increased in the entire frequency band in the $\varphi = 0°$ and $\varphi = 90°$ planes for both polarizations. The maximum measured cross-polarization in the far-field chamber is -36 dB. Although there is a 10 dB to 14 dB difference between simulated and measured results, the maximum measured cross-polarization is still very low. The main reasons for this discrepancy are backscattering from antenna huge wooden stand, cables, power dividers, and anechoic chamber equipment such as antenna

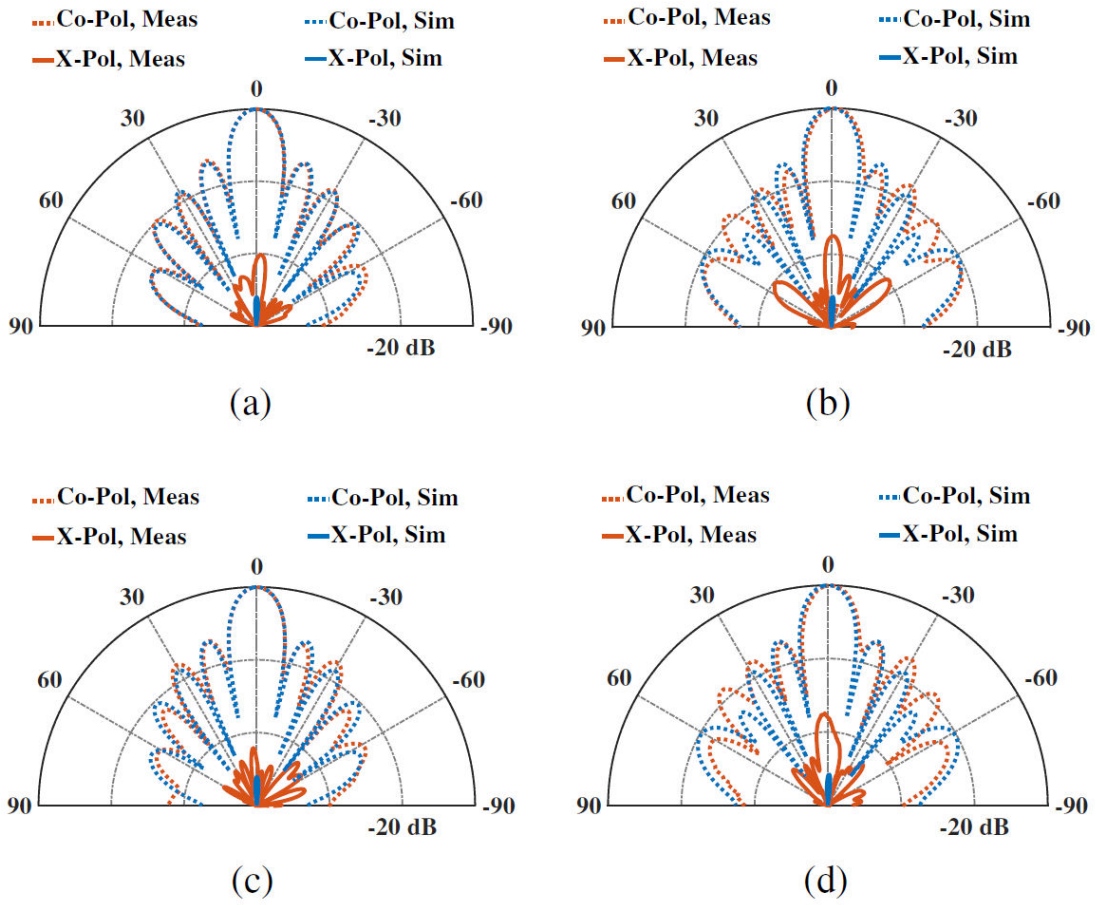

Fig. 4.8: Simulated and measured far-field pattern of central 8 × 8-element array at 3.0 GHz. (a) Horizontal polarization $\varphi = 0°$ plane, (b) Horizontal polarization $\varphi = 90°$ plane, (c) Vertical polarization $\varphi = 0°$ plane, (d) Vertical polarization $\varphi = 90°$ plane.

positioner and pedestal.

The radiation pattern of the designed array is also measured in the near-field chamber of ARRC. The moving probe is placed at 3λ distance from the surface of the antenna. For the near-field measurements, each element in the central 2 × 2-element subarray is excited while all other elements are terminated. The radiation pattern of each element in the 2 × 2-element subarray is measured separately and then these radiation patterns are processed by applying the array factor of 12 × 12-element array for calculating the array scanning radiation

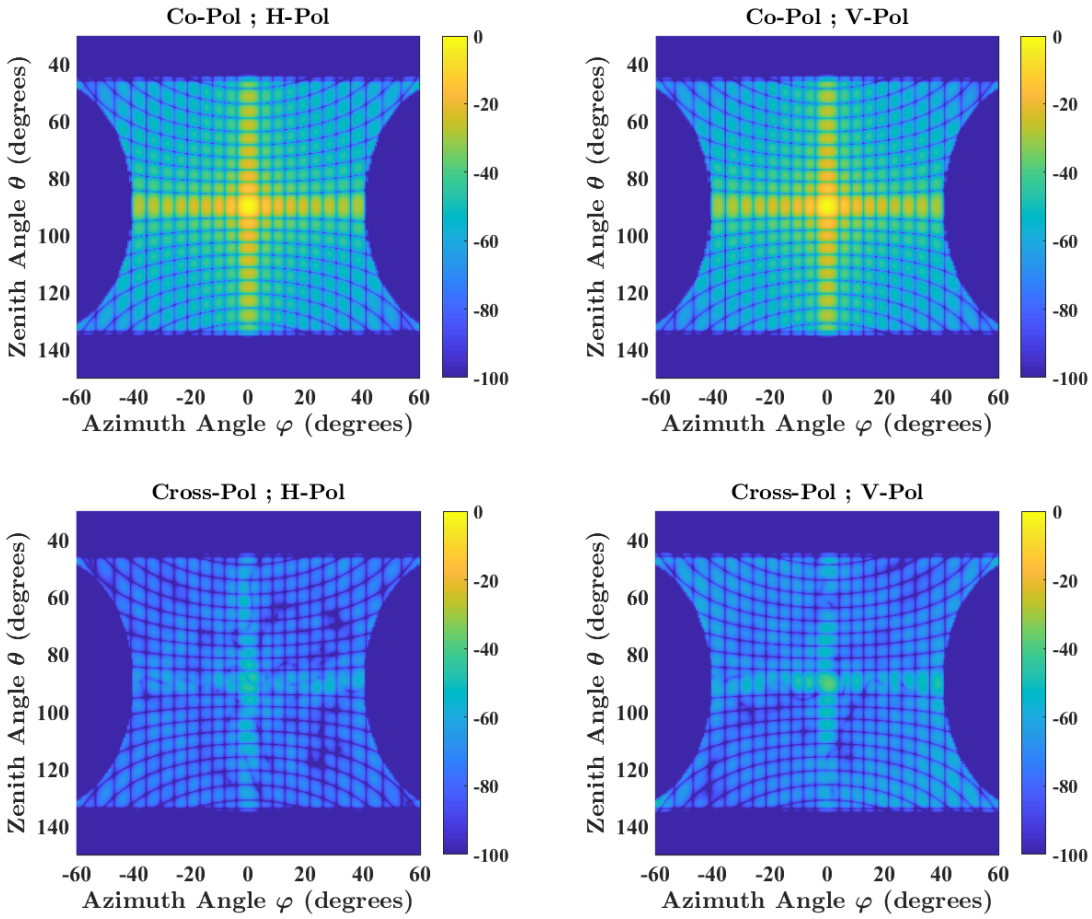

Fig. 4.9: 2D radiation pattern of the 12 × 12-element array at 2.8 GHz based on the measured embedded element pattern in the near-field chamber.

pattern. The broadside co and cross-polarization radiation pattern of the 12 × 12-element array for horizontal and vertical polarizations are shown in Fig. 4.9. The maximum cross-polarization level while $50^\circ \leq \theta \leq 130^\circ$ and $-60^\circ \leq \varphi \leq 60^\circ$ for horizontal polarization and vertical polarizations are -45.2 dB and -37.05 dB respectively. By applying phase shifts between the elements and considering the element location and orientation it is possible to calculate the array pattern at various scan angles. Since the embedded element pattern is measured from the 3λ near-field measurements, the radiation pattern is available from $\theta = -45^\circ$ to $\theta = 45^\circ$ and by considering the scan blindness angle the beam

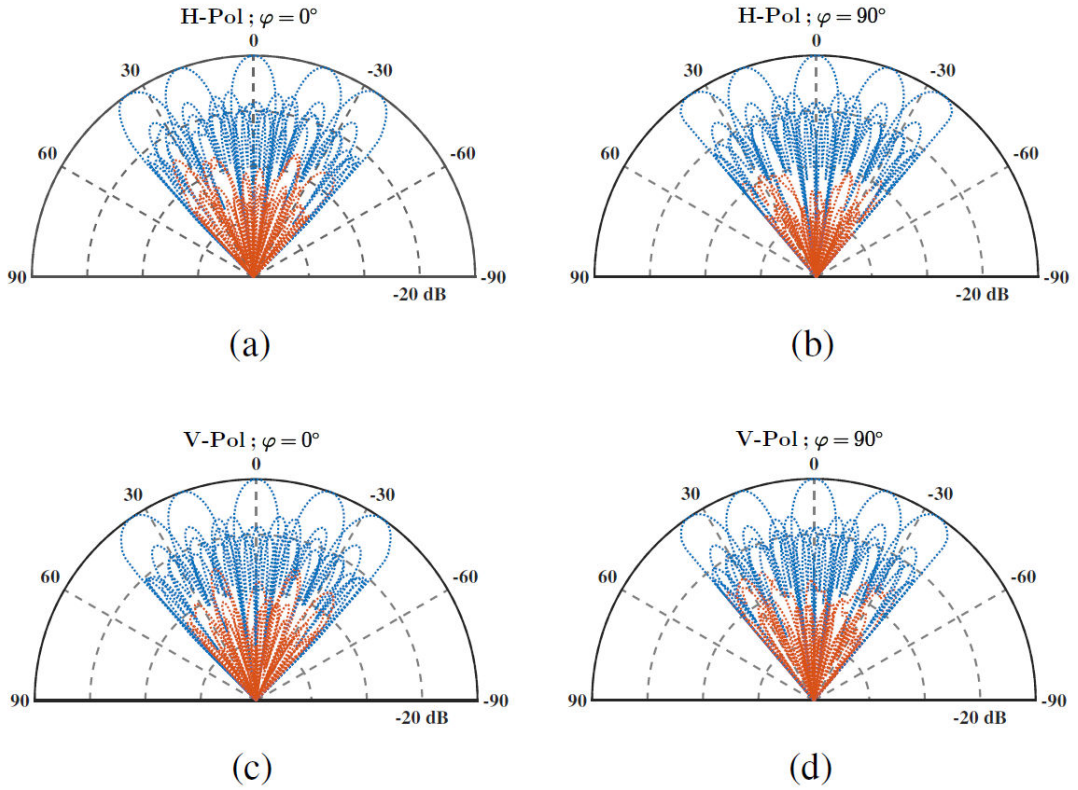

Fig. 4.10: Co- and cross-polarization radiation pattern of 12×12-element array at various scan angles in 2.8 GHz based on the measured embeded element pattern in the near-field chamber, (a) Horizontal polarization in the $\varphi = 0°$ plane, (b) Horizontal polarization in the $\varphi = 90°$ plane, (c) Vertical polarization in the $\varphi = 0°$ plane, (d) Vertical polarization in the $\varphi = 90°$ plane.

steering is performed from $\theta = -35°$ to $\theta = 35°$ for both polarizations in the $\varphi = 0°$ and $\varphi = 90°$ planes at 2.8 GHz.

The horizontal polarization radiation pattern of 12×12-element array antenna at 2.8 GHz in the $\varphi = 0°$ and $\varphi = 90°$ planes are shown in Fig. 4.10 (a) and Fig. 4.10 (b), respectively, and the antenna array vertical polarization are shown in Fig. 4.10 (c) and Fig. 4.10 (d), respectively. As shown in Fig. 4.10 in the $\varphi = 0°$ plane the copolarization radiation pattern maintains its shape but as it was expected the beam width increases. For the horizontal polarization cross-polarization level in the $\varphi = 0°$ plane will remain under -30 dB across the scanning range from

$\theta = -35°$ to $\theta = 35°$, and in the $\varphi = 90°$ plane, the cross-polarization level remains below -36 dB in the entire scan angle range. For the vertical polarization, the cross-polarization level in the $\varphi = 0°$ and $\varphi = 90°$ planes remains under -30 dB. This level of cross-polarization could be acceptable only if the H and V polarizations are coded [32].

4.2 Hybrid Feed Microstrip Patch Antenna Array; Balanced Probe-Feed and Symmetric Aperture Coupling Method

This section presents the design, fabrication and characterization of a high-isolation, low cross-polarization dual-polarized hybrid-fed patch antenna array for multifunction applications. Its hybrid feed design has been implemented, and the vertical and horizontal polarizations are excited by a balanced-probe feed and a slot-coupled feed, respectively. The presented simulations and measurements of the designed single element in section 2.1 have demonstrated an input isolation of 45 dB and 43 dB between the horizontal and vertical ports, respectively. In this section, for further improvement in the cross-polarization level, the image feed method is also implemented, and a 2×2-element array made of designed elements with image configuration has been fabricated. The simulated and measured S-parameter and radiation patterns of the horizontal and vertical polarizations of the designed 2×2-element array are presented and the measured cross-polarization level of less than -37 dB is achieved. To examine the performance of the designed element in an array, a 3×3-element array of designed 2×2-element subarray is fabricated and tested. In the 6×6-element antenna array measurements, -35.4

dB and -36 dB cross-polarization levels for horizontal and vertical polarizations are achieved respectively. Also, using the measured embedded element patterns, the cross-polarization of level lower than -36 dB for scan angles up to 45°is achieved.

4.2.1 2×2-element Array Configuration

For further improvement on the cross-polarization level, the image feed method is applied to the 2×2-element array of the designed single element [48], [53]. In this configuration, the upper right and lower left elements in the 2×2-element array are mirrored with respect to the vertical plane. In this configuration, the phase of the copolarization pattern of mirrored element will be 180° out of phase compared to the original element. On the other hand, the phase of cross-polarization pattern won't change by mirroring the element. To compensate for the 180° phase shift in the copolarization pattern, the mirrored elements are excited with a 180° phase shift. Consequently, the copolarization pattern of two elements will be in phase and the cross-polarization patterns will be 180° out of phase, so the cross-polarization pattern will be canceled, especially in the principal planes.

The geometry of the fabricated 2×2-element array antenna is shown in Fig. 4.11. The fabricated array antenna is tested in the far-field anechoic chamber of the ARRC and the measured results at 2.7 GHz, 2.8 GHz, and 2.9 GHz are presented in Fig. 4.12. Also, not shown here, the simulated cross-polarization level of the 2×2-element array with image configuration is below -80 dB for horizontal polarization and below -56 dB for vertical polarization. As shown in Fig. 4.12, the maximum measured cross-polarization level in the whole bandwidth is below -40 dB above the ground plane ($\theta = -90°$ to $\theta = 90°$) for both polarizations in

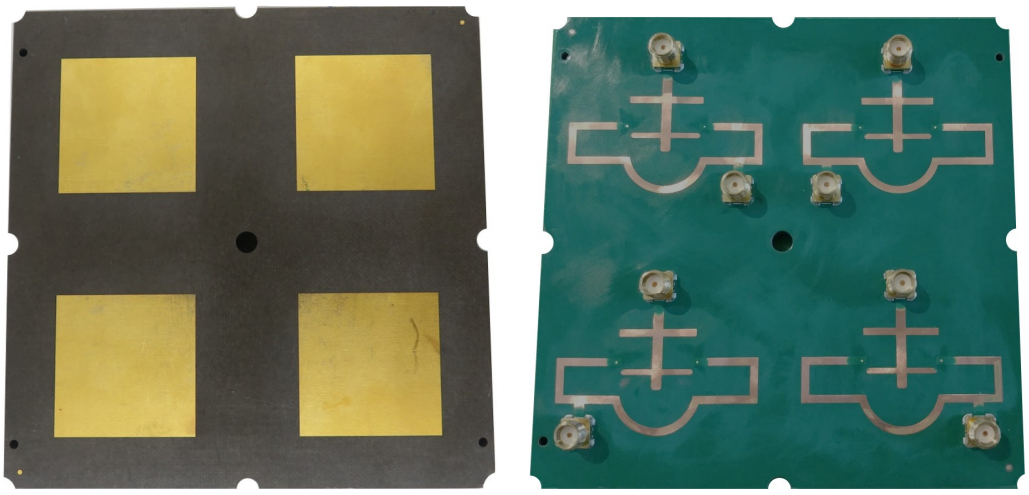

(a) (b)

Fig. 4.11: Geometry of fabricated 2 × 2-element array of designed single element with image configuration. (a) Top view, (b) Bottom view.

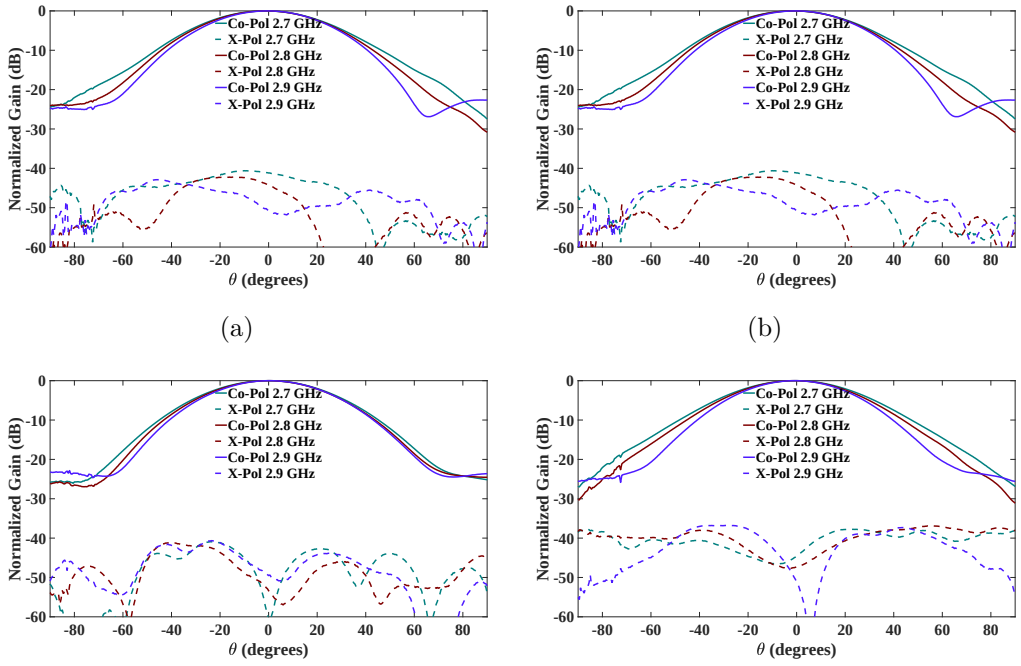

(a) (b)

(c) (d)

Fig. 4.12: Measured normalized radiation pattern of 2 × 2-element array of designed single element with image configuration. (a) H-Pol, $\varphi = 0°$; (b) H-Pol, $\varphi = 90°$; (c) V-Pol, $\varphi = 0°$; (d) V-Pol, $\varphi = 90°$

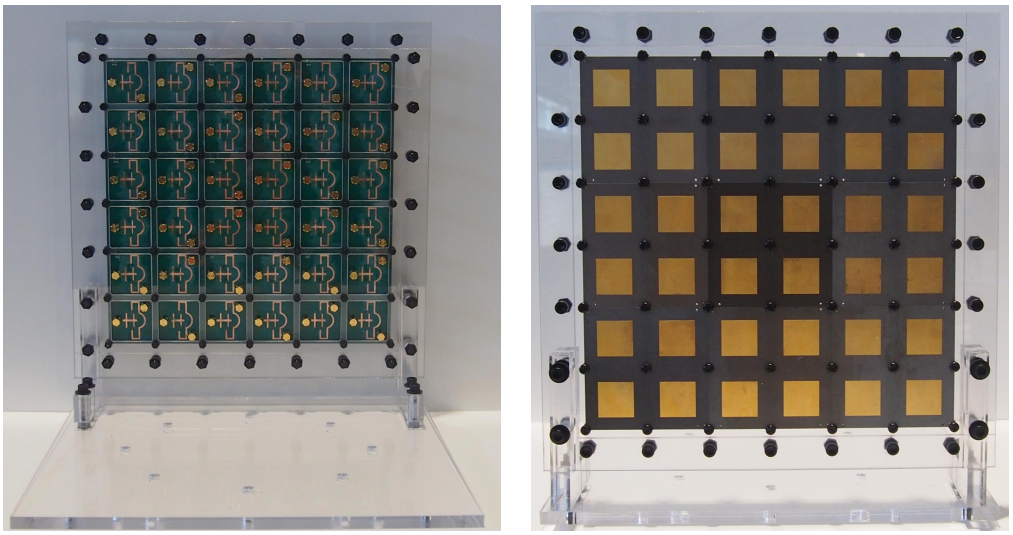

(a) (b)

Fig. 4.13: Geometry of fabricated 6 × 6-element array of designed single element with image configuration. (a) Back view, (b) Front view.

the $\varphi = 0°$ plane. In the $\varphi = 90°$ plane, the cross-polarization level is below -37 dB.

Although there is a gap between the maximum measured and simulated cross-polarization levels, it should be noted that the difference between -56 dB and -40 dB is less than 10^{-4}. Therefore, small backscattering from the cable and pedestal could increase the cross polarization to -40 dB. Also, the cross-polarization level of the standard transmitter antenna in the test will increase the measured cross-polarization level.

4.2.2 6×6-element Array

A 6×6-element array of proposed dual-polarized hybrid feed patch antenna has been designed and fabricated to validate the radiation characteristics of the 2 × 2-element subarray, especially its low cross-polarization level. As shown in Fig. 4.13, the fabricated 6 × 6-element array is made of 9, 2 × 2-element subarrays,

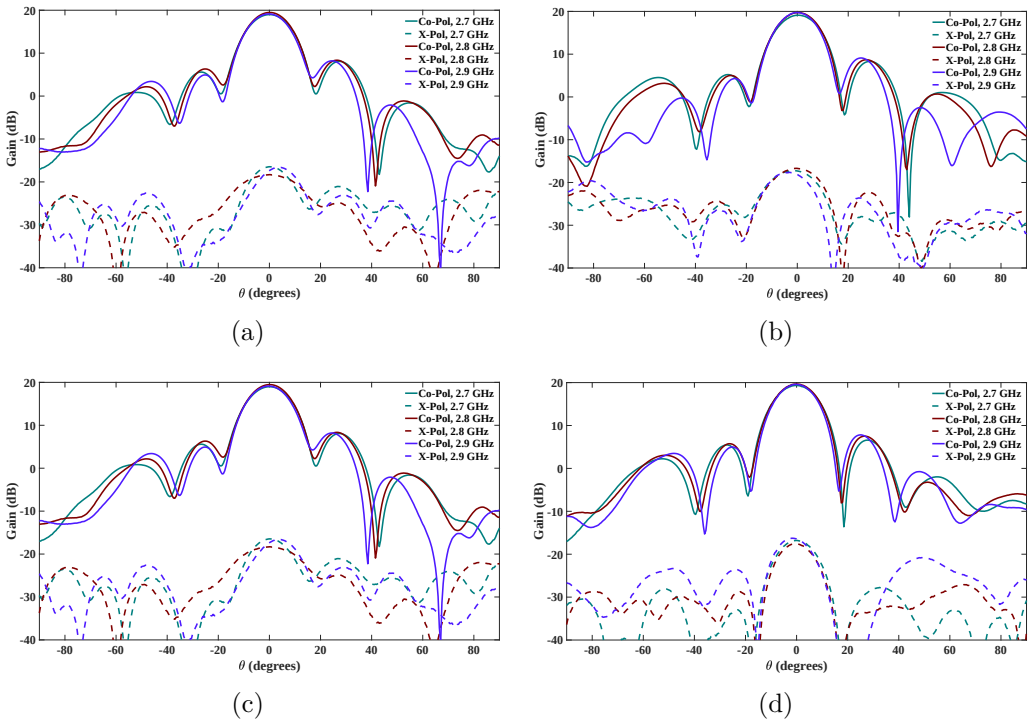

Fig. 4.14: Measured radiation pattern of 3×3-element array of designed 2×2-element subarray (6×6-element array) at 2.7 GHz, 2.8 GHz, and 2.9 GHz; (a) H-Pol, $\varphi = 0°$, (b) H-Pol, $\varphi = 90°$, (c) V-Pol, $\varphi = 0°$, (d) V-Pol, $\varphi = 90°$.

mounted on a fixture made of Polycarbonate and Acrylic.

The radiation pattern of the fabricated 6×6-element array is measured in the far-field anechoic chamber of ARRC. Fig. 4.14 shows the array antenna horizontal and vertical polarizations' radiation patterns at 2.7 GHz, and 2.8 GHz, and 2.9 GHz. In the $\varphi = 0°$ plane the cross-polarization level is below -35.4 dB and -36.1 dB for horizontal and vertical polarization, respectively. As shown in Fig. 4.14 in $\varphi = 90°$ plane the cross-polarization level for horizontal polarization is below -35.5 and for the vertical polarization it is below -36 dB.

The 6×6-element array is used to predict the co and cross-polarization level of large arrays by using its measured embedded element pattern. Since the elements in the center 2×2-element subarray are not identical, each element in

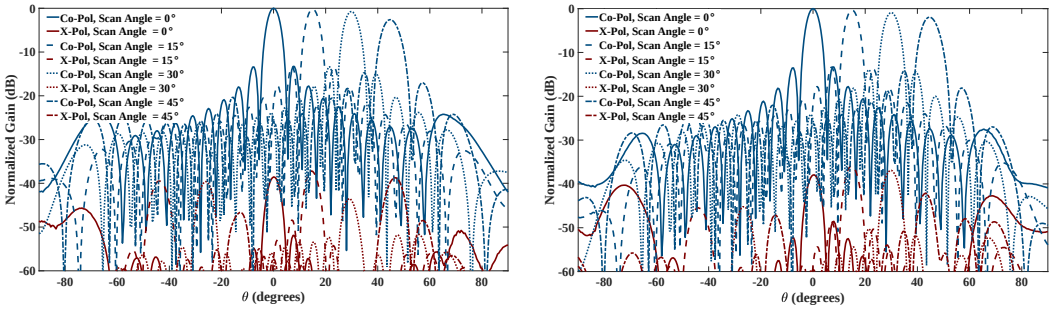

(a) (b)

Fig. 4.15: Emulated radiation pattern of 3 × 3-element array of designed 2 × 2-element subarray (6 × 6-element array) at 2.7 GHz, 2.8 GHz, and 2.9 GHz; (a) H-Pol, $\varphi = 0°$, (b) H-Pol, $\varphi = 90°$.

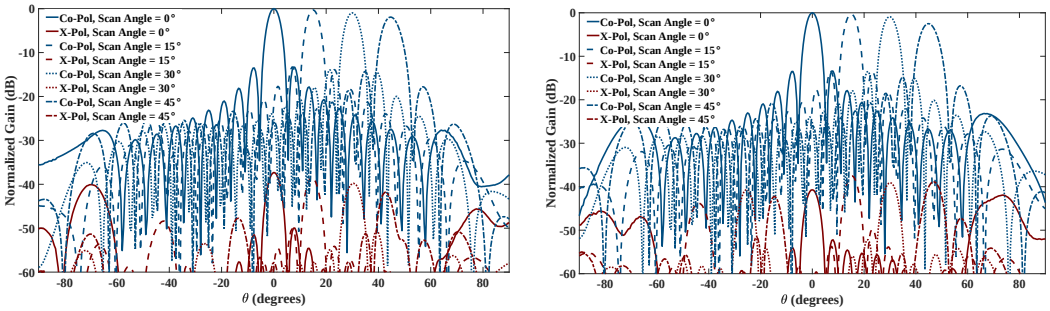

(a) (b)

Fig. 4.16: Emulated radiation pattern of 3 × 3-element array of designed 2 × 2-element subarray (6 × 6-element array) at 2.7 GHz, 2.8 GHz, and 2.9 GHz; (a) V-Pol, $\varphi = 0°$, (c) V-Pol, $\varphi = 90°$.

the center 2 × 2-element subarray is separately excited while all other elements are terminated. Accordingly, the four measured embedded element patterns are used to characterize a large array radiation pattern. The measured embedded element patterns have been used to calculate the radiation pattern of a 20 × 20-element array. The horizontal and vertical polarizations radiation patterns of the 20 × 20-element array in $\varphi = 0°$ and $\varphi = 90°$ planes at 0°, 15°, 30°, and 45° scan angles are shown in Fig. 4.15 and Fig. 4.16. For horizontal polarization in $\varphi = 0°$ and $\varphi = 90°$ planes, the maximum cross-polarization level at broadside is below -38.55 dB and cross-polarization level remains under -36

dB across the scanning to 45°. For the vertical polarization in $\varphi = 0°$ and $\varphi = 0°$ planes, the cross-polarization level at broadside is below -38 dB and it remains below -36 dB while the main beam direction is steered to 45°.

4.3 Hybrid Feed Microstrip Patch Antenna Array; Balanced and Symmetric Aperture Coupling Method

In this section, the radiation characteristics of a dual-polarization, aperture coupled hybrid feed microstrip patch antenna is presented. As mentioned in 2.3, single element the horizontal and vertical polarization are excited using aperture-coupling method. The measured cross-polarization level of lower than -30 dB and input isolation of better than 50 dB are achieved for the designed single element. To achieve a better cross-polarization level, the 2×2-element array of the designed single element while the horizontal polarization ports are mirrored with respect to the vertical plane is designed and fabricated. Using the cross-polarization suppression methods, the cross-polarization level of better than -39 dB is achieved in the measurement results. Finally, to characterize the scan performance of the designed element and subarray, a 4×10-element array of proposed hybrid feed element is fabricated and the cross-polarization level of lower than -45 dB is achieved while scanning up to 45°.

4.3.1 2×2-element Array Configuration

Cross-polarization suppression in dual-linear polarization array antenna is studied in many papers [52], [53]. Any dual-polarized antenna requires two individual ports for exciting orthogonal polarizations, and more or less in dual-polarized antennas it is desired to achieve low cross-polarization level. An

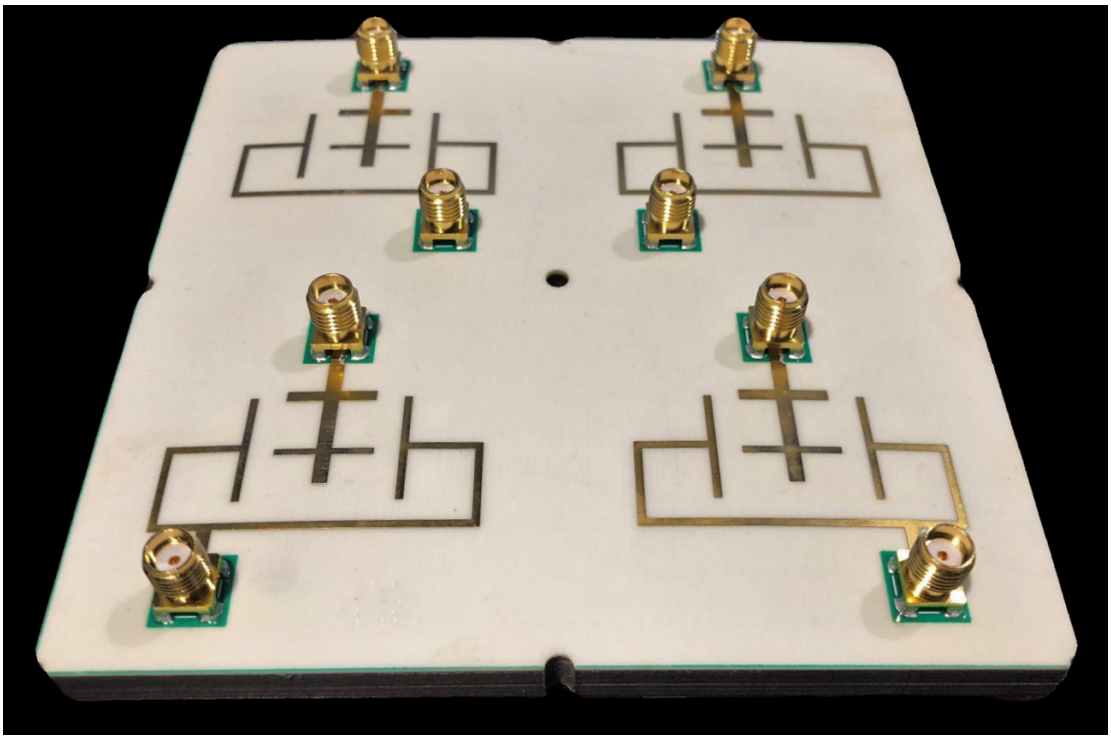

Fig. 4.17: Fabricated 2×2-element subarray with the image configuration.

ideal dual-polarized patch antenna can be designed while each polarization is excited with two 180° out phase ports which is called ideal differential feed patch antenna. The advantage of using ideal differential feed patch antenna is its extremely low cross-polarization level, especially in the principal planes. However, an ideal differential feed requires external 180° phase shifters. In a large array antenna, the increased number of connectors, cables, and phase shifters would significantly increase fabrication costs. An alternative solution for reducing cross-polarization level is to arrange the elements of the array into the groups of 2×2-element identical subarray in which the horizontal polarization ports are mirrored with respect to vertical planes. This method of improving cross-polarization level is implemented in this design. The geometry of fabricated 2×2-element subarray of the designed single element with the image configuration is shown in Fig. 4.17. Similar to an ideal differential feed antenna

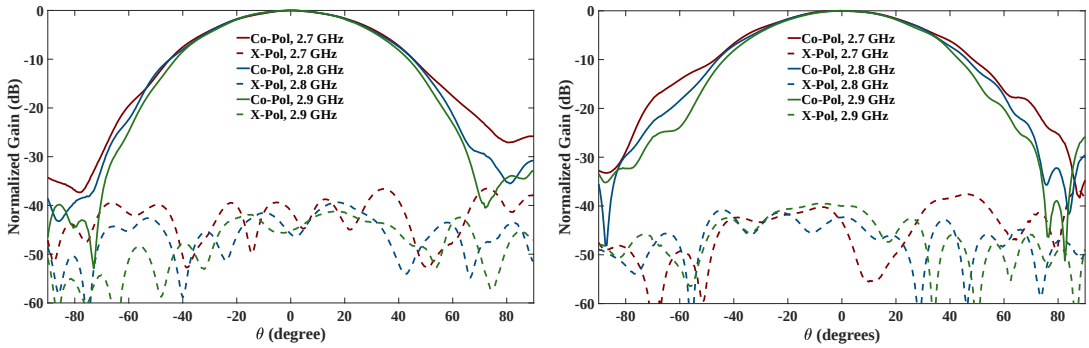

(a) (b)

Fig. 4.18: Measured radiation pattern of the 2×2-element subarray with image configuration at 2.7 GHz, 2.8 GHz, and 2.9 GHz; (a) H-pol, $\varphi = 0°$; (b) H-pol, $\varphi = 90°$.

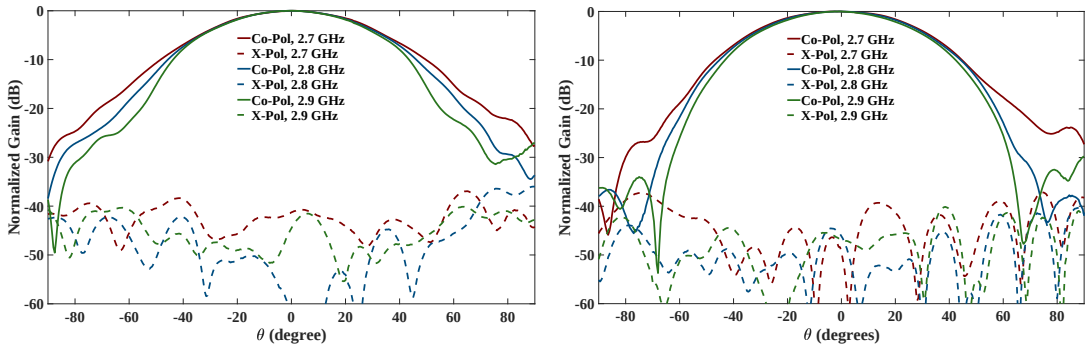

(a) (b)

Fig. 4.19: Measured radiation pattern of the 2×2-element subarray with image configuration at 2.7 GHz, 2.8 GHz, and 2.9 GHz; (a) V-pol, $\varphi = 0°$; (b) V-pol, $\varphi = 90°$.

the mirrored ports are excited with a 180° phase shift.

The measured radiation pattern of the fabricated 2 × 2-element subarray of the designed single element is shown in Fig. 4.18 and Fig. 4.19. As seen from Fig. 4.18 and Fig. 4.19, the cross-polarization level for both polarizations in the $\varphi = 0°$ and $\varphi = 90°$ planes in the entire frequency band is around -40 dB. At 2.8 GHz, the horizontal polarization cross-polarization level is better than -40 dB and -41 dB in $\varphi = 0°$ and $\varphi = 90°$ planes, respectively. For vertical polarization at 2.8 GHz, the maximum measured cross-polarization level is below -37 dB in

$\varphi = 0^\circ$ planes and less than -41 dB in $\varphi = 90^\circ$ plane. Also not shown here, the simulated cross-polarization level in both principal planes is below -50 dB. The discrepancy between simulated and measured cross-polarization level is the result of unideal measurement environment such as the cross-polarization level of the transmitter antenna and backscattering of the antenna cable and positioner and possible fabrication errors.

4.3.2 Array Design

To characterize the scan performance of the designed single element and subarray, a 2 × 5-element array of the 2 × 2-element subarray is fabricated. Fig. 4.20 (a) shows the geometry of the fabricated 4 × 10-element array which is for characterizing the co- and cross-polarization radiation pattern of the horizontal and vertical polarizations at different scan angles in the $\varphi = 0^\circ$ plane. For measuring low cross-polarization levels, the alignment of the antenna under test (AUT) with transmitter antenna, plays a key role. Considering perfect condition in the anechoic chamber, any misalignment between AUT and transmitter antenna will result in measuring the cross-polarization level in off principle planes. For a perfect alignment between AUT and the transmitter antenna, the 2 × 2-element subarrays are mounted on a fixture which is made from polycarbonate and plexiglass. The polycarbonate and plexiglass components of the antenna fixture are precisely processed by a laser cutting machine. The two white components of this fixture are made from ABS by using a 3-D printer. As seen from Fig. 4.20 (b), to measure the radiation pattern and characterize its scanning performance in $\varphi = 90^\circ$ plane, the 2 × 2-element subarrays are rotated 90°.

Although a 4×10-element array antenna is fabricated for characterizing the

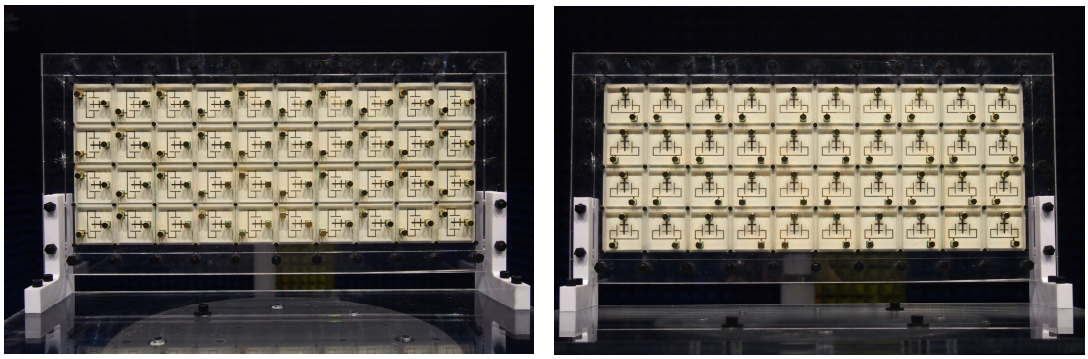

(a) (b)

Fig. 4.20: Fabricated 4×10-element array for characterizing the antenna performance; (a) in $\varphi = 0^\circ$ plane; (b) in $\varphi = 90^\circ$ plane.

performance of the designed single element, for MAPR applications final array dimensions could be as large as a cylindrical array antenna with 10 m diameter. Therefore, to reduce the edge effects on the array radiation pattern, one element form each side is terminated and the radiation pattern of the central 2×8-element array is measured. Also, it is worth noting that, in cylindrical geometry, beam steering is only required on principle planes and since the radiation pattern of the elements in a large cylindrical array antenna is similar to the planar array antenna, the antenna is tested while the element and subarrays are arranged as a 4×10-element array configuration. The radiation pattern of the 4×10-element array of the designed subarray (2×8-element array) is shown in Fig. 4.21 and Fig. 4.22. Fig. 4.21 shows the horizontal and vertical polarization radiation pattern of the first array antenna in $\varphi = 0^\circ$ plane. As seen from Fig. 4.21, the cross-polarization level at 2.8 GHz is below -44 dB and -39 dB for horizontal and vertical polarization respectively. The radiation pattern of the central 2×8-element array antenna in the $\varphi = 90^\circ$ plane is measured by using the array antenna shown in Fig. 4.22. According to the measurements results in $\varphi = 90^\circ$ plane, the cross-polarization level for horizontal antenna vertical polarization at 2.8 GHz is better than -44

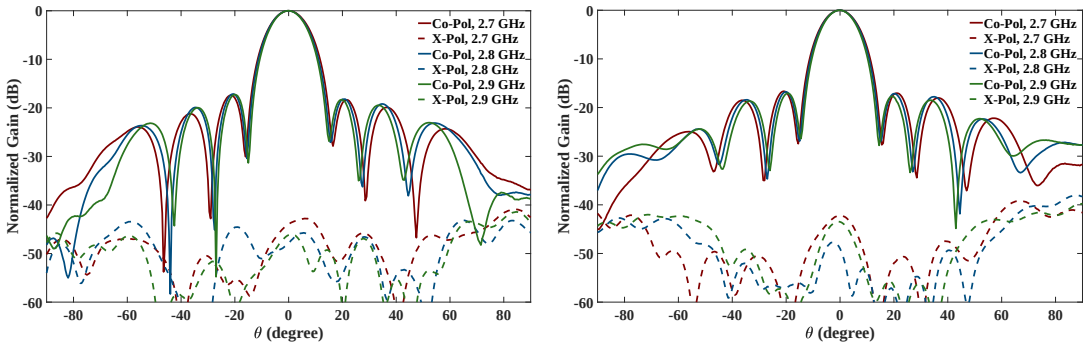

(a) (b)

Fig. 4.21: Measured radiation pattern of the central 2×8-element array in the fabricated 4×10-element array at 2.7 GHz, 2.8 GHz, and 2.9 GHz; (a) H-pol, $\varphi = 0°$; (b) V-pol, $\varphi = 0°$.

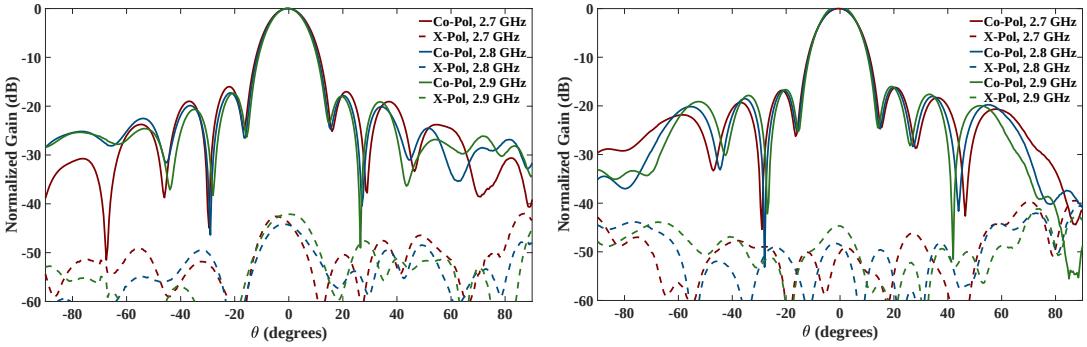

(a) (b)

Fig. 4.22: Measured radiation pattern of the central 2×8-element array in the fabricated 4×10-element array at 2.7 GHz, 2.8 GHz, and 2.9 GHz; (a) H-pol, $\varphi = 90°$; (b) V-pol, $\varphi = 90°$.

dB and -41 dB, respectively. It should be mentioned that the measured cross-polarization level at main beam area for the horizontal and vertical polarization are below -44 dB and -48 dB, respectively.

The radiation pattern of the central 2×8-element array antenna is measured according to Unit Excitation Active Element Pattern (UEAEP) method [57], [58]. In this method, the radiation pattern of each element is measured while all other elements were terminated. The amplitude and phase of all measured active element patterns are imported into Matlab and the required phase shift between

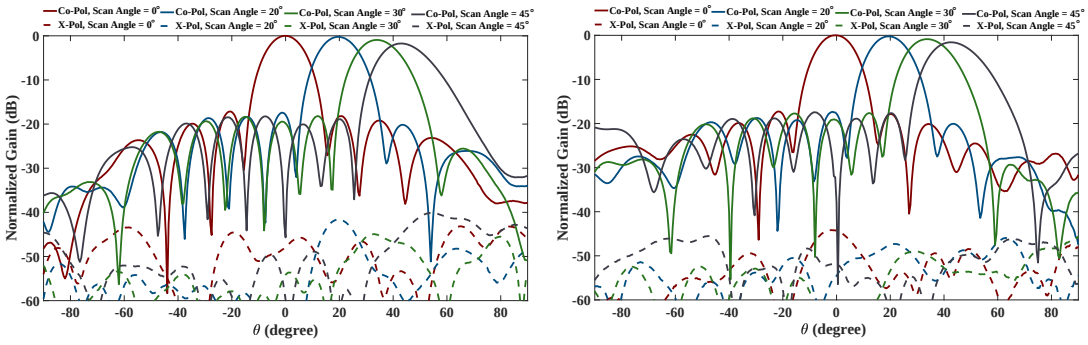

(a) (b)

Fig. 4.23: Measured scan radiation pattern of the central 2×8-element array in the fabricated 4×10-element array at 2.7 GHz, 2.8 GHz, and 2.9 GHz; (a) H-pol, $\varphi = 0°$; (b) H-pol, $\varphi = 90°$.

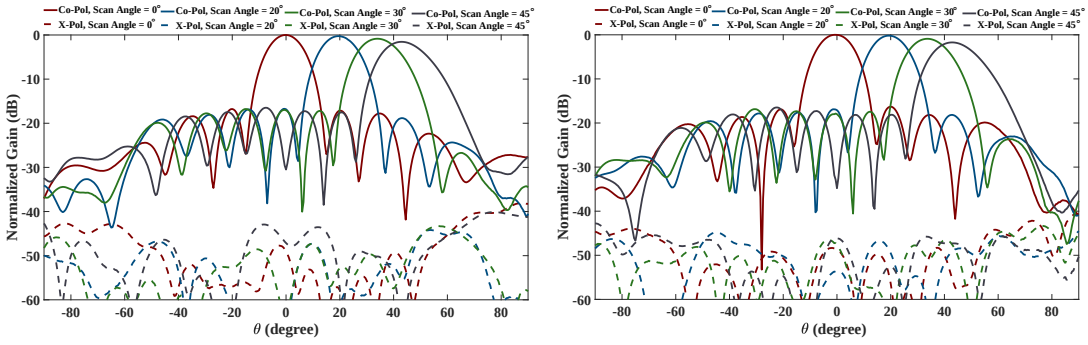

(a) (b)

Fig. 4.24: Measured scan radiation pattern of the central 2×8-element array in the fabricated 4×10-element array at 2.7 GHz, 2.8 GHz, and 2.9 GHz; (a) V-pol, $\varphi = 0°$; (b) V-pol, $\varphi = 90°$.

elements is applied to steer the array radiation pattern. It has not escaped our notice that while measuring the active element pattern, the active reflection coefficient magnitude of the fully excited array at the scan angles is contributing to the measured realized gain. Therefore, measuring the active element pattern for characterizing the array scanning performance can be used to reduce the cost and risk of the system failure in the measurements of the prototypes.

Following the UEAEP method, the measured normalized scanning patterns of the array antenna in $\varphi = 0°$ and $\varphi = 90°$ planes at 2.8 GHz are shown in Fig.

4.23 and Fig. 4.24. Also, 25 dB Taylor amplitude tapering is applied to reduce the sidelobe level. For horizontal polarization, the cross-polarization level while scanning up to 45° in $\varphi = 0°$ and $\varphi = 90°$ planes, stays below -40 dB and -44 dB, respectively. For the vertical polarization, the cross-polarization level of better than -40 dB and -39 dB is achieved in scanning up to 45° in $\varphi = 0°$ and $\varphi = 90°$ planes respectively. It should be mentioned that the reported cross-polarization level is the peak of the cross-polar pattern at 2.8 GHz above the ground plane ($-90° < \theta < 90°$). In the main beam area, the cross-polarization level for the scanning up to 20°, which is the maximum required beam steering for cylindrical geometry, is mostly below -45 dB. This level of the cross-polarization level could satisfy the MPAR requirements.

The proposed three different antennas for MPAR application are compared in Table 4.1. In terms of cross-polarization level and input isolation between polarizations, the hybrid feed designs, especially the hybrid aperture-coupled antenna has a better performance compared to the asymmetric non-overlapping aperture-coupled design. The antenna electrical and geometrical symmetry can be improved by using hybrid feeding method. Using balanced probe feed design in the second hybrid patch antenna will result in having multilayer vias which increase the antenna fabrication cost and complexity. However, in the hybrid design, the antenna fabrication complexity has been improved by using the hybrid aperture coupling method. Overall as it is stated in Table 4.1, the second hybrid design has the best performance among the proposed three designs.

Table 4.1: Comparison of the proposed antennas electromagnetic and non-electromagnetic properties.

Design	Cross-pol level (dB)	Input Isolation (dB)	Design Symmetry	Fabrication Complexity
I. Asymmetric Aperture-Coupled	-30 dB up to 35° scanning	41 dB	Low	Low
II. Hybrid Feed (Probe Feed)	-36 dB up to 45° scanning	43 dB	High	High
III. Hybrid Feed (Aperture-Coupled)	-39 dB up to 45° scanning	50 dB	High	Low

Chapter 5

Antennas for Cylindrical Polarimetric Phased Array Radar (CPPAR)

5.1 Planar or Cylindrical Geometry?

In a four-faced planar phased array radar to scan the required space, each fixed faced should cover 90° of the surrounding azimuths. This means that the radiation pattern of each planar array antenna should be steered from -45° to +45° in azimuth direction. For NWS weather applications, the maximum required scan angle in the elevation direction is 20°. The main disadvantage of using planar phased array antennas compared to conventional mechanically steered reflector antennas is the change in beam characteristics and polarization coupling depending on the beam direction. In a planar array antenna, it is possible to achieve a low cross-polarization level while the beam steering is performed on principle planes, however, if the beam steering is required on off-principle planes, having low cross-polarization which would be acceptable for MPAR applications is almost impossible. In [30] Lei et al. show that at the maximum steering angle of a planar array antenna for weather application, the cross-polarization level increases to -12.4 dB which is not acceptable for weather radar measurements. Also, it is worth noting that, the antenna performance and

the accuracy of weather measurement could be affected by radome conditions (e.g., wet radome) and several investigations have been conducted to illustrate these effects on antenna radiation pattern and the polarimetric biases[59]–[63].

Based on weather radar requirements and deficiencies of the planar array antenna, a cylindrical polarimetric phased array antenna is designed and proposed for MPAR application. The CPPAR demonstrator is a 2m diameter cylindrical array antenna designed and fabricated by the Advanced Radar Research Center (ARRC) of the University of Oklahoma [64]. As shown in Fig. 5.1 M×N element cylindrical array antenna consists of N rows of M-element circular array antenna. For the cylindrical array antenna, the beam is formed from a 90° sector of a cylinder, and for the beam steering in azimuth, an active column from one side of the activated 90° sector (Column A in the Fig. 5.1 (b)) is turned off and another inactive column from another side of the 90° sector (Column B in the Fig. 5.1 (b)) is turned on. So, the beam is always formed from a 90° sector of a cylinder and the scanning on a diagonal plane is not required. Also, due to the symmetry of cylinder around its axis, the radiation pattern will be always symmetric and won't change for beam steering in azimuth. Therefore, the beam steering is only required on principle planes which results in a low cross-polarization level as the cylindrical array antenna scans [52]. Thus, for MPAR weather surveillance, the cylindrical geometry is preferred. However, it is difficult to characterize the radiation pattern of an element in a cylindrical geometry. But, because the radiation pattern of an element in a large cylindrical array antenna is similar to the radiation pattern of the same element in a large planar array [65, Figure 6.18.], in this dissertation the embedded element and subarray radiation patterns have been characterized using planar array antennas.

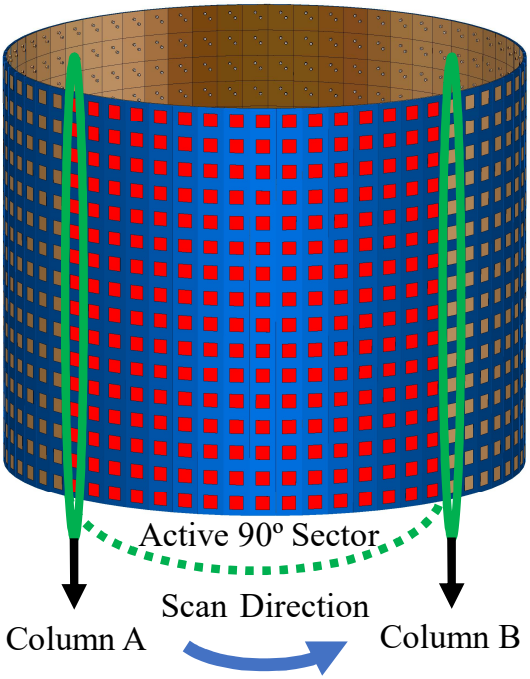

Fig. 5.1: Cylindrical array antenna azimuth scanning [43].

5.2 Conformal Arrays Radiation Pattern

The geometry of an $M \times N$-element cylindrical array antenna is shown in Fig. 5.2. As is shown in Fig. 5.2, the array consists of N, M-element linear arrays, which are placed on a circular ring with a radius of "a". Circular arrays possess the advantage of having a symmetrical radiation pattern in the azimuth, which makes the circular and cylindrical array configurations very interesting for radar applications [66]. The array radiation pattern for the circular array of radius "a" with N elements at locations $\varphi_0 = n\Delta\varphi$ can be written as:

$$E(\theta, \varphi) = \sum_{n=0}^{N-1} a_n F_n(\theta, \varphi) e^{jkasin\theta cos(\varphi - n\Delta\varphi)} \tag{5.1}$$

where a_n is the excitation coefficients of circular array elements and k is the wavenumber. In general, because of symmetry, the element radiation patterns

are also dependent on the element location. The effect of element location in the array can be taken into account with:

$$F_n(\theta, \varphi) = f(\theta, \varphi - n\Delta\varphi) \tag{5.2}$$

where $f(\theta, \varphi)$ is the embedded element radiation pattern. The radiation pattern of the cylindrical array comes from the collective contributions from the array elements on the cylindrical surface. The radiation pattern of an $M \times N$-element cylindrical array antenna when the main beam points to angle (θ_0, φ_0) can be written as follows:

$$\begin{aligned} E(\theta, \varphi) = e^{-j((M-1)/2)\psi_z} \sum_{m=1}^{M} e^{j(m-1)(\psi_z - kd_z cos\theta_0)} \\ \times \sum_{n=0}^{N-1} a_{mn} F_n(\theta, \varphi) e^{jka(sin\theta cos(\varphi - n\Delta\varphi) - sin\theta_0 cos(\varphi_0 - n\Delta\varphi))} \end{aligned} \tag{5.3}$$

where a_{mn}, and d_z are the amplitude weight applied to the mnth element and spacing between elements along z axis of the CPPAR, respectively and $\psi_z = kd_z cos\theta$. The aperture distribution and excitation coefficient of cylindrical array elements can be calculated by optimization methods. Also, the excitation amplitude of mnth element that is equivalent to WSR-88D illumination taper [24], can be calculated according the following equation:

$$a_{mn} = \frac{(1 - \frac{4\left[a^2 sin^2(\varphi_0 - \varphi') + z_{mn}^2\right]}{D^2})^c + b}{1 + b} \tag{5.4}$$

Where "a" for the MPAR- and TMPAR-sized array is 5 m and 2.5 m, respectively, z_{mn} is the vertical distance of mth circular array from the center of the cylindrical array, D is the height of the cylindrical array, $c = 3$, $b = 0.16$, and

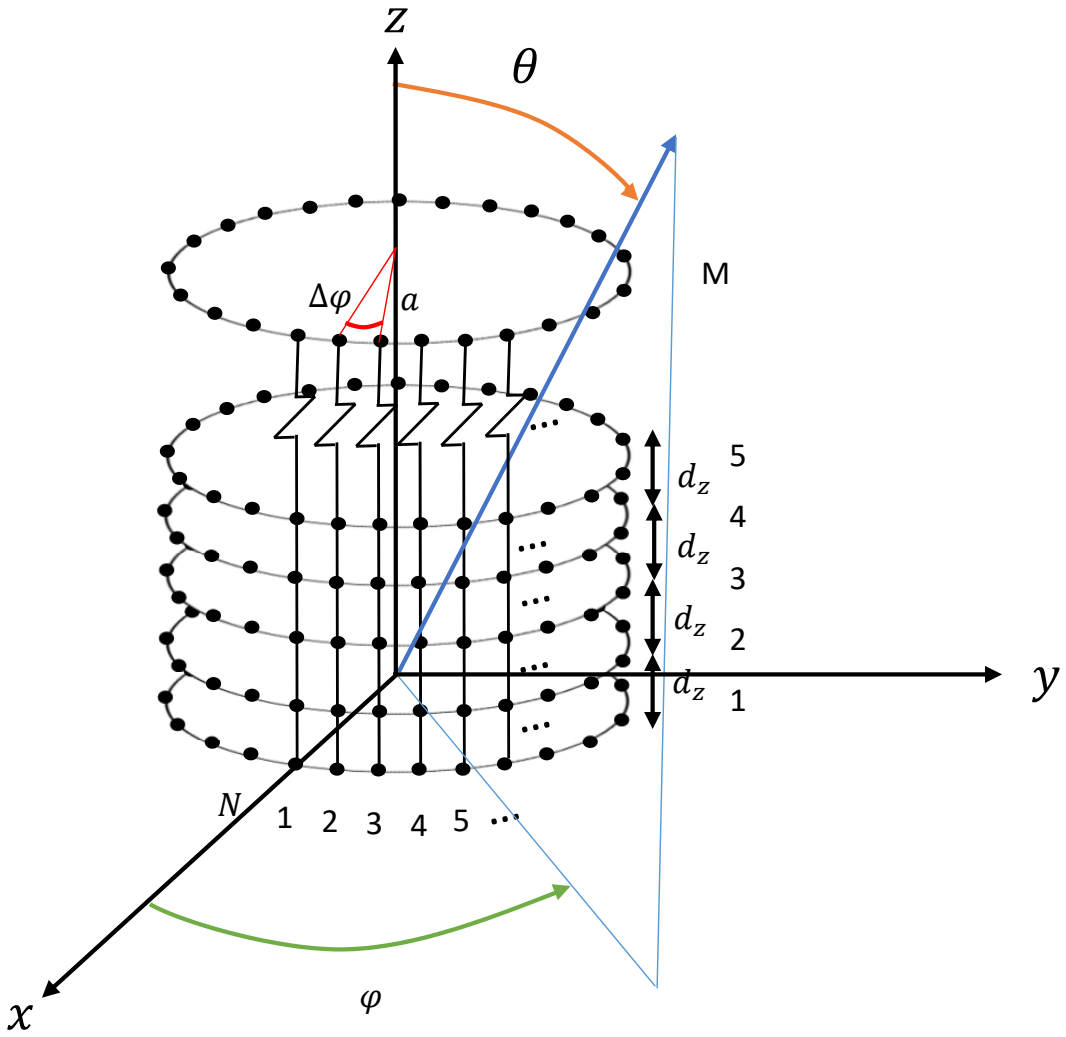

Fig. 5.2: Geometry of cylindrical array antenna.

the MPAR (TMPAR) beam is pointed in the (θ_0, φ_0) direction.

A multifaceted array is made of the combination of planar arrays and cylindrical array. The geometry of a multifaceted array is shown in Fig. 5.3. The array consists of N_f facets of $M \times N_c$-element planar array which N_c is number of columns on each facet and M is number of elements along z-axis.

As is shown in Fig. 5.3 the spacing between elements in z-direction is d_z and let the spacing between array elements in each face in the other direction be d_y. Then

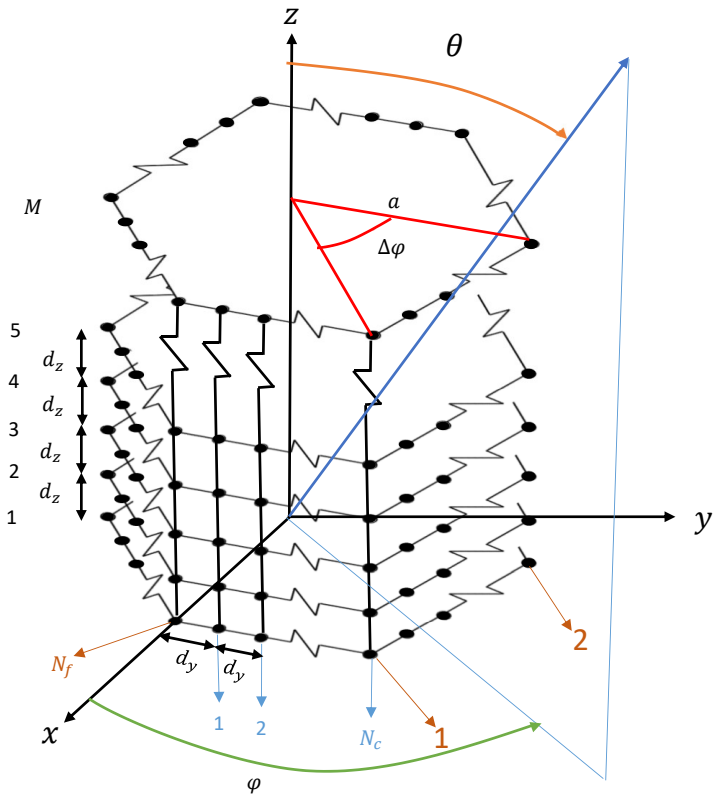

Fig. 5.3: Geometry of multifaceted array antenna.

radiation pattern of a multifaceted array can be calculated based on the coherent addition of the radiation pattern of N_f planar arrays. However, the most accurate method for calculating the radiation pattern of the multifaceted antenna arrays, or any antenna array with an arbitrary geometry, can be calculated based on the following equation:

$$E(\theta,\varphi) = \sum_{p}^{Nl} a_p E(\theta, \varphi - \varphi_p) \times e^{jk[(x_p sin(\theta)cos(\varphi)+y_p sin(\theta)sin(\varphi)+z_p cos(\theta))-(x_p sin(\theta_0)cos(\varphi_0)+y_p sin(\theta_0)sin(\varphi_0)+z_p cos(\theta_0))]} \tag{5.5}$$

In which, $[x_p, y_p, z_p]$ shows the position of each element, $\varphi_p = arctan(y_p/x_p)$,

Nl is number of elements, a_p is the excitation coefficient of p_{th} element, if the axis of the array antenna is in the center of the coordinate system.

5.3 Frequency Scanning Aperture Coupled Microstrip Patch Antenna Array with Matched Dual-Polarization Radiation Patterns

The CPPAR demonstrator which is a 2-meter diameter cylindrical array antenna, populated by 96 columns of frequency scanning array antennas is shown in Fig. 5.4. Although the antenna in the previous design in [25] shows high port-to-port isolation and low cross-polarization, it suffers from a mismatch between both peaks and the overall shapes of the copolarized patterns. This contrasts with the weather observation requirement of having a correlation coefficient higher than 0.99, which requires a patterns mismatch of less than 0.5° **golbon2019**, [67]–[70].

In this section, a precise phase correction method to achieve a pair of matched horizontal and vertical patterns is proposed, implemented, and tested. A step-by-step phase matching between outputs of a row of feed lines cells is carried out. It is followed by phase adjustment between the major outputs of two feed lines. In doing so, a pair of similar horizontal and vertical copolarization patterns with their peaks mismatch less than ±0.2° within the whole frequency bandwidth is achieved. The simulation results are verified by radiation patterns measurements where a good agreement within the whole frequency bandwidth is observed.

5.3.1 Antenna Design

To demonstrate the idea of CPPAR for weather measurement, a 19-element series-fed array of dual-polarized aperture coupled patches was designed and tested [25].

Fig. 5.4: OU/NSSL CPPAR demonstrator.

In the current version, the array is designed to operate in the frequency range from 2.75 to 2.95 GHz. Taconic TLX-8 with a dielectric constant of 2.55 is used in all layers. As shown in Fig. 5.5 (a), the first ground plane is etched on the reverse side of the first substrate with a height of 0.787 mm. The feed lines are placed on the front side of the first substrate. H-shaped slots and second ground plane are laid on the front side of the second substrate with a height of 0.787 mm. The two ground planes are connected to each other with three walls of metalized holes along the feed lines. The third layer is a 3.175 mm thick substrate and contains the square radiating patches, and 5 mm thick substrate with slightly bigger square patches are laid on the third layer to increase the bandwidth of array antenna.

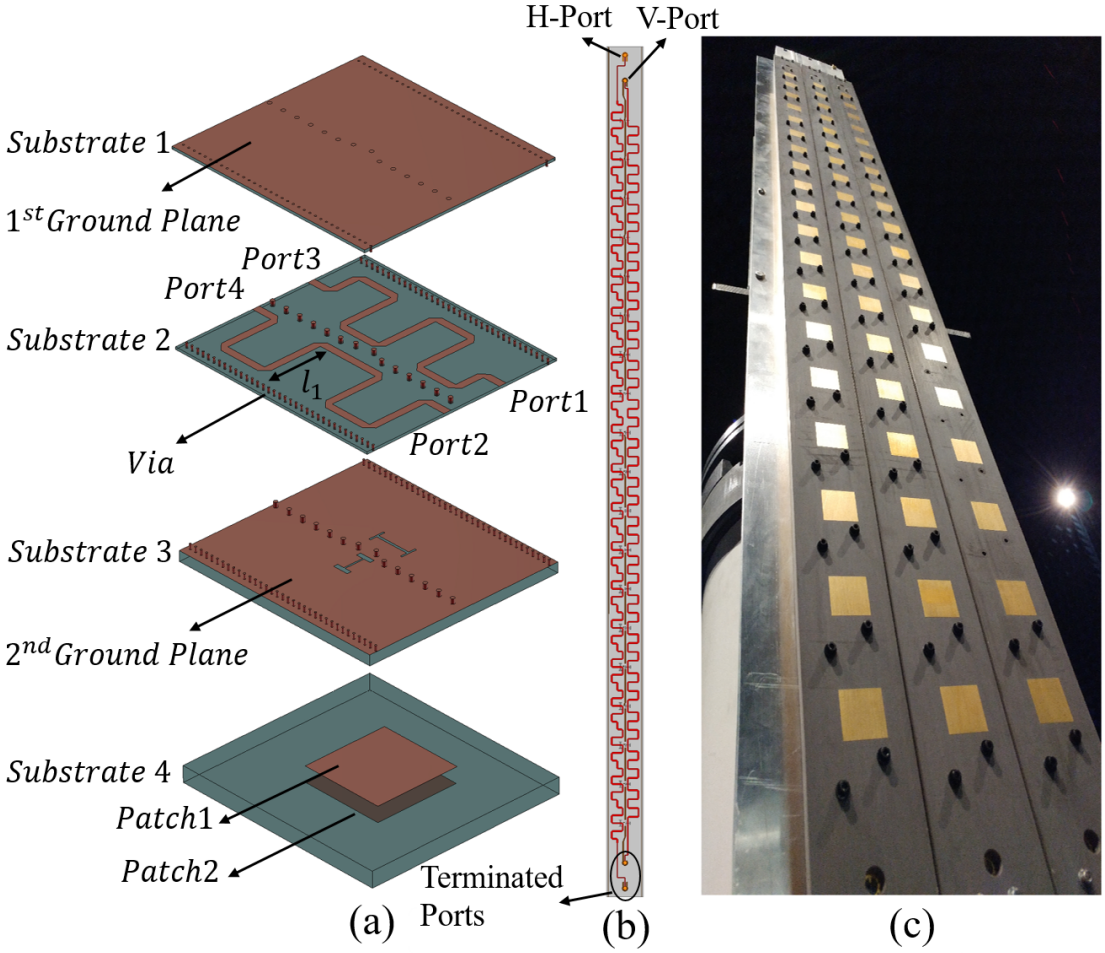

Fig. 5.5: Geometry of 19-element array antenna; (a) single element layers, (b) 19-element array, (c) 3 columns of fabricated 19-element array.

The geometry of the designed 19-element array is shown in Fig. 5.5 (b). The width and length of each column are 64.52 mm and 1.524 m, respectively. The spacing between elements is 70 mm and the length of feed lines are optimized to have a 0° phase shift between patches at 2.73 GHz. Since wavelengths are smaller at higher frequencies, there will be a phase shift between array elements which results in beam steering at higher frequencies.

For weather measurements, it is crucial that the antenna has matched horizontal and vertical polarization radiation patterns. However, the measured

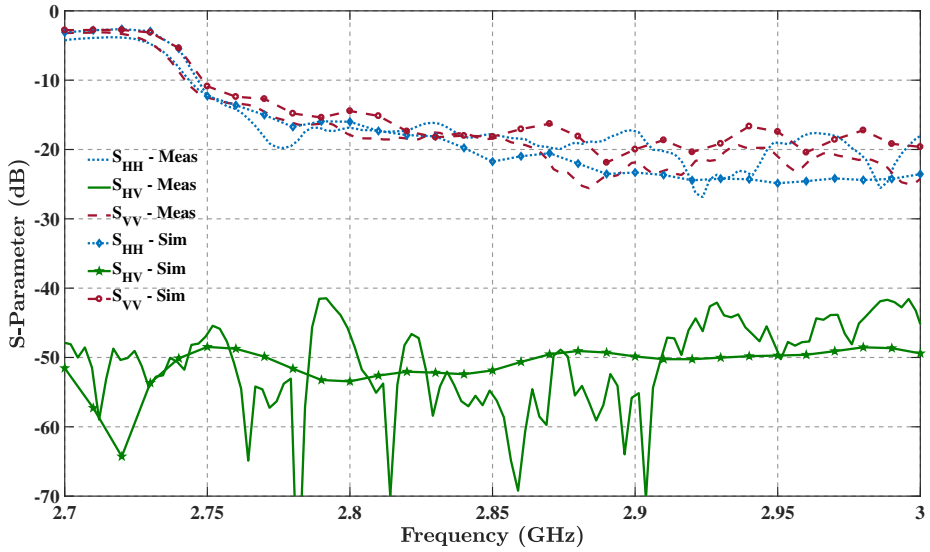

Fig. 5.6: Simulated and measured S-Parameter of designed array antenna.

radiation patterns of the previous design showed that there is a 1.3° beam pointing angle mismatch between measured horizontal and vertical radiation pattern at 2.8 GHz. The primary reason for this mismatch is a 25 dB Taylor amplitude distribution which has been applied to improve the side lobe level. In the series feed design, because the amplitude of excitation of elements cannot be controlled discretely at excitation ports, the slots size and shape are changed to adjust the excitation amplitude of each patch. In the previous design, the feed lines had a periodic form and they were repeated for each element with no change, which caused variant phase shifts between elements through horizontal and vertical feed lines and subsequently resulted in the beam pointing angle mismatch. To avoid this deficiency, the feed line length should be optimized for each element separately. For feed line length adjustments, as shown in Fig. 5.5 (a), each element is separately excited from port 1 and ports 3. The feed line between port 1 and 3 has not been changed and only the length l_1 is adjusted so the phase of S_{42} becomes equal to the phase of S_{31} at 2.8 GHz. The feed line

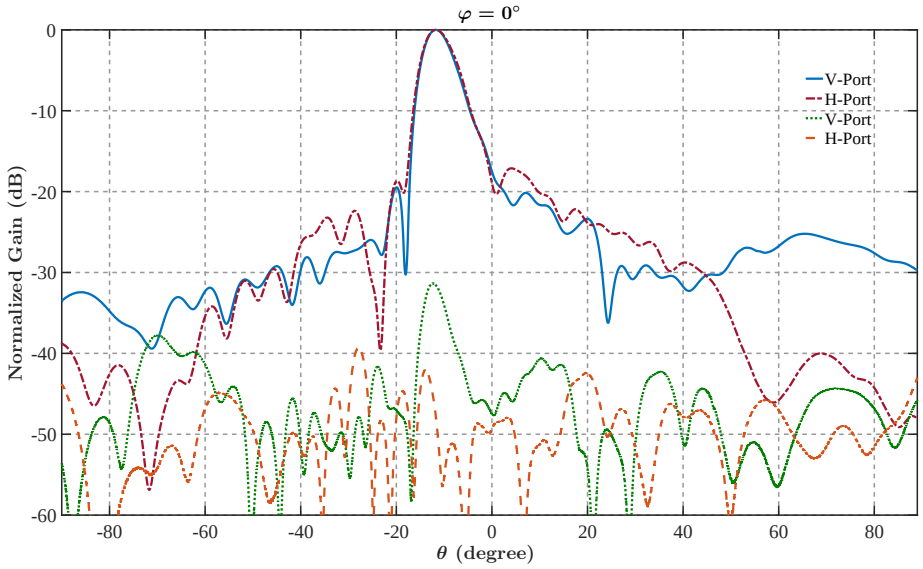

Fig. 5.7: Measured H-Pol and V-Pol co- and cross-polarization radiation pattern of an isolated column.

length adjustment process is repeated for all 19 elements.

The new optimized feed line for the vertical port is used in the new design. The geometry of 3 columns of the fabricated new version is shown in 5.5 (c).

The simulated and measured S-Parameter results of the array antenna are shown in Fig. 5.6. The simulated and measured return loss for both polarization are below -11 dB from 2.75 to 2.8 GHz and below -15 dB from 2.8 to 3 GHz. The simulated and measured isolation between horizontal and vertical ports are below -40 dB in the entire frequency band.

The horizontal and vertical copolarization radiation patterns of the isolated column are measured in the far field anechoic chamber of ARRC.

To examine the mutual coupling effects of adjacent elements, the radiation pattern of the 3-column array when the middle column is excited and two side columns are terminated is also measured.

The measured radiation patterns of isolated (or single) column and embedded

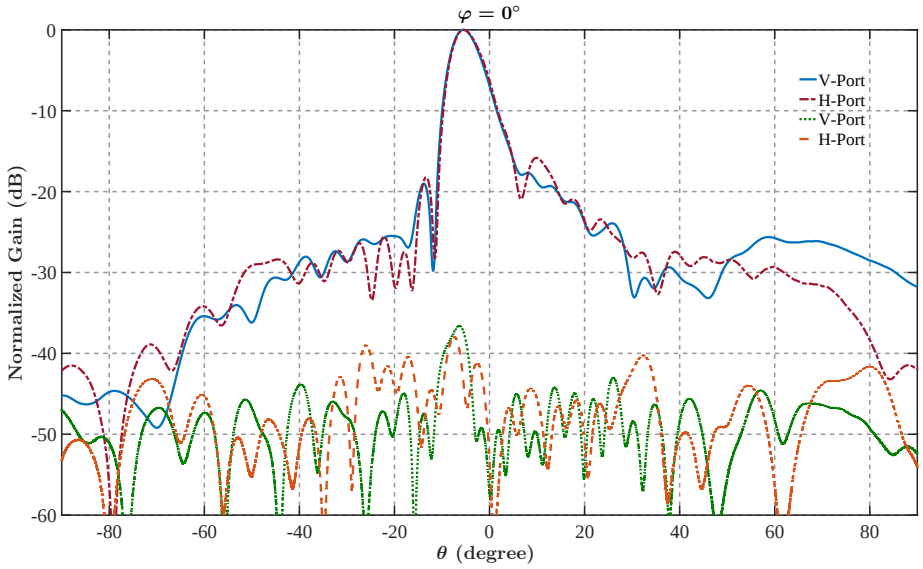

Fig. 5.8: Measured H-Pol and V-Pol co- and cross-polarization radiation pattern of middle column in the 3-column measurement.

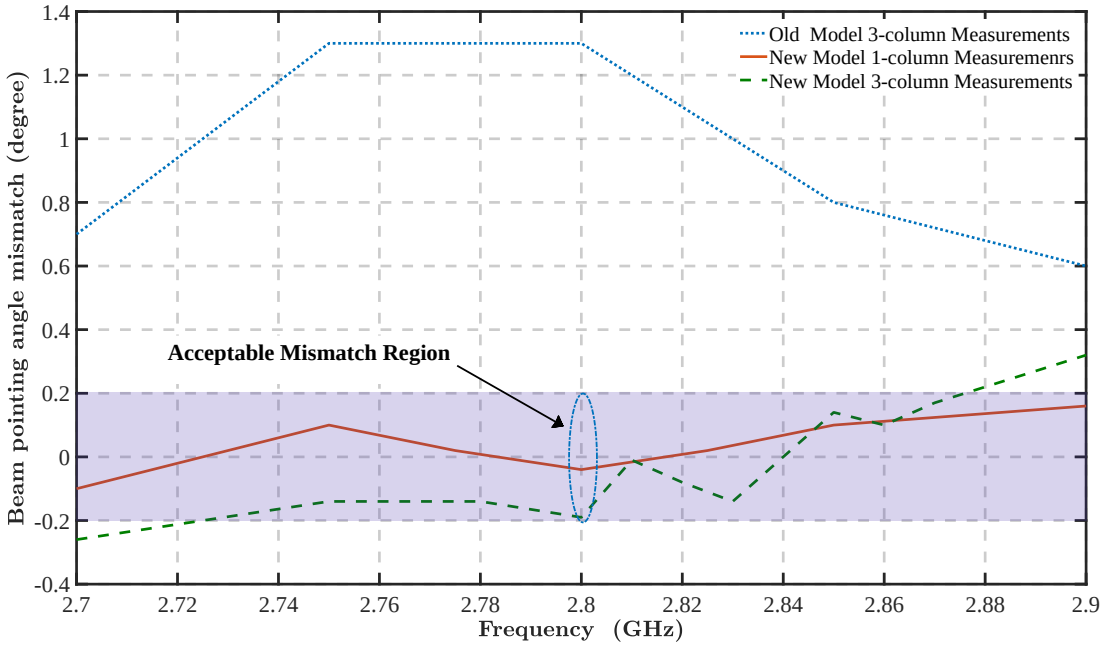

Fig. 5.9: Beam pointing angle mismatch versus frequency.

column (or 3-column) at 2.8 GHz, are shown in Fig. 5.7 and Fig. 5.8, respectively. For the isolated column, the beam mismatch at 2.8 GHz is 0.04° and for 3-column

measurement, the beam mismatch at 2.8 GHz and 2.81 GHz are 0.19° and 0.01°, respectively. The beam pointing angle mismatch for the old version and the current version from 2.7 to 2.9 GHz are compared in Fig. 5.9. It is evident that in the new version the mismatch is within the acceptable region from 2.75 to 2.87 GHz [64], [71].

Chapter 6

Conclusion

6.1 Conclusion and Future Work

6.1.1 Summary

The goal of this dissertation was to design, fabricate and develop state-of-the-art, high-performance dual-polarized antenna arrays which possess low cross-polarization and high input isolation for MPAR application. Different feeding techniques have been discussed and implemented to design several high-performance antenna arrays. First, a brief overview of the evolution of microstrip patch antennas and some of the topologies for realizing dual-polarized microstrip patch antennas are presented in Chapter 2.

In chapter 2, different high-performance microstrip patch antennas for MPAR application have been proposed. In the first design, two none-overlapping, T-shaped transmission lines have been implemented to excited two H-shaped slots. In the second design, a hybrid patch antenna has been designed to improve the geometrical and radiation symmetry of the antenna. The vertical polarization is excited by a pair of 180° out-of-phase currents to attain a low cross-polarization level along beam axis, and horizontal polarization is excite through H-shaped slot in the middle of the ground plane. In the second hybrid feed design to

decrease the antenna fabrication complexity and improve the mechanical stability, the balanced prob-feeding technique in the second design has been replaced with balanced aperture coupling method.

In chapter 3, the issues and changes associated with implementing an image feed method in the large antenna array are discussed. It is shown that decomposing the antenna radiation pattern to its even and odd components, for calculating the configured arrays radiation pattern has some fundamental shortcoming. In this chapter, a proper procedure has been proposed for predicting array sidelobe level and reducing its minimum possible level.

In chapter 4, the proposed high-performance single elements for MPAR application in chapter 2 are characterized in the array configuration while the elements are arranged according to the image configuration. Based on the measured results, an input isolation of better than 51 dB and cross-polarization level of better than -45 dB in the main beam area while scanning up to 45 degrees are achieved.

Finally, in chapter 5, conformal array antennas radiation characteristics have been discussed. In this chapter, a 19-element dual-polarized frequency scanning aperture coupled microstrip patch antenna is designed, fabricated, and the simulation and measurement results are presented. The horizontal and vertical beam pointing mismatch issue has been resolved by length optimization of the feed lines. The horizontal and vertical polarization radiation pattern of a single column and three column measurement are presented. Measured results show that the beam pointing angle mismatch for single column measurement is below 0.2° in the entire frequency band and for three-column measurement is below 0.2° from 2.75 to 2.87 GHz.

6.1.2 Contributions

1. Improvement and fabrication of a 19-element dual polarized frequency scanning aperture coupled microstrip patch antenna with less than 0.2° beam pointing angle mismatch from 2.75 to 2.87 GHz and input isolation of better than 40 dB for CPPAR demonstrator.

2. Design and fabrication of a planar array of dual polarized none-overlapping aperture coupled patch antenna with a very high input isolation and low cross-polarization radiation pattern.

3. Design and fabrication of a high-performance hybrid dual-polarized antenna array excited by aperture coupling and differential probe-fed methods.

4. Design and fabrication a low-fabrication complexity, dual-polarized hybrid-fed microstrip patch antenna excited by balanced aperture coupling and single symmetric aperture coupling methods.

5. Characterization of the issues and changes of using image configuration for cross-polarization suppression in the large phased array antennas and proposing an accurate procedure for predicting and mitigating the sidelobes.

6.1.3 Future Work

The works presented in this dissertation can be expanded in the area of the array final geometry. Multifaceted CPPAR can be an alternative approach for future multifunction phased array radar. In the multifaceted radar approach, the final array geometry will be a polygon. Compared to the four-faced planar array, there are more than four facets that cover 360°. A multifaceted phased array

radar has the advantage of low-cost fabrication, similar to planar arrays, and its electromagnetic characteristics are similar to cylindrical polarimetric phased array radar. The future research plans should determine the minimum number of facets, and a maximum number of columns per facet, so the multifaceted radar can satisfy the MPAR requirements. Multifaceted phased array radar approach antenna is a trade-off between performance and fabrication cost. The output of this research will be the optimized geometry for the performance and fabrication cost of future MPAR.

References

[1] D. D. Grieg and H. F. Engelmann, "Microstrip-a new transmission technique for the klilomegacycle range", *Proceedings of the IRE*, vol. 40, no. 12, pp. 1644–1650, 1952, ISSN: 0096-8390. DOI: 10.1109/JRPROC.1952.274144.

[2] C. A. Balanis, *Antenna theory: analysis and design*. John Wiley & Sons, 2016.

[3] H. Saeidi-Manesh and G. Zhang, "Dual-linear polarization phased array antenna cross-polarization suppression using a novel image configuration", in *Antennas and Propagation (APSURSI), 2016 IEEE International Symposium on*, IEEE, 2016, pp. 525–526.

[4] H. Wong, K.-L. Lau, and K.-M. Luk, "Design of dual-polarized l-probe patch antenna arrays with high isolation", *IEEE Transactions on Antennas and Propagation*, vol. 52, no. 1, pp. 45–52, 2004.

[5] H.-W. Lai and K.-M. Luk, "Dual polarized patch antenna fed by meandering probes", *IEEE Transactions on Antennas and propagation*, vol. 55, no. 9, pp. 2625–2627, 2007.

[6] P. K. Mishra, D. R. Jahagirdar, and G. Kumar, "A review of broadband dual linearly polarized microstrip antenna designs with high isolation [education column]", *IEEE Antennas and Propagation Magazine*, vol. 56, no. 6, pp. 238–251, 2014.

[7] D. M. Pozar, "Microstrip antenna aperture-coupled to a microstripline", *Electronics Letters*, vol. 21, no. 2, pp. 49–50, 1985, ISSN: 0013-5194. DOI: 10.1049/el:19850034.

[8] R. Caso, A. Serra, A. Buffi, M. Rodriguez-Pino, P. Nepa, and G. Manara, "Dual-polarised slot-coupled patch antenna excited by a square ring slot", *IET Microwaves, Antennas & Propagation*, vol. 5, no. 5, pp. 605–610, 2011.

[9] T. Chiba, Y. Suzuki, and N. Miyano, "Suppression of higher modes and cross polarized component for microstrip antennas", in *1982 Antennas and Propagation Society International Symposium*, vol. 20, 1982, pp. 285–288. DOI: 10.1109/APS.1982.1148910.

[10] T.-W. Chiou and K.-L. Wong, "Broad-band dual-polarized single microstrip patch antenna with high isolation and low cross polarization", *IEEE transactions on Antennas and Propagation*, vol. 50, no. 3, pp. 399–401, 2002.

[11] H. Saeidi-Manesh and G. Zhang, "Hybrid-fed microstrip patch antenna for MPAR application", in *2017 IEEE International Symposium on Antennas and Propagation USNC/URSI National Radio Science Meeting*, 2017, pp. 1895–1896. DOI: 10.1109/APUSNCURSINRSM.2017.8072990.

[12] K.-L. Wong and T.-W. Chiou, "Broadband dual-polarized patch antennas fed by capacitively coupled feed and slot-coupled feed", *IEEE Transactions on Antennas and Propagation*, vol. 50, no. 3, pp. 346–351, 2002.

[13] G. Zhang, *Weather Radar Polarimetry*. CRC Press, 2016.

[14] B. M. Golbon-Haghighi M. H. and M. Ardebilipour, "Linear pre-coding in mimo-cdma relay networks", *Wireless Personal Communications*, vol. 79, no. 2, pp. 1321–1341, 2014. DOI: 10.1007/s11277-014-1932-7.

[15] B. Golbon-Haghighi M. H. and M. Ardebilipour, "Beamforming in wireless networks", *InTech Open*, pp. 163–192, 2016.

[16] M. M. B. A. M. Golbon-Haghighi M.-H.; Shirazi, "Dual polarization ground clutter filtering", in *21st Iranian Conference on Electrical Engineering (ICEE)*, 2013.

[17] B. M. Golbon-Haghighi M. H. and M. Ardebilipour, "Multiple antenna relay beamforming for wireless peer to peer communications", *Journal of Information Systems and Telecommunication (JIST)*, vol. 1, no. 4, pp. 209–215, 2013.

[18] R. Irazoqui and C. Fulton, "Spatial interference mitigation nulling the embedded element pattern", in *2018 IEEE/MTT-S International Microwave Symposium - IMS*, 2018, pp. 620–623. DOI: 10.1109/MWSYM.2018.8439271.

[19] J. E. Stailey and K. D. Hondl, "Multifunction phased array radar for aircraft and weather surveillance", *Proceedings of the IEEE*, vol. 104, no. 3, pp. 649–659, 2016.

[20] M. Mirmozafari, H. Saeidi-Manesh, and G. Zhang, "Highly isolated crossed dipole antenna with matched copolar beams", *Electronics Letters*, vol. 54, no. 8, pp. 470–472, 2018, ISSN: 0013-5194. DOI: 10.1049/el.2018.0519.

[21] M.-H. Golbon-Haghighi, G. Zhang, Y. Li, and R. J. Doviak, "Detection of ground clutter from weather radar using a dual-polarization and dual-scan method", *Atmosphere*, vol. 7, no. 6, p. 83, 2016.

[22] H. Saeidi-Manesh, S. Saeedi, M. Mirmozafari, G. Zhang, and H. H. Sigmarsson, "Design and fabrication of orthogonal-mode transducer using 3-d printing technology", *IEEE Antennas and Wireless Propagation Letters*, vol. 17, no. 11, pp. 2013–2016, 2018, ISSN: 1536-1225. DOI: 10.1109/LAWP.2018.2847654.

[23] R. L. Jordan, B. L. Huneycutt, and M. Werner, "The sir-c/x-sar synthetic aperture radar system", *IEEE Transactions on Geoscience and Remote Sensing*, vol. 33, no. 4, pp. 829–839, 1995.

[24] G. Zhang, R. J. Doviak, D. S. Zrnić, R. Palmer, L. Lei, and Y. Al-Rashid, "Polarimetric phased-array radar for weather measurement: A planar or cylindrical configuration?", *Journal of Atmospheric and Oceanic Technology*, vol. 28, no. 1, pp. 63–73, 2011.

[25] S. Karimkashi and G. Zhang, "A dual-polarized series-fed microstrip antenna array with very high polarization purity for weather measurements", *IEEE Transactions on Antennas and Propagation*, vol. 61, no. 10, pp. 5315–5319, 2013, ISSN: 0018-926X. DOI: 10.1109/TAP.2013.2273813.

[26] R. J. Doviak, L. Lei, G. Zhang, J. Meier, and C. Curtis, "Comparing theory and measurements of cross-polar fields of a phased-array weather radar", *IEEE Geoscience and Remote Sensing Letters*, vol. 8, no. 5, pp. 1002–1006, 2011.

[27] R. Doviak, "A memorandum on comparisons of weather and aircraft surveillance radar requirements to determine key features for a 10-cm MPAR and SENSR NOAA", *NSSL, Norman, Oklahoma, USA (NSSL Online Report)*, 2017.

[28] L. Lei, G. Zhang, and R. J. Doviak, "Bias correction for polarimetric phased-array radar with idealized aperture and patch antenna elements", *IEEE Transactions on Geoscience and Remote Sensing*, vol. 51, no. 1, pp. 473–486, 2013.

[29] F. A. Administration, "Multifunction phased array radar (MPAR) notional functional requirements document (version 2.2)", *(pp. 1–16). Washington, DC: NextGen Surveillance and Weather Radar Capability*, 2013.

[30] L. Lei, G. Zhang, R. J. Doviak, and S. Karimkashi, "Comparison of theoretical biases in estimating polarimetric properties of precipitation with weather radar using parabolic reflector, or planar and cylindrical arrays", *IEEE Transactions on Geoscience and Remote Sensing*, vol. 53, no. 8, pp. 4313–4327, 2015.

[31] D. Zrnic, R. Doviak, G. Zhang, and A. Ryzhkov, "Bias in differential reflectivity due to cross coupling through the radiation patterns of polarimetric weather radars", *Journal of Atmospheric and Oceanic Technology*, vol. 27, no. 10, pp. 1624–1637, 2010.

[32] I. R. Ivić and R. J. Doviak, "Evaluation of phase coding to mitigate differential reflectivity bias in polarimetric par", *IEEE Transactions on Geoscience and Remote Sensing*, vol. 54, no. 1, pp. 431–451, 2016.

[33] D. Zrnić, V. Melnikov, and R. Doviak, "A draft report on issues and challenges for polarimetric measurement of weather with an agile-beam phased array radar", *NOAA/NSSL, Norman, Oklahoma, USA (NSSL Online Report)*, 2012.

[34] A Adrian and D. Schaubert, "Dual aperture-coupled microstrip antenna for dual or circular polarisation", *Electronics Letters*, vol. 23, no. 23, pp. 1226–1228, 1987.

[35] T. Chaloun, V. Ziegler, and W. Menzel, "Design of a dual-polarized stacked patch antenna for wide-angle scanning reflectarrays", *IEEE Transactions on Antennas and Propagation*, vol. 64, no. 8, pp. 3380–3390, 2016.

[36] D Pozar and D Schaubert, "Scan blindness in infinite phased arrays of printed dipoles", *IEEE Transactions on Antennas and Propagation*, vol. 32, no. 6, pp. 602–610, 1984.

[37] H. Saeidi-Manesh and G. Zhang, "Dual-polarized hybrid feed microstrip patch antenna for multifunction application", *Electronics letters*, pp. 1–2, 2018.

[38] H. Saeidi-Manesh and G. Zhang, "Dual-polarized aperture-coupled hybrid-fed microstrip patch antenna for MPAR application", in *2018 IEEE International Symposium on Antennas and Propagation USNC/URSI National Radio Science Meeting*, 2018, pp. 2141–2142. DOI: 10.1109/APUSNCURSINRSM.2018.8608351.

[39] D. M. Pozar and B. Kaufman, "Increasing the bandwidth of a microstrip antenna by proximity coupling", *Electronics Letters*, vol. 23, no. 8, pp. 368–369, 1987, ISSN: 0013-5194. DOI: 10.1049/el:19870270.

[40] D. M. Pozar, *Microwave engineering*. John Wiley & Sons, 2009.

[41] V. Palanisamy and R. Garg, "Rectangular ring and h-shaped microstrip antennas-alternatives to rectangular patch antenna", *Electronics Letters*, vol. 21, no. 19, pp. 874–876, 1985, ISSN: 0013-5194. DOI: 10.1049/el:19850617.

[42] C. A. Balanis, *Modern antenna handbook*. John Wiley & Sons, 2011.

[43] H. Saeidi-Manesh, S. Karimkashi, G. Zhang, and R. J. Doviak, "High-isolation low cross-polarization phased-array antenna for MPAR application", *Radio Science*, vol. 52, no. 12, pp. 1544–1557, 2017, 2017RS006304, ISSN: 1944-799X. DOI: 10.1002/2017RS006304. [Online]. Available: http://dx.doi.org/10.1002/2017RS006304.

[44] R. Garg, *Microstrip antenna design handbook*. Artech house, 2001.

[45] M.-H. Golbon-Haghighi, H. Saeidi-Manesh, G. Zhang, and Y. Zhang, "Pattern synthesis for the cylindrical polarimetric phased array radar (CPPAR)", *Progress In Electromagnetics Research*, vol. 66, pp. 87–98, 2018.

[46] D. M. Pozar, "Scanning characteristics of infinite arrays of printed antenna subarrays", *IEEE transactions on antennas and propagation*, vol. 40, no. 6, pp. 666–674, 1992.

[47] M. E. Weber, J. Y. Cho, J. S. Herd, J. M. Flavin, W. E. Benner, and G. S. Torok, "The next-generation multimission us surveillance radar

network", *Bulletin of the American Meteorological Society*, vol. 88, no. 11, pp. 1739–1751, 2007.

[48] Y. Rahmat-Samii, K. S. Kona, M. Manteghi, S. Yueh, W. J. Wilson, J. S. Dinardo, and D. Hunter, "A novel lightweight dual-frequency dual-polarized sixteen-element stacked patch microstrip array antenna for soil-moisture and sea-surface-salinity missions", *IEEE Antennas and Propagation Magazine*, vol. 48, no. 6, pp. 33–46, 2006.

[49] D. Vollbracht, "Optimum phase excitations and probe- feed positions inside antenna arrays for the reduction of cross polarization radiation in demanding phased array weather radar applications", in *2016 10th European Conference on Antennas and Propagation (EuCAP)*, 2016, pp. 1–5. DOI: 10.1109/EuCAP.2016.7481625.

[50] M. Mirmozafari, S. Saeedi, H. Saeidi-Manesh, G. Zhang, and H. H. Sigmarsson, "Direct 3-d printing of nonplanar linear-dipole-phased array antennas", *IEEE Antennas and Wireless Propagation Letters*, vol. 17, no. 11, pp. 2137–2140, 2018, ISSN: 1536-1225. DOI: 10.1109/LAWP.2018.2860463.

[51] H. Saeidi-Manesh and G. Zhang, "Low cross-polarization, high-isolation microstrip patch antenna array for multi-mission applications", *IEEE Access*, vol. 7, pp. 5026–5033, 2019, ISSN: 2169-3536. DOI: 10.1109/ACCESS.2018.2889599.

[52] H Saeidi-Manesh and G Zhang, "Cross-polarisation suppression in cylindrical array antenna", *Electronics Letters*, vol. 53, no. 9, pp. 577–578, 2017.

[53] K Woelder and J. Granholm, "Cross-polarization and sidelobe suppression in dual linear polarization antenna arrays", *IEEE transactions on antennas and propagation*, vol. 45, no. 12, pp. 1727–1740, 1997.

[54] H. Saeidi-Manesh and G. Zhang, "Characterization and optimization of cylindrical polarimetric array antenna patterns for multi-mission applications", *Progress In Electromagnetics Research*, vol. 158, pp. 49–61, 2017.

[55] Z. Sun, S.-S. Zhong, X.-R. Tang, and J.-j. Liu, "C-band dual-polarized stacked-patch antenna with low cross-polarization and high isolation", in

Antennas and Propagation, 2009. EuCAP 2009. 3rd European Conference on, IEEE, 2009, pp. 2994–2997.

[56] H. Saeidi-Manesh and G. Zhang, "High-isolation, low cross-polarization, dual- polarization, hybrid feed microstrip patch array antenna for MPAR application", *IEEE Transactions on Antennas and Propagation*, vol. 66, no. 5, pp. 2326–2332, 2018, ISSN: 0018-926X. DOI: 10.1109/TAP.2018.2811780.

[57] D. Pozar, "The active element pattern", *IEEE Transactions on Antennas and Propagation*, vol. 42, no. 8, pp. 1176–1178, 1994, ISSN: 0018-926X. DOI: 10.1109/8.310010.

[58] D. K. Papantonis and J. L. Volakis, "Dual-polarized tightly coupled array with substrate loading", *IEEE Antennas and Wireless Propagation Letters*, vol. 15, pp. 325–328, 2016, ISSN: 1536-1225. DOI: 10.1109/LAWP.2015.2443725.

[59] A. Mancini, R. M. Lebrón, and J. L. Salazar, "The impact of a wet s -band radome on dual-polarized phased-array radar system performance", *IEEE Transactions on Antennas and Propagation*, vol. 67, no. 1, pp. 207–220, 2019, ISSN: 0018-926X. DOI: 10.1109/TAP.2018.2876733.

[60] A. Mancini, J. L. Salazar, R. M. Lebrón, and B. L. Cheong, "A novel instrument for real-time measurement of attenuation of weather radar radome including its outer surface. part ii: Applications", *Journal of Atmospheric and Oceanic Technology*, vol. 35, no. 5, pp. 975–991, 2018. DOI: 10.1175/JTECH-D-17-0084.1. eprint: https://doi.org/10.1175/JTECH-D-17-0084.1. [Online]. Available: https://doi.org/10.1175/JTECH-D-17-0084.1.

[61] A. Mancini, J. Salazar, R. Lebron, and B. Cheong, "A novel instrument for real-time measurement of weather radar radome attenuation", *Bulletin of the American Meteorological Society*, vol. 99, no. 4, pp. 672–674, 2018.

[62] A. Mancini, J. L. Salazar, R. M. Lebrón, and B. L. Cheong, "A novel technique to characterize the effect of rain over a radome for radar applications", in *2017 IEEE Radar Conference (RadarConf)*, 2017, pp. 0470–0475. DOI: 10.1109/RADAR.2017.7944249.

[63] A. Mancini, J. L. Salazar, R. M. Lebrón, and B. L. Cheong, "A novel instrument for real-time measurement of attenuation of weather radar

radome including its outer surface. part i: The concept", *Journal of Atmospheric and Oceanic Technology*, vol. 35, no. 5, pp. 953–973, 2018. DOI: 10.1175/JTECH-D-17-0083.1. eprint: https://doi.org/10.1175/JTECH-D-17-0083.1. [Online]. Available: https://doi.org/10.1175/JTECH-D-17-0083.1.

[64] H Saeidi-Manesh, M Mirmozafari, and G Zhang, "Low cross-polarisation high-isolation frequency scanning aperture coupled microstrip patch antenna array with matched dual-polarisation radiation patterns", *Electronics Letters*, vol. 53, no. 14, pp. 901–902, 2017.

[65] L. Josefsson and P. Persson, *Conformal array antenna theory and design*. John wiley & sons, 2006, vol. 29.

[66] R. J. Mailloux, *Phased array antenna handbook*. Artech house, 2017.

[67] M.-H. Golbon-Haghighi and G. Zhang, "Detection of ground clutter for dual-polarization weather radar using a novel 3d discriminant function", *Journal of Atmospheric and Oceanic Technology*, 2019.

[68] M. Golbon-Haghighi, G. Zhang, and R. J. Doviak, "Ground clutter detection for weather radar using phase fluctuation index", *IEEE Transactions on Geoscience and Remote Sensing*, vol. 57, no. 5, pp. 2889–2895, 2019, ISSN: 0196-2892. DOI: 10.1109/TGRS.2018.2878378.

[69] M.-H. Golbon-Haghighi and G. Zhang, "Dual polarization ground clutter filtering", in *35th Environmental Information Processing Technologies Conference, AMS Annual Meeting*, Phoenix, AZ, 2019.

[70] M.-H. Golbon-Haghighi, G. Zhang, Y. Li, and R. J. Doviak, "Detection of ground clutter from weather radar using a dual-polarization and dual-scan method", *Atmosphere*, vol. 7, no. 6, p. 83, 2016.

[71] H. Saeidi-Manesh and G. Zhang, "Optimized dual-linear polarization frequency scanning microstrip array antenna for cylindrical polarimetric phased array radar (cppar)", pp. 2021–2022, 2017, ISSN: 1947-1491. DOI: 10.1109/APUSNCURSINRSM.2017.8073053.

Appendix A

Publications

Journal Papers:

[1] H. Saeidi-Manesh and G. Zhang, "Low Cross-Polarization, High-Isolation Microstrip Patch Antenna Array for Multi-Mission Applications," in *IEEE Access*, vol. 7, pp. 5026-5033, 2019.

[2] M. Mirmozafari, S. Saeedi, H. Saeidi-Manesh, G. Zhang and H. H. Sigmarsson, "Direct 3-D Printing of Nonplanar Linear-Dipole-Phased Array Antennas," in *IEEE Antennas and Wireless Propagation Letters*, vol. 17, no. 11, pp. 2137-2140, Nov. 2018.

[3] H. Saeidi-Manesh, S. Saeedi, M. Mirmozafari, G. Zhang and H. H. Sigmarsson, "Design and Fabrication of Orthogonal-Mode Transducer Using 3-D Printing Technology," in IEEE Antennas and Wireless Propagation Letters, vol. 17, no. 11, pp. 2013-2016, Nov. 2018.

[4] H. Saeidi-Manesh, and G. Zhang. "Dual-polarised hybrid feed microstrip patch antenna for multifunction application." Electronics Letters (2018).

[5] M.-H. Golbon-Haghighi, H. Saeidi-Manesh, G. Zhang, and Y. Zhang, "Pattern Synthesis for the Cylindrical Polarimetric Phased Array Radar (CPPAR)," Progress In Electromagnetics Research M, Vol. 66, 87-98, 2018.

[6] M. Mirmozafari, H. Saeidi-Manesh and G. Zhang, "Highly isolated crossed

dipole antenna with matched copolar beams," in Electronics Letters, vol. 54, no. 8, pp. 470-472, 19 4 2018.

[7] H. Saeidi-Manesh and G. Zhang, "High-Isolation, Low Cross-Polarization, Dual- Polarization, Hybrid Feed Microstrip Patch Array Antenna for MPAR Application," in IEEE Transactions on Antennas and Propagation, vol. 66, no. 5, pp. 2326-2332, May 2018.

[8] H. Saeidi-Manesh., S. Karimkashi, G. Zhang, & R.J. Doviak, (2017). High-isolation low cross-polarization phased-array antenna for MPAR application. Radio Science, 52, 1544–1557.

[9] H. Saeidi-Manesh, M. Mirmozafari and G. Zhang, "Low cross-polarisation high-isolation frequency scanning aperture coupled microstrip patch antenna array with matched dual-polarisation radiation patterns," in Electronics Letters, vol. 53, no. 14, pp. 901-902, 6 7 2017.

[10] H. Saeidi-Manesh and G. Zhang, "Cross-polarisation suppression in cylindrical array antenna," in Electronics Letters, vol. 53, no. 9, pp. 577-578, 27 4 2017.

[11] H. Saeidi-Manesh and G. Zhang, "Characterization and Optimization of Cylindrical Polarimetric Array Antenna Patterns for Multi-Mission Applications," Progress In Electromagnetics Research, Vol. 158, 49-61, 2017.

Conference Papers:

[1] H. Saeidi-Manesh and G. Zhang, "Dual-Polarized Aperture-Coupled Hybrid-Fed Microstrip Patch Antenna for MPAR Application," 2018 IEEE International Symposium on Antennas and Propagation & USNC/URSI National Radio Science Meeting, Boston, MA, 2018, pp. 2141-2142.

[2] H. Saeidi-Manesh and G. Zhang, "Hybrid-fed microstrip patch antenna for MPAR application," 2017 IEEE International Symposium on Antennas and Propagation & USNC/URSI National Radio Science Meeting, San Diego, CA, 2017, pp. 1895-1896.

[3] H. Saeidi-Manesh and G. Zhang, "Optimized dual-linear polarization frequency scanning microstrip array antenna for cylindrical polarimetric phased array radar (CPPAR)," 2017 IEEE International Symposium on Antennas and Propagation & USNC/URSI National Radio Science Meeting, San Diego, CA, 2017, pp. 2021-2022.

[4] H. Saeidi-Manesh and G. Zhang, "Dual-linear polarization phased array antenna cross-polarization suppression using a novel image configuration," 2016 IEEE International Symposium on Antennas and Propagation (APSURSI), Fajardo, 2016, pp. 525-526.